

THE UNIVERSITY OF CALGARY
SPECTROELECTROCHEMISTRY OF SOME IRON PORPHYRINS

by

David H. Jones

A THESIS
SUBMITTED TO THE FACULTY OF GRADUATE STUDIES
IN PARTIAL FULFILMENT OF THE REQUIREMENTS FOR THE
DEGREE OF DOCTOR OF PHILOSOPHY

DEPARTMENT OF CHEMISTRY

CALGARY, ALBERTA

MAY, 1992

© David H. Jones 1992



National Library
of Canada

Acquisitions and
Bibliographic Services Branch

395 Wellington Street
Ottawa, Ontario
K1A 0N4

Bibliothèque nationale
du Canada

Direction des acquisitions et
des services bibliographiques

395, rue Wellington
Ottawa (Ontario)
K1A 0N4

Your file Votre référence

Our file Notre référence

The author has granted an irrevocable non-exclusive licence allowing the National Library of Canada to reproduce, loan, distribute or sell copies of his/her thesis by any means and in any form or format, making this thesis available to interested persons.

L'auteur a accordé une licence irrévocable et non exclusive permettant à la Bibliothèque nationale du Canada de reproduire, prêter, distribuer ou vendre des copies de sa thèse de quelque manière et sous quelque forme que ce soit pour mettre des exemplaires de cette thèse à la disposition des personnes intéressées.

The author retains ownership of the copyright in his/her thesis. Neither the thesis nor substantial extracts from it may be printed or otherwise reproduced without his/her permission.

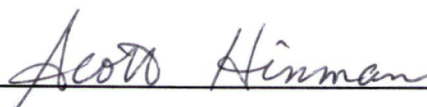
L'auteur conserve la propriété du droit d'auteur qui protège sa thèse. Ni la thèse ni des extraits substantiels de celle-ci ne doivent être imprimés ou autrement reproduits sans son autorisation.

ISBN 0-315-79149-7

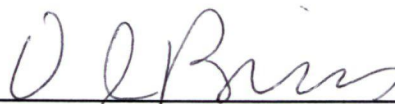
Canada 

THE UNIVERSITY OF CALGARY
FACULTY OF GRADUATE STUDIES

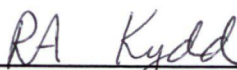
The undersigned certify that they have read, and recommend to the Faculty of Graduate Studies for acceptance, a thesis entitled, "Spectroelectrochemistry of Some Iron Porphyrins" submitted by David H. Jones in partial fulfilment of the requirements for the degree of Doctor of Philosophy



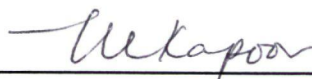
Supervisor, Dr. A. S. Hinman, Department of Chemistry.



Dr. V. I. Birss, Department of Chemistry.



Dr. R. A. Kydd, Department of Chemistry.



Dr. M. Kapoor, Department of Biological Sciences.



External Examiner, Dr. M. J. Stillman, The University of Western Ontario.

Date: 6th May 1992

Abstract

A thin-layer ultraviolet-visible spectroelectrochemistry system has been constructed using a commercially available spinning grating monochromator. The spectroelectrochemical experiment is capable of scanning a wavelength range of 369 to 617 nm in 2.1 ms. The time delay between successive scans is 83 ms. The spectroelectrochemistry of (tetraphenylporphyrinato)copper(II), studied using the system, is presented.

A chronoabsorptometric cell based on an external reflectance geometry has been incorporated into a double potential step chronoabsorptometry experiment. The 1e oxidation of chloro(tetraphenylporphyrinato)iron(III) was investigated using the system and the u.v.-visible spectrum of the 1e oxidized π -cation radical was calculated from chronoabsorptometric data.

The difference spectra in the mid-infrared region associated with oxidation of the porphyrin ring in Mn(III), Fe(III), and Co(III) tetraphenylporphyrin complexes have been obtained by *in situ* FTIR spectroelectrochemistry, and are compared to those similarly observed for the corresponding metal(II)-metal(III) redox couples. Characteristic spectral changes are observed for both reaction types

which thus provide a means to differentiate between ligand- and metal-centred oxidation.

The one-electron oxidation of difluoro(tetraphenylporphyrinato)iron(III) and hydroxy(tetramesitylporphyrinato)iron(III) have been studied using a variety of spectroelectrochemical and voltammetric techniques. The results of these studies provide strong evidence that the initial one-electron oxidation of these species is centred at the porphyrin ring and not the metal as previously suggested.

The relative energies and molecular structures of one-electron oxidized iron(III) porphine derivatives have been studied using approximate density functional methods. These results provide support for a proposed relationship between the spin-state and the oxidation site in iron(III) porphyrins. The $\pi \rightarrow \pi^*$ singlet transitions of chloro(porphyrinato)iron(III) have been calculated and an alternative assignment of the u.v.-visible spectra of iron(III) porphyrins is suggested.

To Mum and Dad

To Jenny

Acknowledgements

The author wishes to acknowledge: Dr. A. Scott Hinman for his help, encouragement, and supervision of this thesis research; Dr. Tom Ziegler for carrying out the density functional calculations and his contributions to the theoretical aspects of this research; Drs. R. A. Kydd and H. Wieser for allowing me the use of their Nicolet 8000 infrared spectrometer; Jenny M. Lewis and Dr. Thomas Eggimann for fruitful discussions regarding this work; Mr. C. Tang for the preparation of tetramesitylporphyrin; Mr. S. Gaur and Mr. T. E. Mani for construction of the spectroelectrochemical cells; Financial support from the University of Calgary in the form of Teaching and Research Assistantships; Financial support from the Department of Chemistry in the form of a Graduate Scholarship.

TABLE OF CONTENTS

	PAGE
Approval Sheet.....	ii
Abstract.....	iii
Dedications and acknowledgements.....	v
Table of contents.....	vi
List of tables.....	xii
List of figures.....	xiv
CHAPTER	
1. INTRODUCTION: IRON PORPHYRINS AND HEME ENZYMES.....	1
1.1 Introduction.....	1
1.2 Structure and nomenclature of some iron porphyrins and their iron chelates.....	1
1.3 Stereochemistry-spin state relationship in iron(III) porphyrins.....	3
1.4 Classification of metalloporphyrin electronic spectra.....	8
1.5 Metal- and porphyrin ring-centred redox reactions of iron(III) porphyrins.....	10
1.6 Heme enzymes: Compound I and Compound II species.....	12
1.7 Objectives.....	16
2. EXPERIMENTAL.....	18

CHAPTER	PAGE
2.1 Porphyrins and metalloporphyrins.....	18
2.2 Electrochemical and spectroelectrochemical experiments.....	20
2.2.1 Reference electrodes.....	20
2.2.2 Electrochemical cell for voltammetric measurements.....	21
2.2.3 Solvents, supporting electrolytes, and other reagents.....	21
2.2.4 Electrochemical instrumentation.....	23
2.2.5 <i>In situ</i> Fourier-transform infrared spectroelectrochemistry.....	24
2.2.6 Other experiments.....	27
2.3 Computational details.....	29
3. THIN-LAYER ULTRAVIOLET-VISIBLE REFLECTANCE SPECTROELECTROCHEMISTRY WITH A SPINNING-GRATING MONOCHROMATOR.....	31
3.1 Introduction.....	31
3.2 Thin-layer u.v.-visible spectroelectrochemical system: Design and operation.....	33
3.3 Results and discussion.....	36
3.4 Conclusion.....	43

CHAPTER	PAGE
4. CHRONOABSORPTOMETRY OF HIGHLY COLOURED SPECIES IN NONAQUEOUS MEDIA: THE ONE-ELECTRON OXIDATION OF CHLORO(TETRAPHENYLPORPHYRINATO)IRON(III).....	47
4.1 Introduction.....	47
4.2 Theory.....	52
4.3 Details of cell construction.....	53
4.4 Double-potential step chronoabsorptometry system: Design and operation.....	55
4.5 Results and discussion.....	57
4.6 Conclusion.....	65
5. <i>IN SITU</i> INFRARED SPECTROELECTROCHEMICAL STUDIES OF TETRAPHENYLPORPHYRIN COMPLEXES CONTAINING MANGANESE, IRON, AND COBALT.....	66
5.1 Introduction.....	66
5.2 Results and discussion.....	69
5.2.1 Electrochemistry and u.v.-visible spectroelectrochemistry.....	69
5.2.2 <i>In situ</i> FTIR spectroelectrochemistry.....	73

CHAPTER	PAGE
6. THE ONE-ELECTRON OXIDATION OF DIFLUORO(TETRAPHENYLPORPHYRINATO)IRON(III): EVIDENCE FOR π -RADICAL CATION FORMATION.....	88
6.1. Introduction.....	88
6.2. Results.....	89
6.2.1 dc cyclic voltammetry.....	89
6.2.2 In-phase ac cyclic voltammetry.....	92
6.2.3 Time-resolved thin-layer u.v.-visible reflectance spectroelectrochemistry.....	93
6.2.4 <i>In situ</i> FTIR reflectance spectroelectrochemistry.....	97
6.3. Discussion.....	102
6.3.1 Site of oxidation in the difluoro iron(III) porphyrin anion - metal- versus ring-centred.....	102
6.3.2 Origin of the shift of the first oxidation potential on coordination of fluoride to fluoro(tetraphenylporphyrinato)iron(III).....	104
6.3.3 Nature of the chemical irreversibility associated with π -radical cation formation from difluoro(tetraphenylporphyrinato)iron(III).....	105

CHAPTER	PAGE
7. THE ONE-ELECTRON OXIDATION OF HYDROXY(TETRAMESITYLPORPHYRINATO)IRON(III): EVIDENCE FOR π -CATION RADICAL FORMATION.....	109
7.1 Introduction.....	109
7.2 Results.....	111
7.2.1 Cyclic voltammetry.....	111
7.2.2 Double potential step chronoabsorptometry.....	118
7.2.3 Thin-layer voltammetry and simultaneous linear potential sweep u.v.-visible spectroelectrochemistry.....	126
7.3 Discussion.....	132
7.4 Conclusion.....	135
8. DENSITY FUNCTIONAL STUDIES OF IRON(III) PORPHINES AND THEIR ONE-ELECTRON OXIDIZED DERIVATIVES.....	137
8.1 Introduction.....	137
8.2 Results and discussion.....	138
8.2.1 Relative energies of selected states of one-electron oxidized iron(III) porphines with one or two fluoride anions as axial ligands..	138
8.2.2 Molecular structures of one-electron oxidized difluoro iron(III) porphines.....	142

CHAPTER	PAGE
8.2.3 A possible spin-state/oxidation-site relationship in iron(III) porphyrins.....	146
8.2.4 $\pi \rightarrow \pi^*$ singlet transition energies of chloro(porphyrinato)iron(III).....	153
9. CONCLUSIONS AND FUTURE WORK.....	158
9.1 Introduction.....	158
9.2 Summary of progress.....	158
9.3 Future work: The 1e oxidation of σ -bonded aryl iron(III) porphyrins	163
References.....	166

LIST OF TABLES

TABLE	PAGE
1. Structures of some porphyrins and metalloporphyrins.....	5
2. Half-wave potentials for the first metal- and ligand-centred redox reactions of the 0.5 mM porphyrin complexes in 1:1 CH ₂ Br ₂ : CH ₃ CN containing 0.1 M Bu ₄ NPF ₆	71
3. Mid-infrared bands due to the porphyrin complexes.....	79
4. Position of new bands and wavenumber shifts to existing bands observed during ligand-centred oxidation of the porphyrin complexes in 1:1 CH ₂ Br ₂ : CH ₃ CN containing 0.1 M Bu ₄ NPF ₆	81
5. Position of bands which disappear and wavenumber shifts to existing bands during metal-centred oxidation of the 2 mM porphyrin complexes in 1:1 CH ₂ Br ₂ : CH ₃ CN containing 0.1 M Bu ₄ NPF ₆	85
6. Relative energy of selected states of [Fe(p)]F ₂	139
7. Relative energy of selected states of [Fe(p)]F.....	140
8. Calculated bond distances for selected difluoro iron porphines.....	143
9. Calculated bond angles for selected difluoro iron porphines.....	144

TABLE	PAGE
10. Site of one-electron oxidation in high- and intermediate-spin ferric porphyrins.....	148
11. Site of oxidation in low-spin ferric porphyrins.....	149
12. Calculated singlet transition energies of chloro(porphyrinato)iron(III)(S=5/2).....	154

LIST OF FIGURES

FIGURE	PAGE
1. The structure of the porphine dianion.....	2
2. Generalized substituted metalloporphyrin with axial ligation.....	4
3. Domed stereochemistry displayed by high-spin 5-coordinate iron(III) porphyrins.....	9
4. Enzymatic cycle of peroxidases.....	13
5. Postulated structures of Compound I and II species for peroxidases, catalases, and cytochromes P-450.....	15
6. Exploded view of electrochemical cell used for dc cyclic voltammetry.....	22
7. Cross section of assembled cell and electrode assembly.....	25
8. Front view of cell with window and retaining flange removed.....	26
9. Cell assembly and optical arrangement used for <i>in situ</i> FTIR spectroelectrochemistry.....	28
10. Schematic of the thin-layer u.v.-visible spectroelectrochemical system.....	34
11. Single scan of the visible spectrum of a holmium oxide glass filter..	38

FIGURE	PAGE
12. Thin-layer single potential step chronoabsorptometry of the one-electron oxidation of 0.46 mM [Cu(tpp)] in C ₂ H ₄ Cl ₂ -0.16 M Bu ₄ NPF ₆ . Applied potential step vs. aqueous SCE was 0.80 to 1.10 V. Spectra were collected every 1.3 s. Total electrolysis time was 12.0 s. Spectra were smoothed using a 15 point, second order Savitzky-Golay routine.....	41
13. Average absorbance at 415 nm plotted as a function of electrolysis time. Data were collected during the single potential step chronoabsorptometric experiment shown in Figure 12.....	42
14. Thin-layer linear potential sweep chronoabsorptometry of the one-electron oxidation of 0.46 mM [Cu(tpp)] in C ₂ H ₄ Cl ₂ -0.16 M Bu ₄ NPF ₆ . The applied potential was swept between 0.80 V and 1.20 V vs. aqueous SCE at a scan rate of 4.2 mV s ⁻¹ . Spectra were collected every 10.6 s. Total experiment time was 96 s. Spectra were collected using a 15 point, second order Savitzky-Golay routine.....	44

FIGURE	PAGE
15. Thin-layer linear potential sweep chronoabsorptometry of the oxidation of 0.46 mM [Cu(tp _p)] in C ₂ H ₄ Cl ₂ -0.16 M Bu ₄ NPF ₆ . The applied potential was swept between 1.24 V and 1.60 V vs. aqueous SCE at a scan rate of 4.2 mV s ⁻¹ . Spectra were collected every 10.6 s. Total experiment time was 85 s. Spectra were smoothed using a 15 point, second order Savitzky-Golay routine...	45
16. Comparison between the optical pathlength q for an external reflectance geometry and the optical pathlength x for a transmission geometry.....	50
17. Design of the chronoabsorptometric cell.....	54
18. Schematic of the double potential step chronoabsorptometric experiment.....	56
19. Absorbance-time transient for the double potential step chronoabsorptometry of [Fe(tp _p)]Cl at 410 nm. Data is an average of 64 experiments and was smoothed using 10 point averaging.....	59
20. Plot of absorbance against square root of elapsed time for the forward step of the data presented in Figure 19.....	61

FIGURE	PAGE
21. U.v.-visible spectrum of [Fe(tpp)]Cl (solid line) together with the u.v.-visible spectrum of the corresponding iron(III) porphyrin π -cation radical (circles) calculated from chronoabsorptometric data.....	63
22. U.v.-visible spectral changes associated with the one-electron oxidation of [Fe(tpp)]Cl measured using time-resolved thin-layer reflectance spectroelectrochemistry.....	64
23. Time resolved thin-layer u.v.-visible spectroelectrochemistry of the one-electron oxidation of (a) [Mn ^{III} (tpp)]ClO ₄ (b) [Mn ^{II} (tpp)] (c) [Fe ^{III} (tpp)]Cl (d) [Fe ^{II} (tpp)] (e) [Co ^{III} (tpp)]PF ₆ and (f) [Co ^{II} (tpp)] in 1:1 CH ₂ Br ₂ : CH ₃ CN containing 0.1 M Bu ₄ NPF ₆	72
24. <i>In situ</i> FTIR difference spectra observed for the one-electron oxidation of (a) [Co ^{III} (tpp)]PF ₆ and (b) [Co ^{II} (tpp)] in 1:1 CH ₂ Br ₂ : CH ₃ CN containing 0.1 M Bu ₄ NPF ₆	74

FIGURE	PAGE
25. <i>In situ</i> FTIR difference spectra observed for the one-electron oxidation of (a) $[\text{Fe}^{\text{III}}(\text{tpp})]\text{Cl}$ and (b) $[\text{Fe}^{\text{II}}(\text{tpp})]$ in 1:1 $\text{CH}_2\text{Br}_2 : \text{CH}_3\text{CN}$ containing 0.1 M Bu_4NPF_6	75
26. <i>In situ</i> FTIR difference spectra observed for the one-electron oxidation of (a) $[\text{Mn}^{\text{III}}(\text{tpp})]\text{ClO}_4$ and (b) $[\text{Mn}^{\text{II}}(\text{tpp})]$ in 1:1 $\text{CH}_2\text{Br}_2 : \text{CH}_3\text{CN}$ containing 0.1 M Bu_4NPF_6	76
27. <i>In situ</i> FTIR difference spectra observed for the one-electron oxidation of (a) $[\text{Mn}^{\text{III}}(\text{tpp})]\text{ClO}_4$ and (b) $[\text{Mn}^{\text{II}}(\text{tpp})]$ in CH_3CN containing 0.1 M Bu_4NPF_6	77
28. dc (a) and in-phase ac (b) cyclic voltammetry of 0.6 mM $[\text{Fe}^{\text{III}}(\text{tpp})]\text{F}$ in CH_2Cl_2 containing 0.1 M Bu_4NPF_6 and 3-6 mM dried $\text{Bu}_4\text{NF} \cdot x\text{H}_2\text{O}$. In (a), scan rate = 500 mV s^{-1} . In (b), scan rate = 5 mV s^{-1} , potential modulation = 10 mV p-p, 389 Hz. (c) dc cyclic voltammetry of 10 mM $\text{Bu}_4\text{NF} \cdot x\text{H}_2\text{O}$ in CH_2Cl_2 containing 0.1 M Bu_4NPF_6 (dashed line shows solvent-supporting electrolyte alone).....	91

FIGURE	PAGE
29. Time-resolved thin layer u.v.-visible reflectance spectroelectrochemistry of $[\text{Fe}^{\text{III}}(\text{tpp})]\text{F}$ + excess dried $\text{Bu}_4\text{NF} \cdot x\text{H}_2\text{O}$ in CH_2Cl_2 containing 0.1 M Bu_4NPF_6 . (a) potential held at 0.45 V, 21.2 s between spectra (b) potential held at 0.80 V, 21.2 s between spectra (c) the second of two potential steps from 0.45 V to 0.80 V, 5.3 s between scans (d) $[\text{Fe}^{\text{III}}(\text{tpp})]\text{F}$ in absence of Bu_4NF oxidized at 1.30 V, 2.7 s between spectra. All potentials are reported versus aqueous SCE.....	94
30. <i>In situ</i> FTIR difference spectra observed for the one-electron oxidation of (a) $[\text{Fe}^{\text{III}}(\text{tpp})]\text{F}$ and (b) $[\text{Fe}^{\text{III}}(\text{tpp})]\text{F}$ + excess dried $\text{Bu}_4\text{NF} \cdot x\text{H}_2\text{O}$ in CH_2Br_2 containing 0.1 M Bu_4NPF_6	98
31. Proposed reaction scheme accounting for the electrode processes associated with the electrolysis of $[\text{Fe}(\text{tpp})]\text{F}$ in the presence of excess $\text{Bu}_4\text{NF} \cdot x\text{H}_2\text{O}$	108
32. Cyclic voltammetry of 1 mM $[\text{Fe}(\text{tmp})]\text{OH}$ in dichloromethane containing (a) 0.1 M Bu_4NClO_4 and (b), (c) 0.1 M Bu_4NPF_6 . The sweep rate for all experiments was 100 mV s^{-1}	112
33. Potential programs used for voltammetric experiments A-D.....	116

FIGURE	PAGE
34. Combined potential step and sweep voltammetry of 0.25 mM [Fe(tmp)]OH in CH ₂ Cl ₂ containing 0.1 M Bu ₄ NPF ₆ . Voltammetry arising from the potential sweep portion of experiments A-D shown in Figure 33.....	117
35. Absorbance-time transient recorded at 350 nm for 0.05 mM [Fe(tmp)]OH during double potential step chronoabsorptometry of the first one-electron oxidation in CH ₂ Cl ₂ containing 0.1 M BuN ₄ PF ₆ . The transient is the average of 64 experiments. The transient was smoothed by ten point averaging.....	120
36. Plot of absorbance versus square root of time elapsed for the forward step of the data plotted in Figure 35.....	121
37. U.v.-visible spectra of [Fe(tmp)]OH (solid line) and its one-electron oxidized derivative (circles) in dichloromethane solvent.....	123
38. Time-resolved thin-layer u.v.-visible spectral changes associated with the one-electron oxidation of [Fe(tmp)]Cl in CH ₂ Cl ₂ containing 0.1 M Bu ₄ NClO ₄	124

FIGURE	PAGE
39. Thin-layer cyclic voltammetry of 0.5 mM [Fe(tmp)]OH in CH ₂ Cl ₂ containing 0.1 M Bu ₄ NPF ₆ . Sweep rate is 5 mV s ⁻¹ . Potentials are vs. the Ag-AgPF ₆ quasi reference electrode.....	127
40. Thin-layer u.v.-visible spectral changes recorded during the thin-layer cyclic voltammetry experiment shown in Figure 39 at potentials between 0.00 V to 0.42 V vs. the Ag-AgPF ₆ quasi-reference electrode on the forward sweep.....	129
41. Thin-layer u.v.-visible spectral changes recorded during the thin-layer cyclic voltammetry experiment shown in Figure 39 at potentials between 0.42 V on the forward scan and 0.51 V on the reverse scan. Potentials are reported vs. the Ag-AgPF ₆ quasi-reference electrode.....	130
42. Thin-layer u.v.-visible spectral changes recorded during the thin-layer cyclic voltammetry experiment shown in Figure 39 at potentials between 0.51 V and 0.00 V vs. the Ag-AgPF ₆ quasi-reference electrode on the reverse scan.....	131

FIGURE	PAGE
43. Reactions associated with the electrochemical oxidation of [Fe(tmp)]OH in CH ₂ Cl ₂ containing 0.1 M Bu ₄ NPF ₆	136
44. Interaction diagrams between metal-based d-orbitals and axial X ligands as well as σ-orbitals on N for an iron(IV) S=1 state and an iron(III) S=1/2 state (see text for discussion).....	151
45. Comparison of calculated transition energies using INDO/CI methods (taken from ref. 78a) based on Gouterman's 4-orbital model, and HFS-LCAO methods (present work). The experimental spectra are those due to [Fe(tpp)]Cl (solid line) and [Fe(oep)]Cl (dashed line).....	155

CHAPTER ONE

INTRODUCTION: IRON PORPHYRINS AND HEME ENZYMES

1.1 Introduction

Iron porphyrins often give brown solutions, but red or green species are also known. The origin of these colours is still not completely understood, and they remain a perplexing reminder of the subtle electronic structures present in these systems (1). It is the details of these electronic structures which are considered to be the basis of the intriguing catalytic properties of the heme enzymes - enzymes which have an iron porphyrin in their active sites (2). In turn, the catalytic properties of these biomolecules are a major reason why iron porphyrins and related systems are studied so intensively by scientists from a variety of disciplines (2, 3).

1.2 Structure and nomenclature of some porphyrins and their iron chelates

Porphyrins are compounds which are derived from porphine (Figure 1). The porphine structure consists of four pyrrole units connected by four methine bridges to form a macrocycle which is overall a dianion. If charge neutrality is maintained by two protons then the compound is referred to as the *free base*.

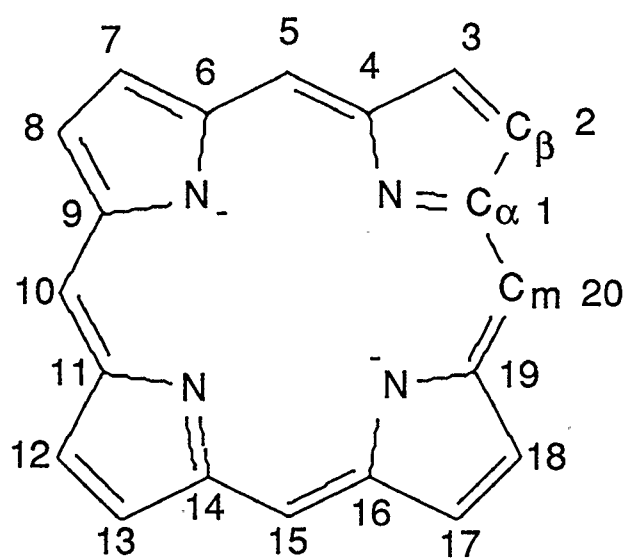


Figure 1 The structure of the porphine dianion.

Alternatively, these protons may be replaced by a wide variety of metals to form chelates known as metalloporphyrins (4).

The numbering scheme according to which substituted porphines will be named is shown in Figure 1. It is common practise to refer to the two symmetry-distinct pyrrole carbons as the α - and β -carbons. Furthermore, the methine bridges are sometimes referred to as the *meso* carbons and denoted C_m .

The structures of three common synthetic porphyrins known as 5,10,15,20-tetraphenylporphyrin (tpp), 2,3,7,8,12,13,17,18-octaethylporphyrin (oep), and 5,10,15,20-tetramesitylporphyrin (tmp), are presented in Figure 2 and Table 1. The structures of chloro(tetraphenylporphyrinato)iron(III), $[\text{Fe}(\text{tpp})]\text{Cl}$, and chloro(protoporphyrin-IX)iron(III), $[\text{Fe}(\text{pp-IX})]\text{Cl}$, are also presented. Natural porphyrins are often referred to by trivial names, such as protoporphyrin-IX. For a discussion see ref. 5.

1.3 Stereochemistry-spin state relationship in iron(III) porphyrins

Air-stable iron porphyrins contain Fe in a formal oxidation state of

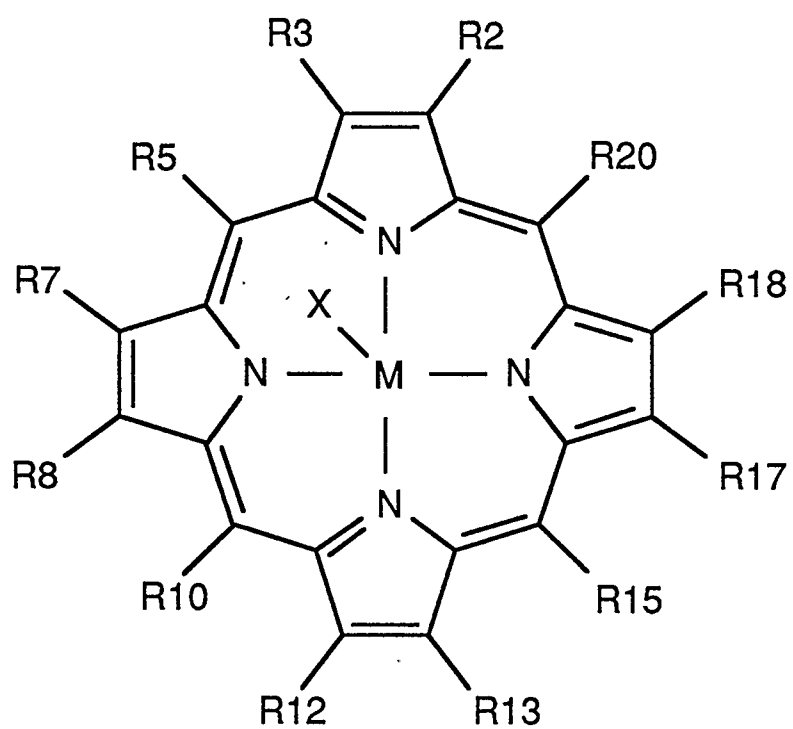


Figure 2 Generalized substituted metalloporphyrin with axial ligation.

Table 1 Structures of some porphyrins and metalloporphyrins.

	substituents complexes				
	(tpp)H ₂	(oep)H ₂	(tmp)H ₂	[Fe(tpp)]Cl	[Fe(pp-IX)]Cl
R2	H	Ethyl	H	H	CH=CH ₂
R3	H	Ethyl	H	H	Methyl
R5	Phenyl	H	Mesityl	Phenyl	H
R7	H	Ethyl	H	H	CH=CH ₂
R8	H	Ethyl	H	H	Methyl
R10	Phenyl	H	Mesityl	Phenyl	H
R12	H	Ethyl	H	H	Methyl
R13	H	Ethyl	H	H	(CH ₂) ₂ CO ₂ ⁻
R15	Phenyl	H	Mesityl	Phenyl	H
R17	H	Ethyl	H	H	(CH ₂) ₂ CO ₂ ⁻
R18	H	Ethyl	H	H	Methyl
R20	Phenyl	H	Mesityl	Phenyl	H
M	H ₂	H ₂	H ₂	Fe	Fe
X	-	-	-	Cl	Cl

+3. Since the porphyrin ligand is formally a dianion, charge neutrality is often maintained by an anionic axial ligand forming a 5-coordinate complex. A sixth axial coordination site remains available which may be occupied by either neutral or anionic species. The term *axial ligand* arises because the porphyrin ligand binds to iron (and many other metals) in a square planar tetradentate fashion and is therefore considered to provide all the equatorial ligation in these systems. It is generally the type and number of axial ligands which determine the spin-state in iron(III) porphyrins (6).

The ferric ion can adopt either quantum-admixed- ($S=5/2, 3/2$), high- ($S=5/2$), intermediate- ($S=3/2$), and low-spin ($S=1/2$) states. Quantum-admixed spin-states are favoured by very weak field axial ligands whereas strong field axial ligands favour low-spin states. A correlation between spin state and Fe-N bond distances for iron porphyrins of a given coordination number has been established (6). Thus, high-spin 5-coordinate Fe(III) porphyrins all have Fe-N distances between 2.060-2.087 Å. In contrast, six-coordinate low-spin Fe(III) porphyrins possess Fe-N bond distances of between 1.970-2.000 Å.

The spin-state adopted by an iron(III) porphyrin can be rationalized in terms of a simple molecular orbital model. The energy of a particular d configuration is given (7) by

$$E_d = \sum e_d - (n_\alpha - 1)n_\alpha K/2 - (n_\beta - 1)n_\beta K/2 \quad (1)$$

where e_d is a one-electron d-orbital energy, n_α is the number of spin-up d-electrons, n_β is the number of spin-down d-electrons, and K is the average pairwise exchange integral. The high- and low-spin iron(III) configurations are

$$(d_{x^2-y^2})^1 (d_{z^2})^1 (d_{xz,yz})^2 (d_{xy})^1 \quad (2)$$

$$(d_{x^2-y^2})^0 (d_{z^2})^0 (d_{xz,yz})^3 (d_{xy})^2$$

If the d_{xy} and $d_{xz,yz}$ orbitals are assumed to have energy t , the $d_{x^2-y^2}$ orbital to have energy b , and the d_{z^2} orbital to have energy a , the energy difference between the high- and low-spin states is approximated by

$$\Delta E_{HL} = (a - t) + (b - t) - 6K \quad (3)$$

Therefore, if the orbital excitation energy differences are small with respect to the difference in exchange energy stabilization for the two states, then the high-spin state will be favoured over the low-spin state and *vice versa*. For iron(III) porphyrins the quantity $(a - t)$ can be altered significantly by changing the nature of the axial ligation. Thus, the importance of axial ligation in determining the spin-state of a given iron(III) porphyrin complex is rationalized.

The spin-state of an iron(III) porphyrin also has consequences for the stereochemistry. Five-coordinate high-spin iron(III) porphyrins often display a *domed* stereochemistry (see Figure 3) in which the iron centre lies *ca.* 0.4 Å above the plane of the porphyrin ring (8). For 6-coordinate high-spin iron(III) porphyrins in which the metal centre is compelled to lie in the plane of the porphyrin ring, an expanded porphyrin core is observed (9). These effects can be ascribed in part to the population of the $d_{x^2-y^2}$ metal orbital (6) since for 6-coordinate low-spin iron(III) porphyrins expansion of the porphyrin core is less pronounced (9).

1.4 Classification of metalloporphyrin electronic spectra

Metalloporphyrins all produce characteristic absorptions in the ultraviolet-visible region of the spectrum denoted Q, B, N, and L bands (1). These bands dominate the electronic spectra and are thought to arise mainly from $\pi \rightarrow \pi^*$ transitions due to the π -electrons of the porphyrin ring. For *regular* metalloporphyrins containing metals with closed-shell configurations a *normal* spectrum is obtained. The normal spectrum is comprised of two visible bands, seen between 500 and 600 nm and separated by *ca.* 1250 cm^{-1} , which are called Q-bands. In addition, an intense band appears between 380 and 420 nm called the B-band or Soret band. At higher energies two additional bands denoted N and L are observed. For chelates with transition metals of

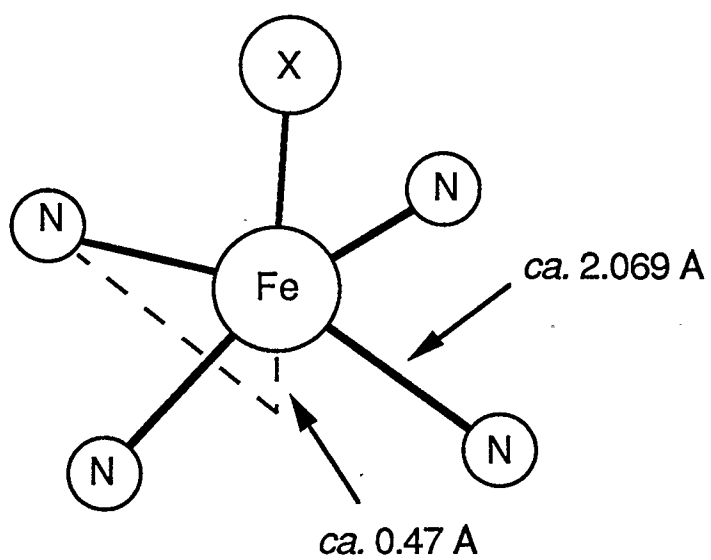


Figure 3 Domed stereochemistry displayed by high-spin 5-coordinate iron(III) porphyrins.

configuration d^m , $m = 6-9$, an irregular *hypso* spectrum is observed which is similar to the normal spectrum except that the bands are blue-shifted. Another type of *irregular* porphyrin spectrum is the *hyper* spectrum which displays additional bands at wavelengths greater than 320 nm. Iron(III) porphyrins give rise to d-type hyper spectra (1b). The assignment of the absorption bands has been investigated during this work and a discussion is presented in Chapter 8.

1.5 Metal- and porphyrin ring-centred redox reactions of iron(III) porphyrins

Metalloporphyrins containing redox-active metals like iron can undergo redox reactions centred at either the porphyrin ring or the central metal (10). The reason for distinguishing between *redox-sites* in the case of metalloporphyrin complexes follows from symmetry considerations (11). If the effective molecular symmetry of the complex is D_{4h} , then the d-based molecular orbitals and the ring-based π -molecular orbitals are respectively gerade and ungerade, and therefore cannot mix. For example, the one-electron oxidation of iron(III) porphyrins can produce *a priori* either an iron(III) porphyrin π -cation radical (12), in which an electron has been lost from the porphyrin π -system, or a high-valent Fe(IV) porphyrin (13), in which the electron has been abstracted from a d-based σ -molecular orbital. As mentioned previously, five-coordinate ferric porphyrins often adopt a domed stereochemistry which lowers the

symmetry around iron to C_{4v} . In this point group, the d-based molecular orbitals on iron can now mix with the top filled porphyrin π -molecular orbitals. The degree of this mixing will determine to what extent the molecular orbitals retain their identity as being either metal- or porphyrin ring-based. For the one-electron oxidation of iron(III) porphyrins this mixing effect appears to be quite small since iron(IV) porphyrins and iron(III) porphyrin π -cation radicals display distinct chemical and physical properties (12, 13).

The electrochemistry of iron(III) porphyrins in nonaqueous media often involves two successive reversible one-electron oxidation steps to form an iron(III) porphyrin π -cation radical and an iron(III) porphyrin π -dication, respectively. The first one-electron reduction of iron(III) porphyrins is usually metal-centred and produces the corresponding Fe(II) derivatives (10). The characterization of redox-site as being either metal- or porphyrin ring-centred normally requires spectroscopic characterization and spectroelectrochemical techniques are often employed. For a general discussion see ref. 14. In the case of metalloporphyrins, a number of diagnostic criteria have been developed to allow correct formulation of the electrogenerated product based on optical spectra, EPR, NMR, electrochemistry, magnetic moment (15), XRD (12), magnetic circular dichroism (16), infrared- (11, 17), Mossbauer- (12, 18), and resonance Raman-spectra (19).

1.6 Heme enzymes: Compound I and Compound II species

Heme proteins are enzymes which possess in common an active site comprised of an iron porphyrin moiety (*e.g.* iron protoporphyrin-IX) which is connected to the surrounding protein via axial ligation involving one or perhaps two local amino acid residues. The enzymes facilitate important biological functions such as reversible oxygen transport (*e.g.* hemoglobin, myoglobin), electron transport (*e.g.* cytochromes c), and various metabolic oxidations (*e.g.* peroxidases, chloroperoxidases, catalases, cytochromes P-450) (2a,3b).

The enzymatic cycle of peroxidases is shown in Figure 4. Peroxidases such as horseradish peroxidase catalyze the two-electron oxidation of organic substrates using hydrogen peroxide. The active intermediates in the cycle are called Compounds I and II (2a). These semi-stable species are two- and one-electron oxidized with respect to the Fe(III) porphyrin resting state. Mossbauer spectroscopy, magnetic moment measurements, electronic absorption, and NMR studies of the intermediates indicate that Compound I is an iron(IV) porphyrin π -cation radical and Compound II is an Fe(IV) porphyrin. Labelling and resonance Raman studies strongly suggest the presence of an *oxo* moiety bound to the high-valent iron in both intermediates.

Cytochromes P-450, chloroperoxidases, and catalases have also been

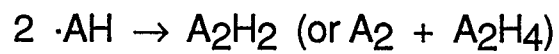
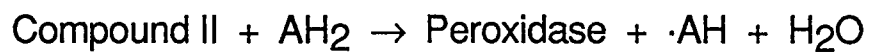
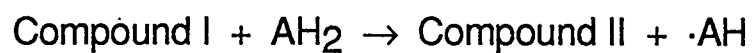
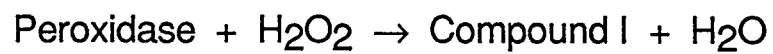
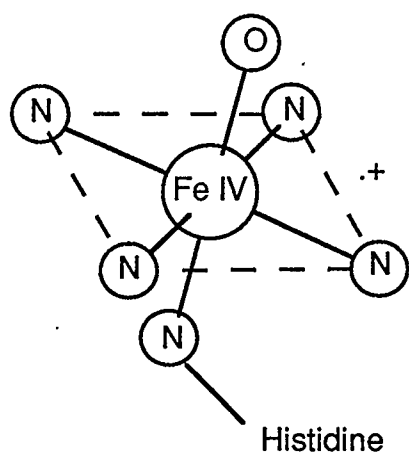


Figure 4 Enzymatic cycle of peroxidases.

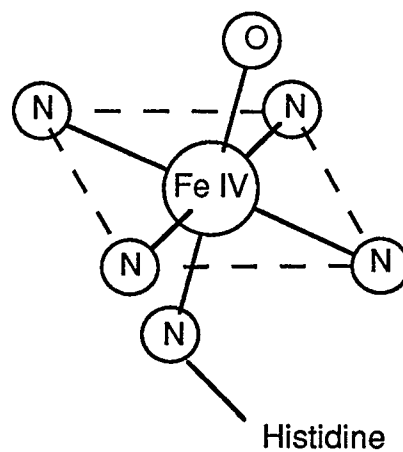
suggested to have high-valent oxo iron species formed during their catalytic cycles. The postulated structures (2a) of these high-valent intermediates are shown in Figure 5. It is observed that whereas an oxo ligand is suggested to be common to all the species, the nature of the second axial ligand varies between enzymes. In the case of peroxidases, Compound I is one-electron reduced to form Compound II. It follows that the Fe(IV) state is stabilized relative to the π -cation radical state in these species (20). However, 5-coordinate high-spin Fe(III) porphyrins with halide ions acting as axial ligands are one-electron oxidized to form iron(III) porphyrin π -cation radicals (12, 21). Therefore, it is apparent that axial ligation can play an important role in determining the relative stability of the Fe(IV) and Fe(III) porphyrin π -cation radical states (20).

High-valent oxo iron complexes which act as models of Compounds I and II have been reported by several groups (22). In addition several other iron(IV) porphyrins have been prepared with axial ligands other than oxo (13, 18, 23). Iron(III) porphyrin π -cation radical species are also well known (11, 12, 21).

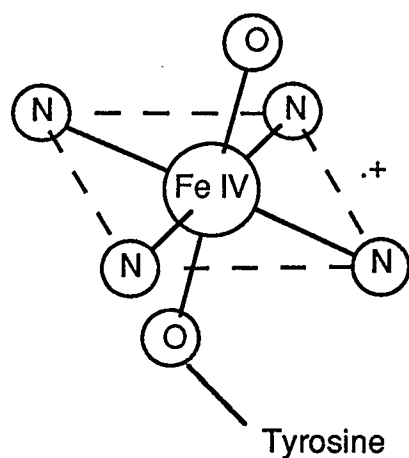
Two of the most widely used synthetic porphyrin ligands have been tetraphenylporphyrin and octaethylporphyrin (Table 1). The propensity of iron



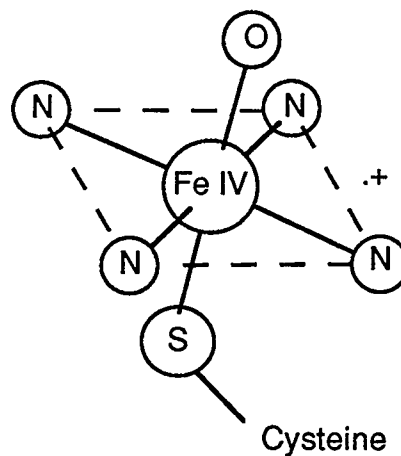
Peroxidases Compound I



Peroxidases Compound II



Catalases Compound I



Cytochromes P-450 Compound I

Figure 5 Postulated structures of Compound I and II species for peroxidases, catalases, and cytochromes P-450.

chelates produced with these ligands to form μ -oxo dimers has led to the development of more sterically hindered porphyrins such as tetramesitylporphyrin (24), as well as various 'capped' porphyrins (3f). The hope is that these systems will display chemistries more closely resembling that of the monomeric heme present in the enzyme (3f).

1.7 Objectives

This work arose out of a question as to whether iron(IV) porphyrins could be generated by direct electrochemical oxidation. A few studies had suggested that it was possible to electrochemically generate iron(IV) porphyrins provided that the iron(III) porphyrin precursor possessed the appropriate axial ligation such as one σ -bonded phenyl (23b), two fluoride anions (25) or one hydroxide anion (26). However, room temperature spectral characterization of the one-electron oxidized species could only be obtained in the case of the σ -bonded phenyl species (23b).

This laboratory has specialized in the development of spectroelectrochemical instrumentation using infrared and u.v.-visible spectroscopic probes (17). It was hoped that the application of these techniques would provide further information about the purported high-valent

would form the basis of a systematic study into the effects of axial ligation upon the anodic electrochemistry of iron(III) porphyrins.

The initial part of this work involved the development of short-timescale u.v.-visible spectroelectrochemical techniques which would be suitable to study electrogenerated species with limited stability (Chapters 3 and 4). Subsequently, an *in situ* infrared spectroelectrochemical experiment was used to study both metal- and porphyrin ring-centred electrode reactions (Chapter 5). The aim was to further develop the utility of infrared absorbance changes as a criterion for distinguishing between both types of redox process. In later studies, the developed spectroelectrochemical techniques were used to study the one-electron oxidations of difluoro(tetraphenylporphyrinato)iron(III) (Chapter 6) and hydroxy(tetramesitylporphyrinato)iron(III) (Chapter 7). Finally, density functional theory was used to investigate the relative stabilities of various one-electron oxidized states of iron(III) porphyrins as well as their molecular structures (Chapter 8). The aim was to obtain useful information about the factors influencing the relative stability of the iron(IV) and iron(III) porphyrin π -cation radical states.

CHAPTER TWO

EXPERIMENTAL

2.1 Porphyrins and metalloporphyrins

The complexes (tetraphenylporphyrinato)copper(II), [Cu(tpp)], actetato(tetraphenylporphyrinato)manganese(III), [Mn(tpp)]CH₃CO₂, μ -oxo-bis(tetraphenylporphyrinato)iron(III), [Fe(tpp)]₂O, and (tetraphenylporphyrinato)cobalt (II), [Co(tpp)], had been prepared by Adler's DMF method (27) during previous studies. The complexes were not further purified except for [Fe(tpp)]₂O which was chromatographed on alumina using CH₂Cl₂ as eluent. Chloro(tetraphenylporphyrinato)iron(III) was used as received from Porphyrin Products. Tetramesitylporphyrin, (tmp)H₂, had been prepared according to Lindsey's method (28) in a previous study. This material was chromatographed on alumina using CH₂Cl₂ as eluent, recrystallized from CH₂Cl₂-CH₃OH, and dried at 120 °C overnight prior to use.

The complex [Mn(tpp)]ClO₄ was prepared according to a literature procedure (29) by addition of 1 M aqueous HClO₄ to [Mn(tpp)]CH₃CO₂ in

CH₃OH. The product was crystallized by dropwise addition of water from a dropping funnel. The u.v.-visible spectrum was identical to that reported previously and the infrared spectrum (KBr pellet) contained $\nu(\text{ClO}_4)$ at 1131 cm⁻¹ (29). Although [Mn(tpp)]ClO₄ displayed no observable shock sensitivity (30), **perchlorate salts pose potential explosion hazards, and appropriate precautions should be observed in preparing or handling large quantities of this material.**

The complex [Fe(tpp)]F was prepared by stirring a dichloromethane solution of [Fe(tpp)]₂O with 1 M HF as previously reported (30). The reaction was followed spectrophotometrically and the product was recrystallized from heptane-dichloromethane. The u.v.-visible spectrum (CH₂Cl₂) of the product was identical to that of [Fe(tpp)]F (31) and the infrared spectrum displayed $\nu(\text{Fe-F})$ at 615 cm⁻¹ (32). The complex salt Bu₄N[Fe(tpp)]F₂ was prepared by addition of [Fe(tpp)]F to tetra-n-butylammonium fluoride trihydrate in CH₂Cl₂ according to a published method (32). Addition of dry CH₃CN to the dichloromethane solution followed by volume reduction under vacuum caused crystallization of the product. The infrared spectrum displayed $\nu(\text{F-Fe-F})$ at 485 cm⁻¹ as reported previously (32).

Chloro(tetramesitylporphyrinato)iron(III) was prepared from (tmp)H₂ and FeCl₂·4H₂O according to Adler's DMF method (27). This material was converted into the hydroxide form by stirring a 1 mM toluene solution of iron porphyrin against an equal volume of 1 M NaOH according to a published procedure (24). The u.v.-visible spectrum (toluene) was identical to that previously reported (33).

2.2 Electrochemical and spectroelectrochemical experiments

2.2.1 Reference electrodes

A saturated calomel electrode (SCE) prepared according to Adam's procedure (33a) was used as reference electrode for most electrochemical and spectroelectrochemical experiments. An Ag-AgPF₆ quasi-reference electrode was used for experiments where chloride could not be tolerated. This was prepared by soaking a Ag-wire electrode in CH₂Cl₂ containing 0.1 M Bu₄NPF₆ and a crystal of AgPF₆ for 24 h prior to use. The electrode potential was referenced to a porphyrin redox couple whose half-wave potential vs. SCE was known. Although the 1e oxidation of ferrocene is widely used as a reference redox couple, B. J. Pavelich in this laboratory has observed that its oxidation potential can shift in dichloromethane depending upon the supporting electrolyte employed.

2.2.2 Electrochemical cell for voltammetric experiments

The electrochemical cell used for most of the dc cyclic voltammetry experiments employed a Pt wire (0.75 mm diameter) working electrode positioned concentrically within the coils of a Pt wire helix counter electrode. A luggin capillary extended between two coils of the helical counter electrode to within 2 mm of the working electrode surface (see Figure 6). Two glass frits separated the luggin from a second compartment containing the reference electrode.

2.2.3 Solvents, supporting electrolytes, and other reagents

Dichloromethane (BDH) and 1,2-dichloroethane (Fisher) were shaken with alumina, distilled from P_2O_5 onto CaH_2 and stored over CaH_2 ready for use. Dibromomethane (Aldrich) was shaken with alumina prior to use. Acetonitrile (BDH Omnisolve) was shaken with alumina, stirred with CaH_2 overnight and distilled onto CaH_2 prior to use. Toluene was distilled from CaH_2 prior to use.

Solutions used for electrochemical and spectroelectrochemical experiments employed 0.1 M tetra-n-butylammonium hexafluorophosphate (Bu_4NPF_6) or tetra-n-butylammonium perchlorate (Bu_4NClO_4) as supporting electrolyte, and were purged with Argon to remove O_2 . The salt Bu_4NPF_6 was prepared by the

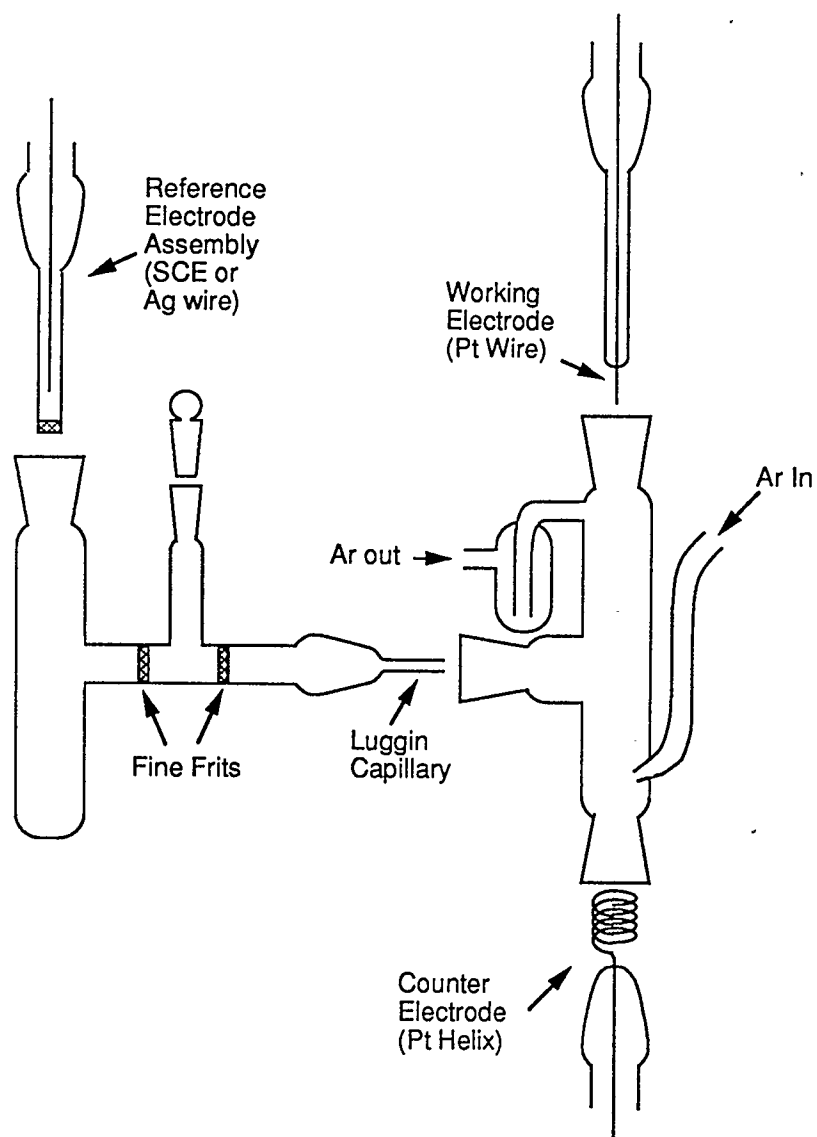


Figure 6 Exploded view of cell used for dc cyclic voltammetry.

addition of one mole equivalent of aqueous sodium hexafluorophosphate (Aldrich) to tetra-n-butylammonium bromide (Fluka) dissolved in a minimum volume of water. The white crystalline precipitate was filtered, washed with water, recrystallized twice from isopropanol-water mixtures, and dried at 110 °C *in vacuo* for several days. Tetra-n-butylammonium perchlorate was recrystallized from isopropanol-water and dried at 80 °C *in vacuo* for several days prior to use. Tetra-n-butylammonium fluoride (Aldrich) was either used as received or else dried at 40 °C for 24 h under vacuum and washed three times with dry toluene immediately prior to use. All manipulations involving solid tetra-n-butylammonium fluoride were carried out under Ar atmosphere. Tri-n-butylamine was reagent grade and was not further purified before use.

2.2.4 Electrochemical instrumentation

For all electrochemical experiments, potential control of the working electrode was achieved with a Hi-Tek DT2101 potentiostat operating in conjunction with a Hi-Tek PPR1 waveform generator. A home-built lock-in amplifier, based around an Evans Associates model 4114 phase control unit and an Evans Associates model 4110 phase sensitive detector, together with a Heath model EUW27 sine wave generator were included in the experimental apparatus for ac voltammetric experiments. Voltammetric traces were recorded with either a Linseis model LY1700 or a Kipp and Zonen 9100 X-Y-T recorder.

2.2.5 *In situ* Fourier transform infrared spectroelectrochemistry

The same cell was utilized for *in situ* Fourier transform infrared (FTIR) spectroelectrochemistry, time-resolved thin-layer u.v.-visible spectroelectrochemistry (*vide infra*), thin-layer cyclic voltammetry, and in-phase ac cyclic voltammetry (see Figures 7 and 8). The cell employs a Pt wire counter electrode, a 7 mm diameter Pt disk working electrode polished to a mirror finish, and a CaF_2 optical window, which is transparent from the ultraviolet portion of the electromagnetic spectrum through to *ca.* 1000 cm^{-1} in the infrared. Thin layer cavities of variable thickness are maintained between the surface of the electrode and the window, except for experiments which required conditions of semi-infinite linear diffusion where the working electrode was pulled far back from the cell window. The effective optical pathlength of the cell used in the thin layer spectroelectrochemical experiments varied in the range 50-100 μm .

Infrared spectroelectrochemical measurements employed a Nicolet 8000 FTIR spectrometer and a liquid-nitrogen cooled narrow-range mercury cadmium telluride detector. Two front-surfaced gold mirrors were used to direct the infrared beam onto the Pt electrode and back to the detector as shown in Figure 9. The infrared difference spectra associated with the redox couples were determined by collecting and averaging a set of 128 interferograms at each of two potentials, E_1 and E_2 , selected to lie 120 mV on either side of the

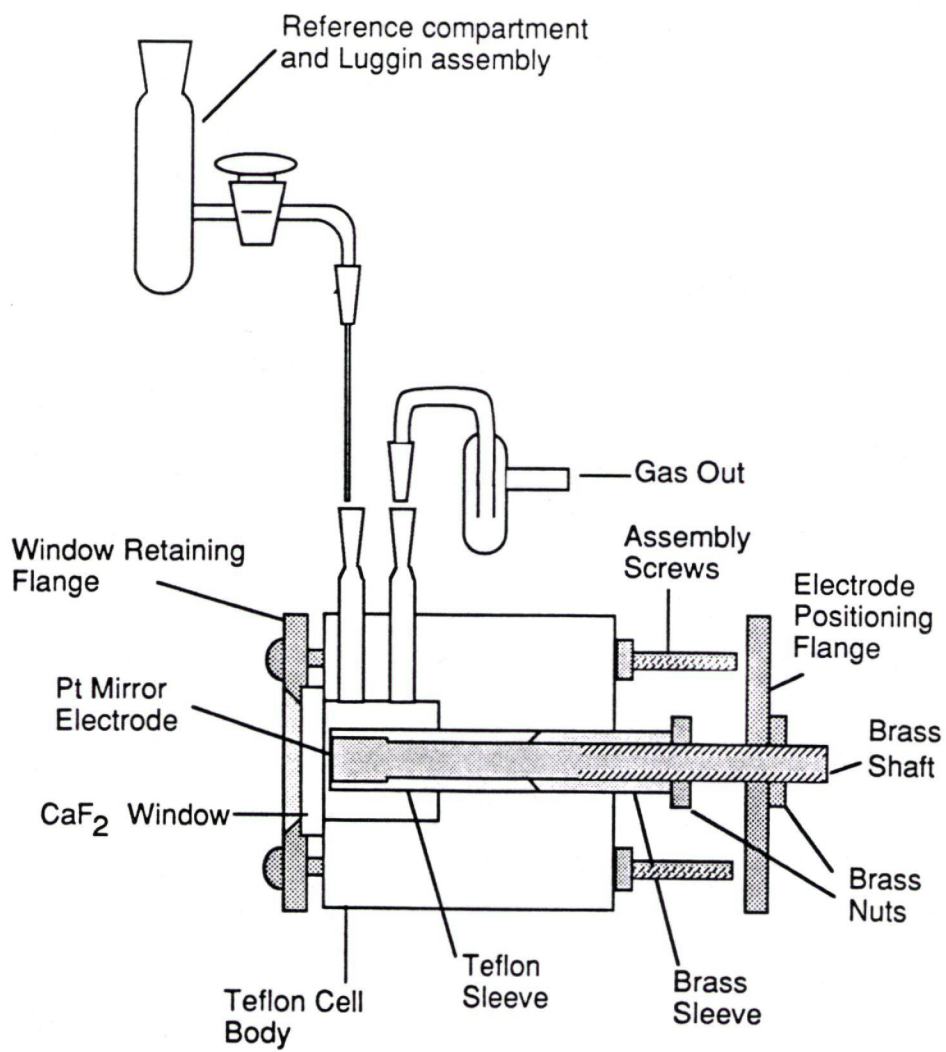


Figure 7 Cross section of assembled cell and electrode assembly.

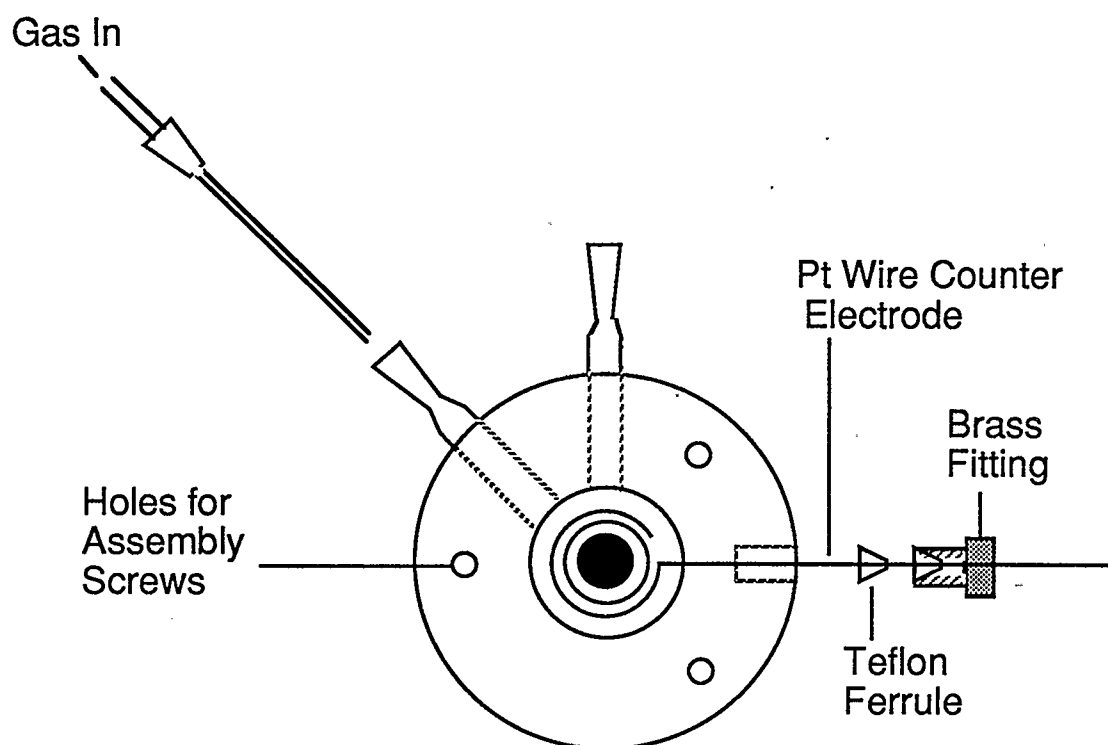


Figure 8 Front view of cell with window and retaining flange removed.

observed half-wave potential for the couple. The potential was automatically switched under computer control on completing collection of the first set of spectra. To allow time for complete electrolysis, a 30 s delay was invoked before initiating acquisition of the second set of spectra. The resulting averaged Fourier-processed spectrum at E_2 was then ratioed against the averaged Fourier-processed background spectrum collected at the initial potential E_1 . Taking the logarithm and multiplying the result by -1 afforded the difference in absorbance, $\Delta A = A(E_2) - A(E_1)$, between the original and electrolyzed solutions.

2.2.6. Other experiments

The instrument utilized for time-resolved thin-layer u.v.-visible spectroelectrochemistry employs a Rofin-Sinar model RSO 6101 spinning-grating monochromator. The details of its construction and implementation are fully described in Chapter 3. The instrumentation used for double potential step chronoabsorptometry has been fully discussed in Chapter 4. Diffusion coefficients for iron(III) porphyrins were calculated from chronoamperometric data. The electrode area of the chronoabsorptometric cell was calculated from chronoamperometric data for 4 mM $[\text{Fe}(\text{CN})_6]^{4-}$ in water containing 0.1 M KCl. The diffusion coefficient of $[\text{Fe}(\text{CN})_6]^{4-}$ is known under

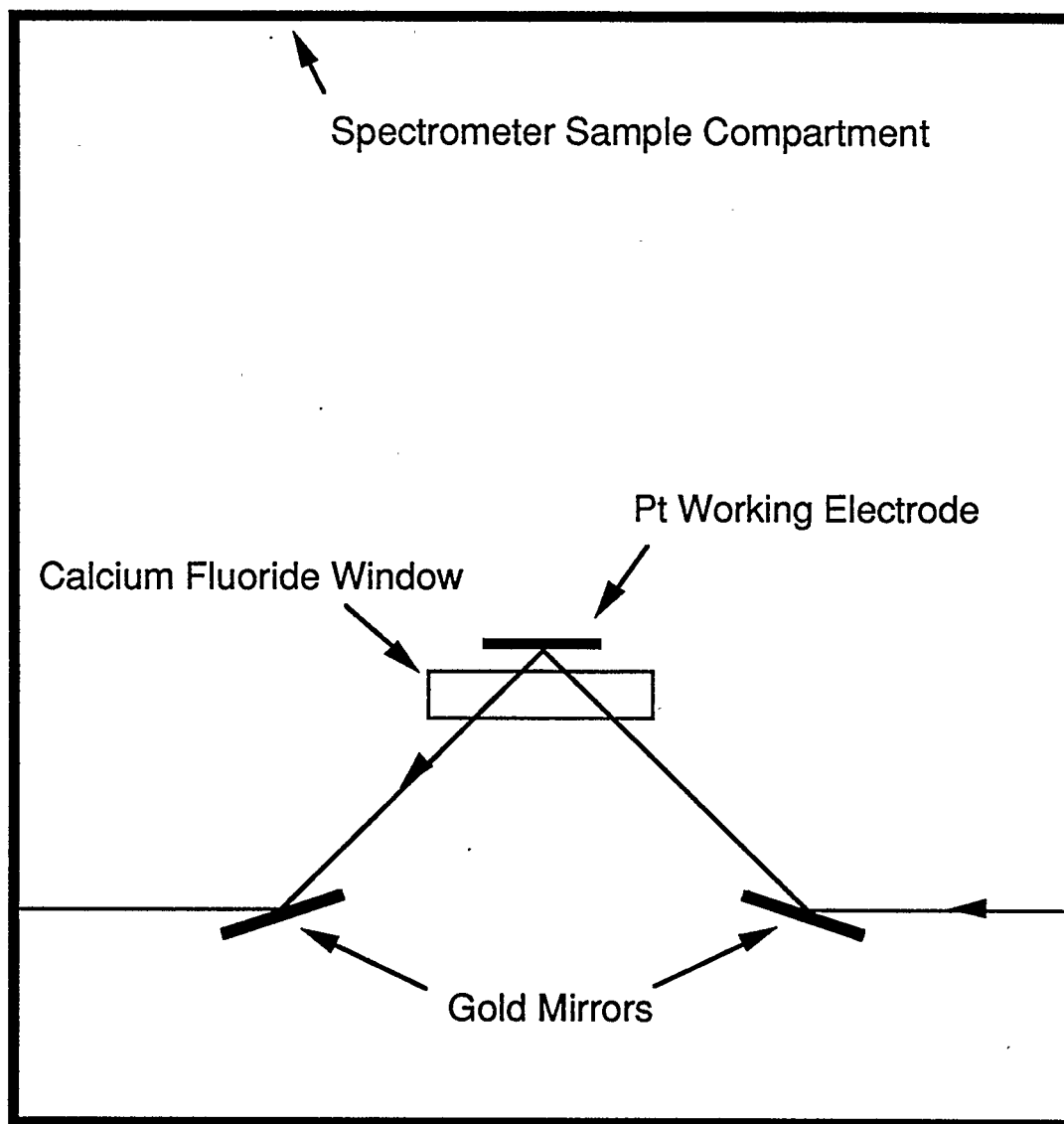


Figure 9 Cell assembly and optical arrangement used for *in situ* FTIR spectroelectrochemistry.

these conditions (33). Transmission infrared spectra were recorded using a Nicolet 5DX Fourier transform infrared spectrometer. A Cary 16 spectrophotometer was used to measure u.v.-visible spectra.

2.3 Computational details

The reported molecular orbital calculations were all carried out by Dr. T. Ziegler utilizing the HFS-LCAO program system developed by Baerends *et al.* (34, 35) and vectorized by Ravenek (35b). The numerical integration procedure applied for the calculations was developed by Becke (36). All molecular structures were optimized within the C_{2v} symmetry group. The geometry optimization procedure was based on the method developed by Versluis and Ziegler (37). An uncontracted triple ζ -STO basis set was employed for iron, whereas the ligand atoms were represented by a double ζ -STO basis set. The $1s^2 2s^2 2p^6$ configuration on Fe and the $1s^2$ configuration on C and N were assigned to the core and treated by the frozen-core approximation (34). A set of auxiliary s, p, d, f and g STO functions (38) centered on all nuclei was used in order to fit the molecular density and to present the Coulomb and exchange potentials accurately in each SCF cycle. Geometry optimizations and SCF calculations were based on the Local Density Approximation (LDA) (39) in the representation given by Vosko *et al.* (40). Energy differences were calculated

by including non-local corrections to exchange (41) and correlation (42).

CHAPTER THREE

THIN-LAYER ULTRAVIOLET-VISIBLE REFLECTANCE SPECTROELECTROCHEMISTRY WITH A SPINNING-GRATING MONOCHROMATOR

3.1 Introduction

Thin-layer u.v.-visible spectroelectrochemistry is an established electroanalytical technique for the *in situ* spectroscopic study of redox processes (43). To take full advantage of the short electrolysis times possible in thin-layer spectroelectrochemical cells, it is desirable to utilize optical analyzers which have the capability of acquiring and processing several complete spectra in a few seconds. Recent improvements in the design of thin-layer cells allow very short electrolysis times, even in highly resistive solvent-supporting electrolyte systems (17a, 44-46). These advances further increase the possibilities for the combination of thin-layer electrochemistry with techniques for rapid spectral acquisition.

To date, rapid spectral acquisition in spectroelectrochemical experiments has been accomplished using two different types of optical instrument. Rapid scanning spectrophotometers, based on oscillating galvanometer mirrors, have

been utilized in thin-layer spectroelectrochemical experiments (47-49), as well as in diffusion-controlled experiments with optically transparent electrodes (50-54). More recently, linear diode array multichannel optical analyzers, which allow for simultaneous wavelength detection, have been utilized in thin-layer spectroelectrochemistry (45a, 46).

The proposed study of the effects of axial ligation upon the anodic electrochemistry of iron(III) porphyrins was considered to require the spectral characterization of semi-stable intermediates (25, 26). As a means of meeting this requirement, an alternative approach to doing short timescale thin-layer spectroelectrochemistry using a commercially available spinning-grating monochromator was investigated. This monochromator utilizes a diffraction grating mounted directly onto the shaft of a dc servo motor. The motor rotates continuously at approximately 700 rpm, allowing the acquisition of complete spectra at intervals of 80 to 100 ms. Also, a variety of triggering options are provided which allow convenient interfacing with computers and electrochemical equipment. These features, coupled with the low cost of the device, made it an attractive alternative to other commercially available rapid spectral acquisition systems for use in spectroelectrochemical experiments.

3.2 Thin-layer u.v.-visible spectroelectrochemical system: design and operation

A schematic of the thin-layer u.v.-visible spectroelectrochemical system is shown in Figure 10. The optical design is analogous to that of a single-beam spectrophotometer, with the exception that the 'sample' (spectroelectrochemical cell) and monochromator positions are reversed.

A 75 watt xenon arc lamp is used as a light source. The radiation passes through a second order blocking filter (2.00 cm acetone) and is focused onto a Pt mirror disk working electrode in the thin-layer spectroelectrochemical cell by means of a spherical mirror. The angle of incidence is about 45°. The use of a reflectance-type cell, as opposed to the more common transmission-type cell employing optically transparent electrodes, provides greater sensitivity to small absorbance changes by virtue of the longer optical pathlengths achieved. The details of the construction of the cell have already been discussed in the experimental section (Chapter Two). The only modification in this work is the inclusion of a thin black card positioned normal to the electrode surface and the plane of incidence of the optical beam, which serves to deflect stray light reflected from the surface of the quartz window. Light which is specularly reflected from the electrode surface is focused onto the entrance slit of a Rofin-Sinar RSO 6101 spinning grating monochromator by

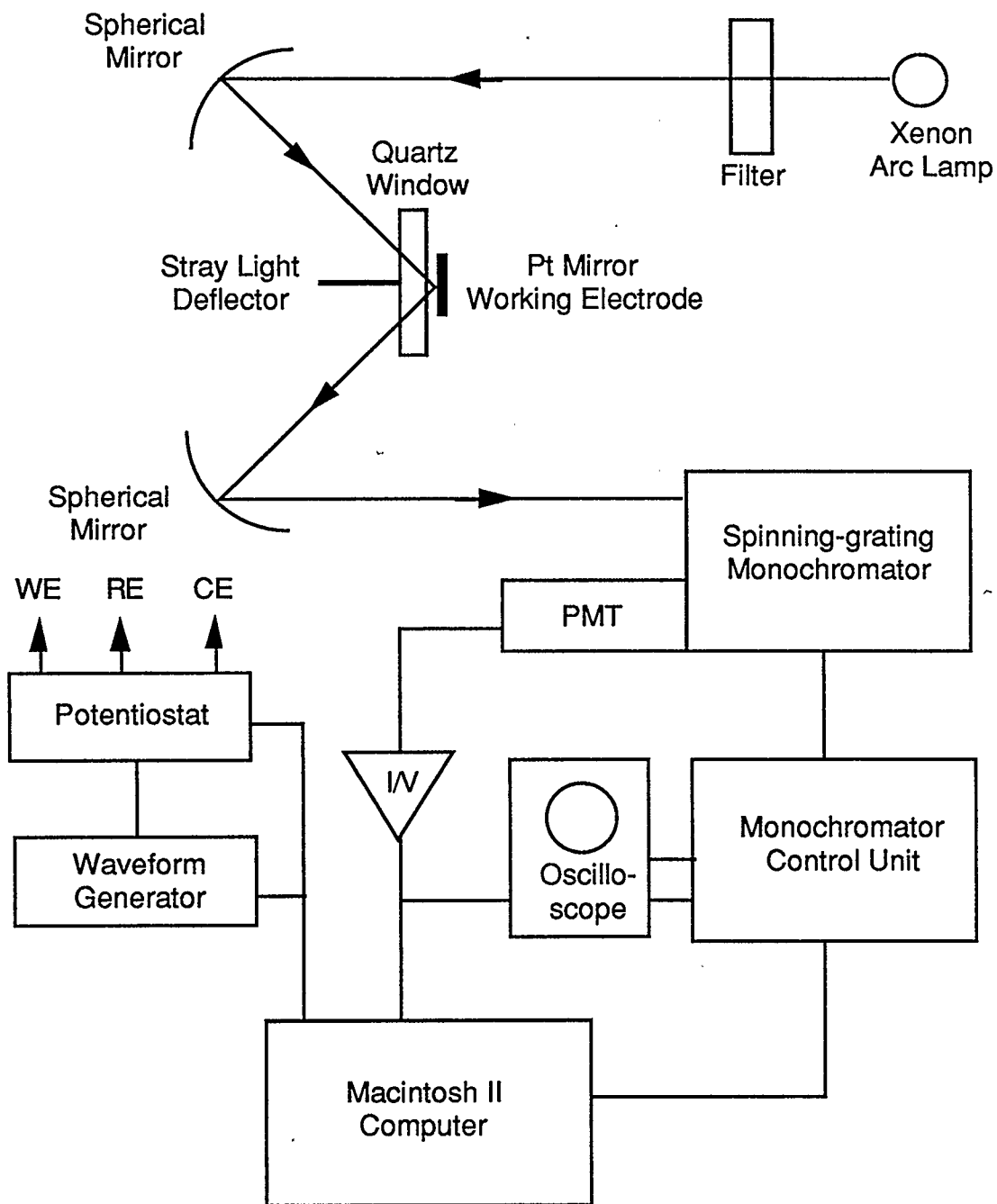


Figure 10 Schematic of the thin-layer u.v.-visible spectroelectrochemical system.

means of a second spherical mirror. The blaze wavelength of the monochromator grating is 500 nm. A Hamamatsu R268 photomultiplier tube (PMT) detector is placed at the monochromator exit slit. The anode current of the PMT is amplified with a Keithley model 427 current amplifier.

The output of the current amplifier is monitored with a Macintosh II computer fitted with a G. W. Instruments Macadios II analog-digital interface card. The interface card allows analog data to be digitized and placed into memory at rates of up to 200 kHz. As configured, the full-scale voltage recognized by the 12-bit ADC is 10 V. In order to gain maximum benefit from the 12-bit resolution, the output of the current amplifier is monitored with an oscilloscope and the maximum signal is adjusted to slightly less than ten volts by varying the PMT supply voltage.

The spinning grating monochromator is used in conjunction with a Rofin Sinar 6200 monochromator control unit, which provides a flash trigger voltage during each grating rotation. This pulse is used to synchronize the various aspects of the spectroelectrochemical experiment. On the first trigger pulse following initiation of the experiment by the operator, the computer either applies a preselected voltage step directly to the adder input of a Hi-Tek model DT 2101 potentiostat, or triggers the start of a voltage ramp as derived from a

Hi-Tek model PPRI waveform generator. Subsequent pulses from the monochromator initiate the acquisition of a 300 point integer array by the computer at a rate of 7 μ s per point. The time between trigger pulses is sufficient to allow the data to be converted to floating point format and added into a second array, providing real-time signal averaging. The time at which the flash trigger occurs in relation to the grating position is variable in one nm increments by means of a thumbwheel switch on the monochromator control unit. This allows convenient control of the wavelength range scanned in the experiment. By appropriate ratioing of sample and background energy spectra collected in this manner, both transmittance and absorbance spectra may be obtained. The system is controlled using a Think Technologies Lightspeed Pascal computer programme which accesses the Macadicos II input-output and data manipulation libraries. Wavelength calibration of the monochromator is performed by measuring the absorption spectra of several narrow bandwidth filters.

3.3 Results and discussion

The shortest period of rotation obtainable with the monochromator was determined by measuring the time interval between successive trigger pulses, and was found to be 83 ms. It is important to note, however, that the entire u.v.-visible wavelength region appears at the exit slit of the monochromator for

only a small fraction (*ca.* 3 %) of this time. The wavelength range covered in the present experiments (369 to 617 nm) is thus scanned in only 2.1 ms, so that the light beam is only sampled for 2.5 % of the total time. When compared to a linear diode array, which samples light continuously, this amounts to a considerable loss of throughput and therefore, inherently poorer signal-to-noise ratios. It was envisaged, however, that the use of a PMT, which has greater sensitivity than a photodiode, in conjunction with a high intensity light source, would at least partially compensate for this effect.

The short time in which the wavelength region of interest is scanned requires that a fast response current amplifier be used in order to avoid loss of spectral resolution and wavelength accuracy. The Keithley model 427 amplifier used in this work has a rise time of 0.01 ms. Also, the ADC must be capable of operating at high sampling rates. The sampling time of 7 μ s utilized in the present experiments provides for a digital resolution of 0.81 nm per point. Figure 11 illustrates the visible spectrum of a holmium oxide glass filter obtained from a single scan. The spectrum was determined with the filter placed in the optical path between the light source and the thin-layer spectroelectrochemical cell so that the throughput would closely match that expected in a typical spectroelectrochemical experiment. A 0.2 mm monochromator slit width was employed, giving a spectral bandwidth of 2 nm.

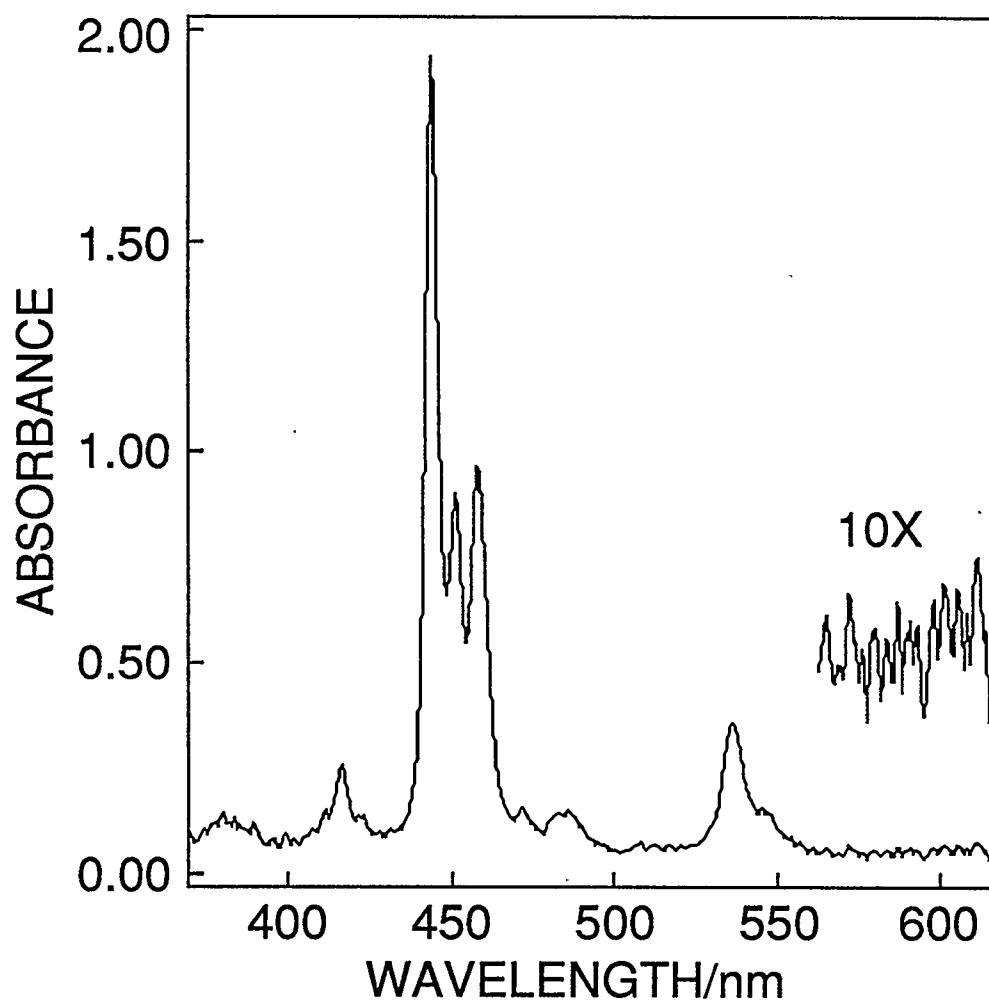


Figure 11 Single scan of the visible spectrum of a holmium oxide glass filter.

The unusually sharp absorption peaks in the spectrum are clearly resolved. The overall resolution provided by the system is thus more than adequate for most condensed phase u.v.-visible experiments. No detectable change in the position of peak maxima was observed over a period of 2-3 hours, indicating excellent stability in the rotation rate of the grating. The maximum peak-to-peak noise level evident in the spectrum is only 0.03 absorbance units, even though the spectrum was acquired in 2.1 ms during a single scan. This figure may, of course, be improved upon using signal averaging and digital filtering techniques.

In order to demonstrate the performance of the system during an actual spectroelectrochemical experiment, the anodic spectroelectrochemistry of 0.46 mM [Cu(tpp)] in $\text{C}_2\text{H}_4\text{Cl}_2$ -0.16 M Bu_4NPF_6 was studied. In this solvent-supporting electrolyte system, [Cu(tpp)] undergoes two successive one electron oxidations with half wave potentials of 0.94 and 1.32 V vs. SCE. The two electrode reactions correspond to the stepwise formation of a porphyrin ring π -radical cation and π -dication (55). Both processes were studied using thin-layer single potential step chronoabsorptometry, as well as thin-layer linear potential sweep chronoabsorptometry. In these techniques, either a potential step or a potential ramp is applied to the Pt mirror working electrode and the absorbance changes in the adjacent thin electrolyte layer are monitored with

time.

The thin-layer single potential step chronoabsorptometry of the first oxidation is shown in Figure 12. The optical pathlength was calculated to be 63 μm for this and subsequent experiments, which corresponds to a thin-layer thickness of ca. 22 μm (17a). During the electrolysis time of 12.0 seconds, it was possible to collect 9 spectra, each obtained by averaging 16 successive scans. Four isosbestic points are observed at 407, 428, 529, and 551 nm. The spectral changes are typical of π -radical cation formation as seen for a number of tpp complexes (55). The short timescale is clearly adequate to define the spectral changes occurring, provided the signals are of sufficiently high absorbance.

Figure 13 presents the average absorbance at 415 nm observed during the chronoabsorptometric experiment from which the spectra of Figure 12 were recorded. It is evident that the absorbance change during the first 1.3 second interval is considerably less than that observed in the next few intervals. Such delays in the onset of the electrolysis have been observed in even the fastest thin-layer cells (44b), and result from the high solution resistivity within the thin-layer cavity. This high resistivity results in long RC time constants associated with charging the double-layer capacitance at various points on the electrode. By virtue of the associated solution iR drop, it delays the charging of

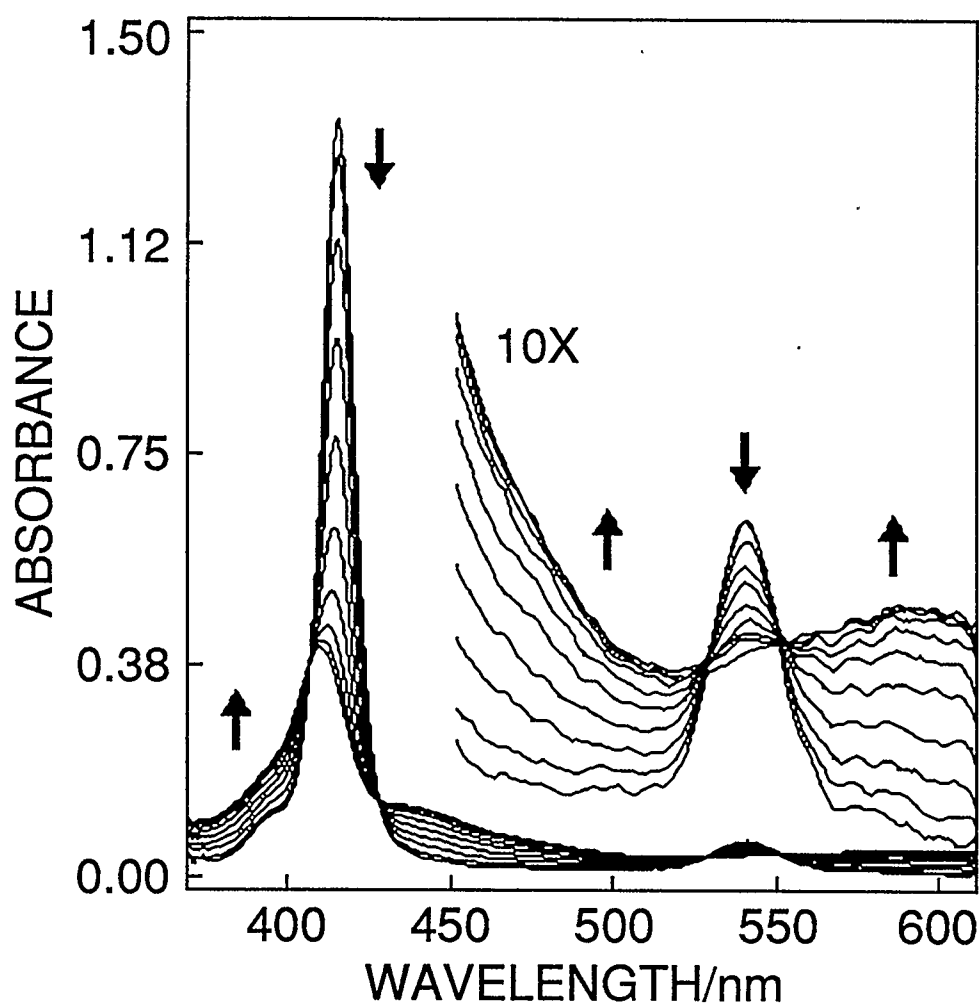


Figure 12 Thin-layer single potential step chronoabsorptometry of the one-electron oxidation of 0.46 mM [Cu(tpb)] in C₂H₄Cl₂-0.16 M Bu₄NPF₆. Applied potential step vs. aqueous SCE was 0.80 V to 1.10 V. Spectra were collected every 1.3 s. Total electrolysis time was 12.0 s. Spectra were smoothed using a 15 point, second order Savitzky-Golay routine.

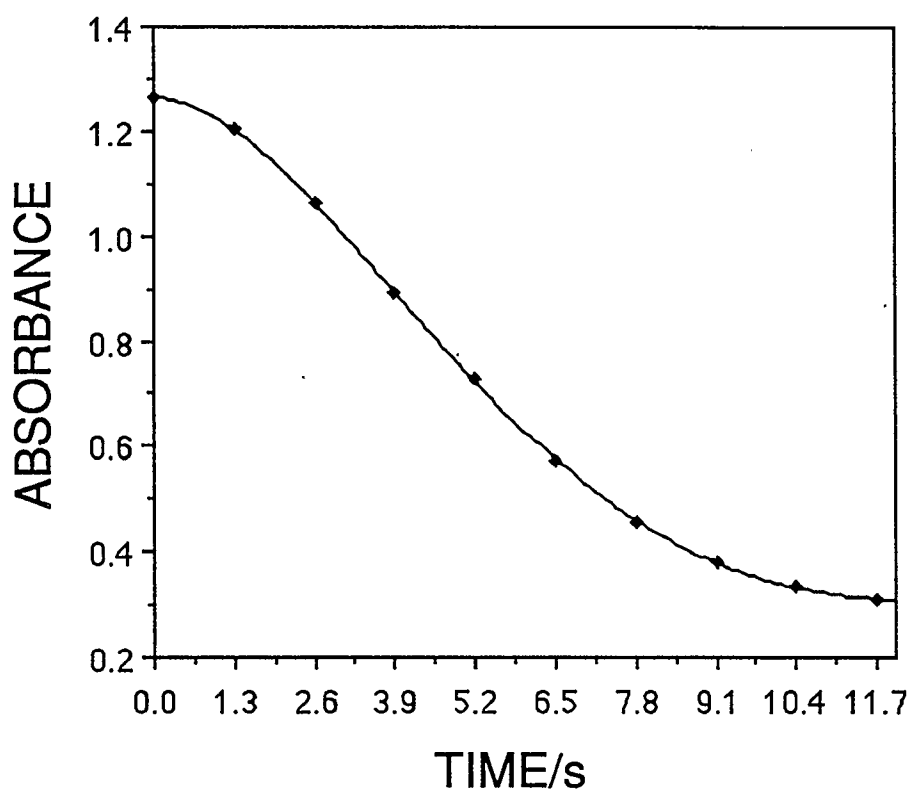


Figure 13 Average absorbance at 415 nm plotted as a function of electrolysis time. Data were collected during the single potential step chronoabsorptometric experiment shown in Figure 12.

the double-layer capacitance and onset of electrolysis at points on the working electrode surface placed further from the counter electrode surface until current flow to points closer to the counter electrode subsides. (More complete discussions of this effect can be found in refs. 17a, 44a, 56, and 57.) Thus, under the conditions of this experiment, the shortest time frame accessible is limited by the electrochemical response rather than the rate at which spectra may be acquired.

Provided the electrogenerated intermediates under study are sufficiently stable, it is possible to improve the S/N levels in the spectra by employing a linear sweep potential program. Through an appropriate choice of scan rate, the experiment time may be extended thus affording opportunity for further signal averaging. Figures 14 and 15 show the spectral changes observable during the first and second one electron oxidations of [Cu(tp_p)] respectively. The spectral changes associated with the second oxidation (Figure 15) show three isosbestic points at 379, 524, and 543 nm. The spectral changes are typical of π -dication formation (55).

3.4 Conclusion

The thin-layer spectroelectrochemical system constructed using a spinning grating monochromator, appears to provide an economical and versatile means

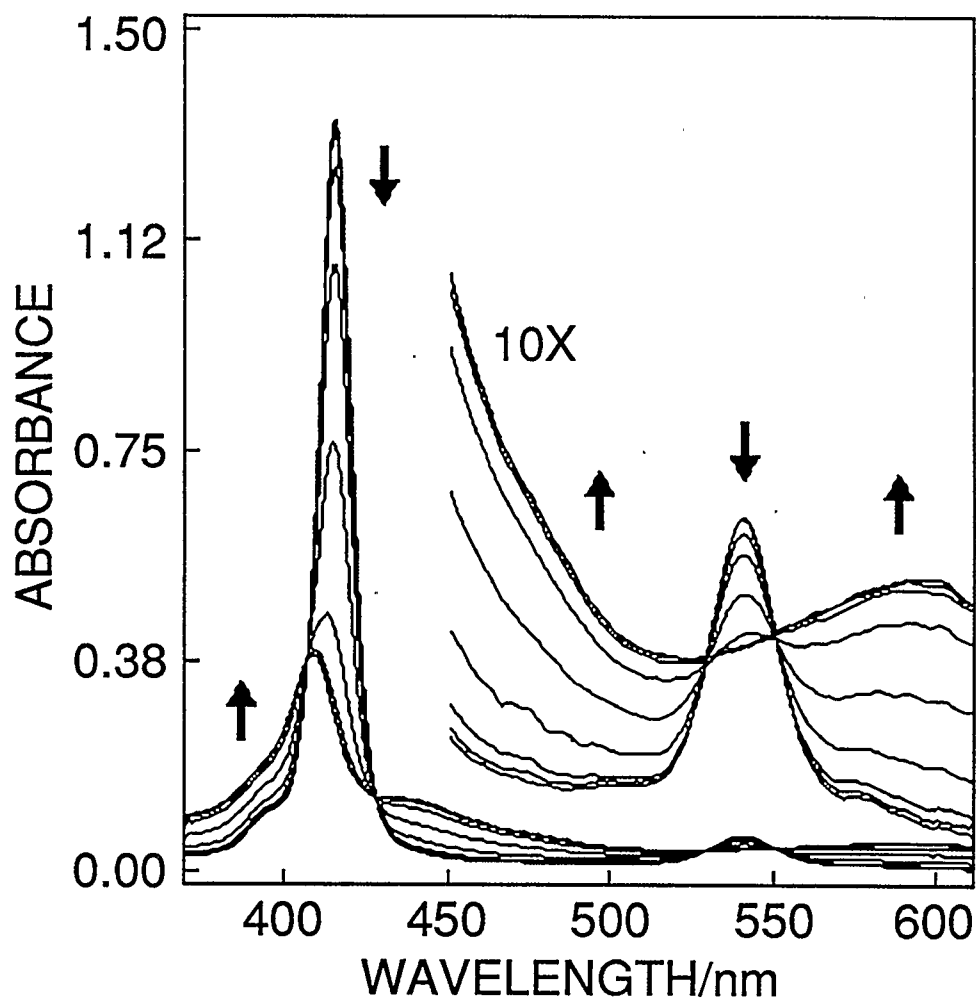


Figure 14 Thin-layer linear potential sweep chronoabsorptometry of the one-electron oxidation of 0.46 mM [Cu(tpp)] in C₂H₄Cl₂-0.16 M Bu₄NPF₆. The applied potential was swept from 0.80 to 1.20 V vs. aqueous SCE at a scan rate of 4.2 mV s⁻¹. Spectra were collected every 10.6 s. Total experiment time was 96 s. Spectra were smoothed using a 15 point, second order, Savitzky-Golay routine.

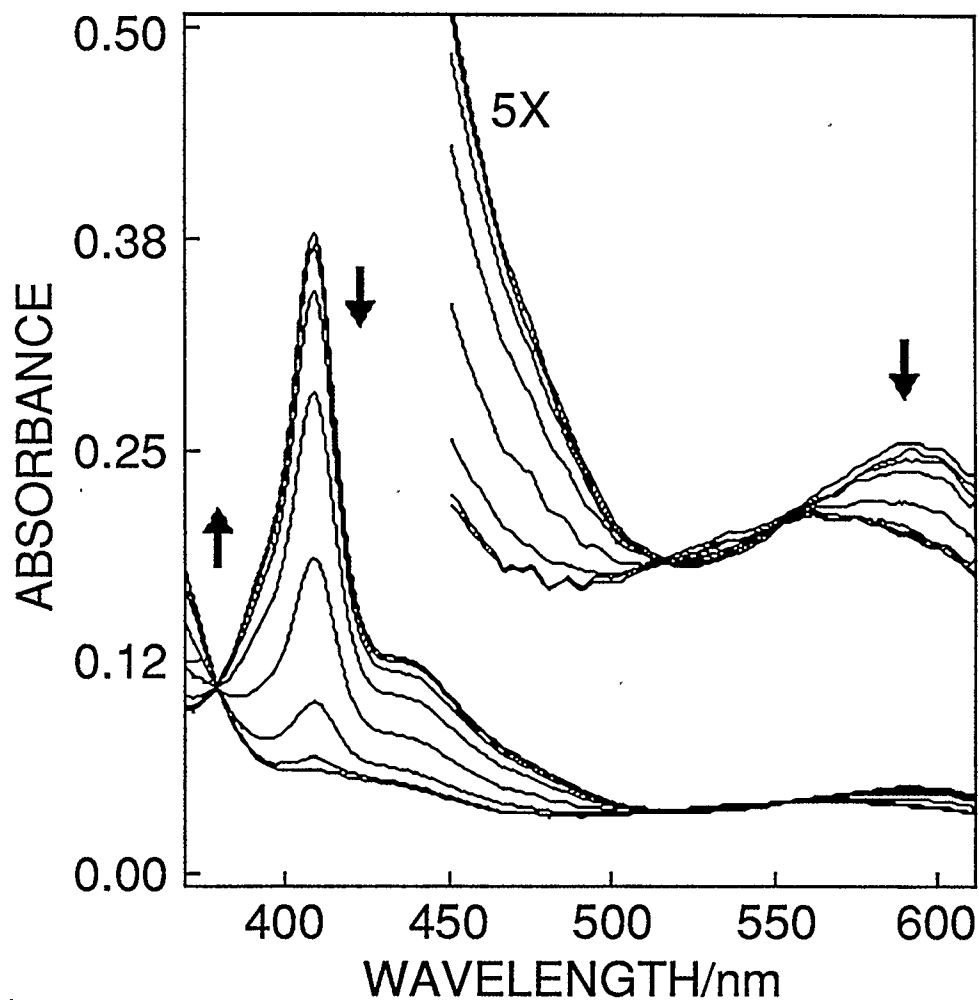


Figure 15 Thin-layer linear potential sweep chronoabsorptometry of the oxidation of 0.46 mM [Cu(tp)] in C₂H₄Cl₂-0.16 M TBAPF₆. The applied potential was swept between 1.24 and 1.60 V vs. aqueous SCE at a scan rate of 4.2 mV s⁻¹. Spectra were collected every 10.6 s. Total experiment time was 85 s. Spectra were smoothed using a 15 point, second order Savitzky-Golay routine.

of performing short timescale thin-layer spectroelectrochemistry. The quality of the spectral data obtained using the system, is sufficient to characterize the spectral properties of electrogenerated intermediates which are stable on the second timescale.

The system is simple to assemble and experimentally flexible. Modification of the experiment to scan different wavelength regions in the u.v.-n.i.r. range could easily be accomplished by altering the source, detector, and blaze wavelength of the grating in the monochromator unit. Furthermore, the variety of triggering and data acquisition options offered by the computer and monochromator control unit, provide scope for a variety of spectroelectrochemical experiment designs.

CHAPTER FOUR

CHRONOABSORPTOMETRY OF HIGHLY COLOURED SPECIES IN NONAQUEOUS MEDIA: THE ONE-ELECTRON OXIDATION OF CHLORO(TETRAPHENYLPORPHYRinato)IRON(III)

4.1 Introduction

Chronoabsorptometry using single and double potential steps are widely used techniques for the *in situ* spectroscopic study of redox processes under conditions of semi-infinite linear diffusion (43, 58). In single potential step chronoabsorptometry the potential is stepped to a region where the redox reaction under investigation proceeds at a diffusion-controlled rate (Cottrell experiment) and any absorbance changes in the diffusion layer are monitored as a function of time. In double potential step chronoabsorptometry the potential is subsequently stepped back to the original potential after a defined delay τ and changes in absorbance are monitored throughout the potential perturbation.

Most studies to date using chronoabsorptometric methods under conditions of semi-infinite linear diffusion have involved electrode reactions in which a coloured species is produced from a precursor with negligible absorbance at

the analytical wavelength (43, 58). This condition ensures maximum light throughput and therefore optimum signal-to-noise ratios in the absorbance-time transients (59). Furthermore, since there is no restriction upon the light path through the spectroelectrochemical cell, it is easier to produce designs in which resistance effects are minimized thus ensuring a fast electrochemical response (58).

If the starting material absorbs at the analytical wavelength(s) then a loss of light throughput must occur which will result in lower signal-to-noise ratios. From a consideration of Beer's law it is seen that the analyte absorbance can be lowered by either shortening the total cell pathlength or lowering the bulk analyte concentration.

Some workers using OTE's have shortened the total optical pathlength by using a light pipe (*e.g.* a quartz tube) to transmit light to within a short distance of the OTE surface without loss of throughput due to absorption by the analyte (59-61). However, this results in an increase in the cell resistance which will increase the time constant associated with charging the double-layer capacitance and produce uneven potential distribution at the working electrode because of iR losses (59). These effects will lead to non-ideal electrochemical response which may limit the utility of the absorbance-time results (59-61).

These effects will become particularly severe if highly resistive solvent-supporting electrolyte systems are required (17a, 44, 56, 57). Lowering the analyte concentration can improve the optical throughput but will also lower the absorbance change produced on electrolysis and thereby reduce the signal-to-noise ratio. In addition, any effects due to impurities or adsorption effects will become more significant under conditions of high dilution.

The use of an external reflectance geometry (58) as opposed to a transmission geometry means the light passes through the diffusion layer twice which improves the sensitivity by a factor of $2/\cos\theta$ where θ is the angle of incidence of the light beam relative to the electrode surface (see Figure 16). Thus, an external reflectance geometry compensates to some extent for the loss in sensitivity entailed by a reduction in the bulk analyte concentration. Using external reflectance geometry it is possible to position the counter electrode such that all points are equidistant from the working electrode. This results in uniform current distribution and good electrochemical response. This is not possible in most transmission cell designs since the counter electrode would block the light path.

During our studies of the anodic oxidation of iron(III) porphyrins it became necessary to accurately map point-by-point the electronic spectra of the

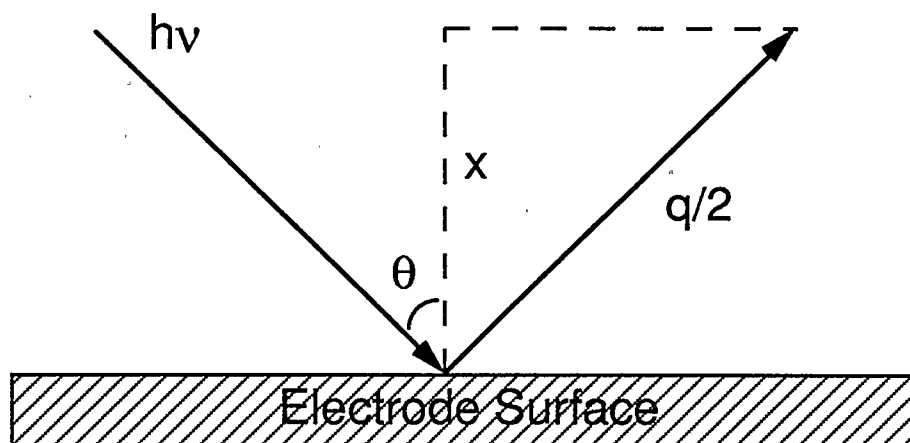


Figure 16 Comparison between the optical pathlength q for an external reflectance geometry and the optical pathlength x for a transmission geometry.

electrogenerated products over the u.v.-visible range in short-timescale experiments. Since porphyrins give rise to u.v.-visible absorbance bands with molar absorptivities in the range 10^3 - $10^6 \text{ M}^{-1} \text{ cm}^{-1}$ (1), it was necessary to design a cell in which the total optical pathlength was minimized. In addition the requirement that the cell give a fast electrochemical response even when using a highly resistive nonaqueous solvent-supporting electrolyte meant that the cell had to have a design in which effects due to solvent resistance were minimized.

A cell design based upon an external reflectance optical geometry which was considered to meet the requirements outlined above was incorporated into a potential step chronoabsorptometric experiment. In order to demonstrate typical results attainable from the potential step chronoabsorptometry experiment, the changes to the u.v.-visible spectrum accompanying the 1e oxidation of chloro(tetraphenylporphyrinato)iron(III), $[\text{Fe}(\text{tpp})]\text{Cl}$, were measured using the system. The chronoabsorptometric results are compared with those from time-resolved thin-layer u.v.-visible spectroelectrochemistry (also termed single potential step thin-layer chronoabsorptometry) for the same electrode reaction.

4.2 Theory

Consider a one electron reversible oxidation reaction in which a colourless species R is converted to a coloured species O. The absorbance-time profile for a Cottrell experiment performed at an optically transparent electrode (OTE) using a transmission geometry is given by

$$A(t) = [2 \cdot \epsilon \cdot C^* \cdot D^{1/2} \cdot t^{1/2}] / \pi^{1/2} \quad (4)$$

where A is the absorbance, ϵ is the extinction coefficient, C^* is the bulk concentration of species R, D is the diffusion coefficient of species R, and t is the time elapsed (14).

If both forms of the redox couple absorb at the analytical wavelength the equation becomes

$$\Delta A(t) = [2 \cdot \Delta \epsilon \cdot C^* \cdot D^{1/2} \cdot t^{1/2}] / \pi^{1/2} \quad (5)$$

where ΔA is the change in absorbance at the analytical wavelength, and $\Delta \epsilon$ is the associated change in molar absorptivity.

If a reflectance geometry (Figure 16) is utilized instead of a transmission geometry then the absorbance change at a given time will be larger than in the transmission case by a factor $2/\cos\theta$ as discussed above. Therefore, the pertinent equation is

$$\Delta A(t) = [4.\Delta\varepsilon.C^*.D^{1/2}.t^{1/2}] / [\cos\theta.\pi^{1/2}] \quad (6)$$

which shows that the absorbance change should be linear with $t^{1/2}$. If the concentration of the analyte solution as well as the diffusion coefficient of the reacting species is known then the change in molar absorptivity at the analytical wavelength associated with the oxidation process may be calculated.

In a similar fashion it can be shown that, for a reversible electrode reaction, the absorbance change on the reverse step of a double potential step experiment is given by

$$\Delta A(t > \tau) = [4.\Delta\varepsilon.C^*.D^{1/2}.(t^{1/2} - (t - \tau)^{1/2})] / [\cos\theta.\pi^{1/2}] \quad (7)$$

where τ is the time at which the potential is stepped back to its original value (14, 62).

4.3 Details of cell construction

The design of the chronoabsorptometric cell is shown in Figure 17. The cell body was constructed from a solid teflon block 90 mm X 50 mm X 50 mm. A cylindrical hole 11 mm in diameter was drilled through the centre of the block to accept the working and counter electrodes. Two holes were drilled into the top

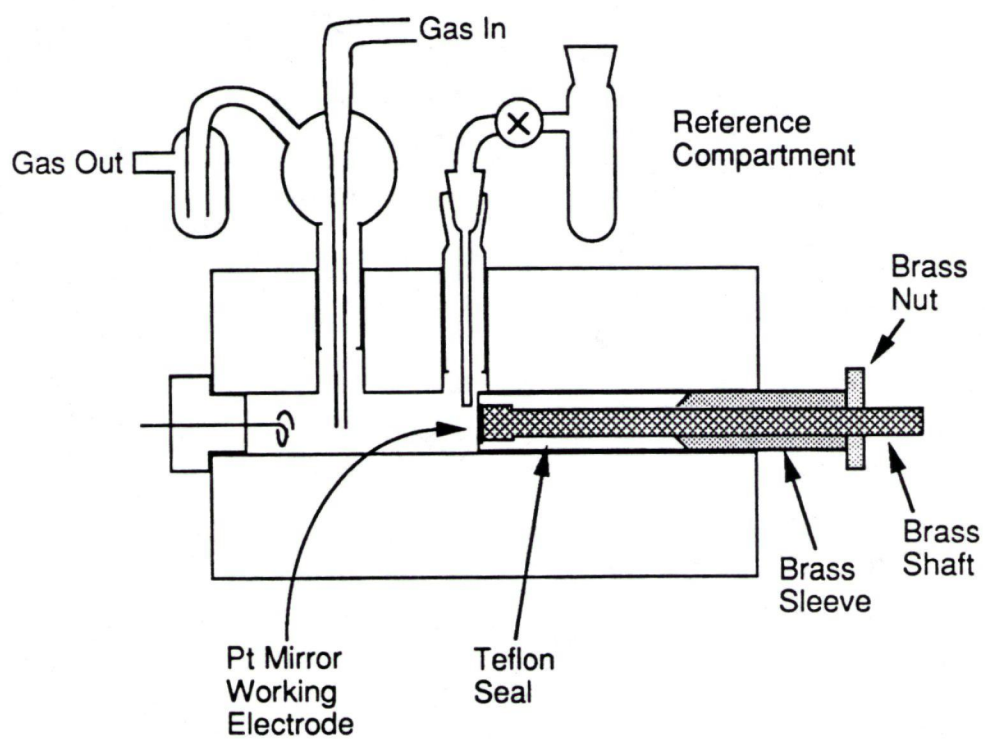
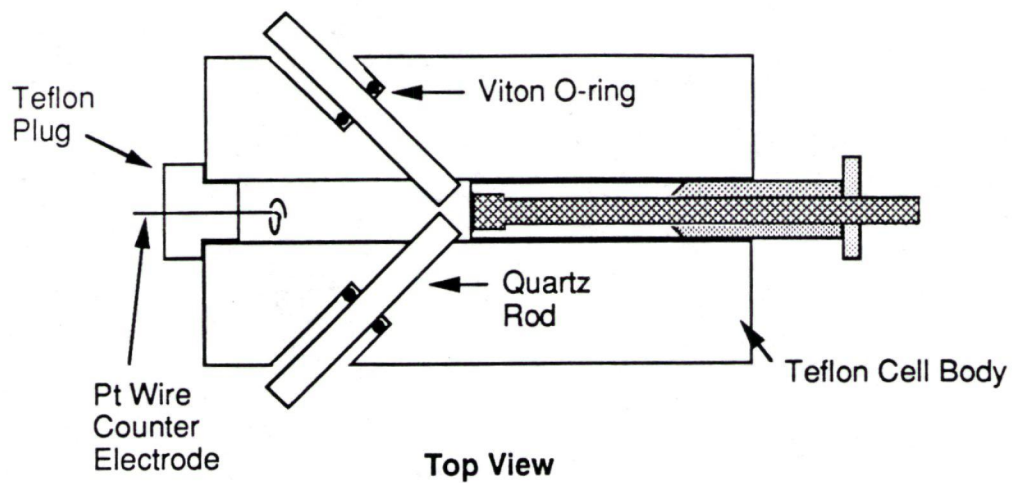


Figure 17 Design of the chronoabsorptometric cell.

of the block and a ground glass joint (5/30 standard taper) required to accept a luggin capillary from the reference electrode compartment, and an assembly to enable degassing were press-fitted into them. Two cylindrical holes of 5 mm diameter were drilled at an angle of 45° through the sides of the cell body into the main cylindrical channel to accept two polished quartz rods which act as windows in the u.v.-visible region of the electromagnetic spectrum. Viton O-rings were used to seal between the quartz rods and the teflon cell body. A press fit was not used in order that optical alignment of the rods would be possible. The working electrode was of the same design as that utilized previously for thin-layer spectroelectrochemistry. The details of its construction are given in ref. 17a. The counter electrode was constructed from a teflon plug which had a hole drilled through the centre into which a Pt-wire was press-fitted and coiled up.

4.4 Double-potential step chronoabsorptometry system: Design and operation

A schematic of the double potential step chronoabsorptometry system is shown in Figure 18. A 75 W xenon arc lamp is used as a light source. The radiation enters a GCA-McPherson model EU-701 spectrophotometer. The entrance and exit slit widths were chosen to be 2 mm. Monochromatic light from the monochromator exit slit passes through the quartz rod window of the

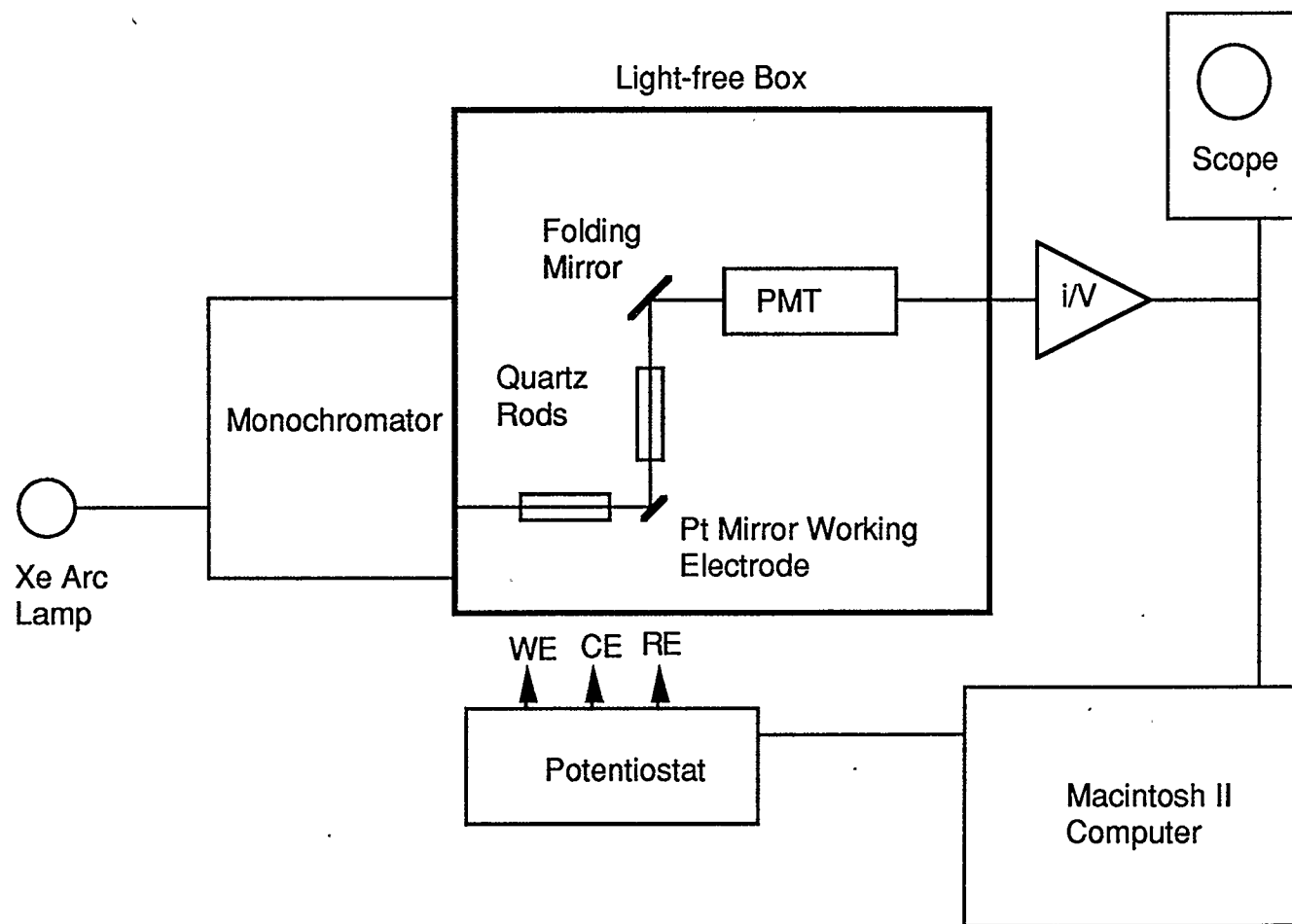


Figure 18 Schematic of the double potential step chronoabsorptometric experiment

chronoabsorptometric cell and is specularly reflected from the Pt mirror disk working electrode through the second quartz rod window. The angle of incidence is fixed at 45 °. Light emerging from the chronoabsorptometric cell is reflected from a folding mirror to a Hamamatsu R268 photomultiplier tube (PMT) detector. The anode current of the PMT is amplified with a Keithley model 427 current amplifier.

The output of the current amplifier is monitored with a Macintosh II computer fitted with a G. W. Instruments Macadios II analog-digital interface card. A Think Pascal control program which accessed the Macadios II input-output and data-manipulation libraries was written to allow the generation of successive double potential steps of variable potential and duration with simultaneous collection of up to a one thousand point array at a fixed rate of 5 ms per point with real-time signal averaging. The generated potential step was fed to the adder input of a Hi-Tek model DT2101 potentiostat which was used to control the working electrode potential with respect to the reference potential. The data arrays from the experiments could be saved as Microsoft Excel files which could then be further processed within a Microsoft Excel spreadsheet.

4.5 Results and discussion

Chloro(tetraphenylporphyrinato)iron(III), [Fe(tpp)]Cl, is reversibly

one-electron oxidized in dichloromethane containing 0.1 M Bu_4NClO_4 at 1.13 V vs. SCE. The oxidation product has been characterized and formulated as an iron(III) porphyrin π -cation radical (12). Double potential step chronoabsorptometry of 10^{-5} - 10^{-4} M $[\text{Fe}(\text{tpp})]\text{Cl}$ in dichloromethane containing 0.1 M Bu_4NClO_4 was carried out at single wavelengths separated by 20 nm intervals in the range 370-610 nm. The exact concentration was selected such that the analyte solution in the chronoabsorptometric cell gave an absorbance between 0.9-1.5 at the analytical wavelength. The potential perturbation consisted of a step from 0.90 V to 1.3 V vs. SCE. The potential was held at 1.3 V for one second before being stepped back to 0.90 V. A delay of 12 seconds was invoked between successive step experiments. The absorbance of the analyte solution was monitored from a time 200 ms prior to the forward potential step from 0.90 V to 1.30 V until a time 2 sec after the reverse potential step.

A representative absorbance-time (A-t) transient is shown in Figure 19.

According to theory (14, 62) the ratio of the absorbance at time 2τ relative to the absorbance at time τ for a one-electron redox process without complications should be 0.414. The experimental value is 0.433 ± 0.017 in excellent agreement with the theoretical value.

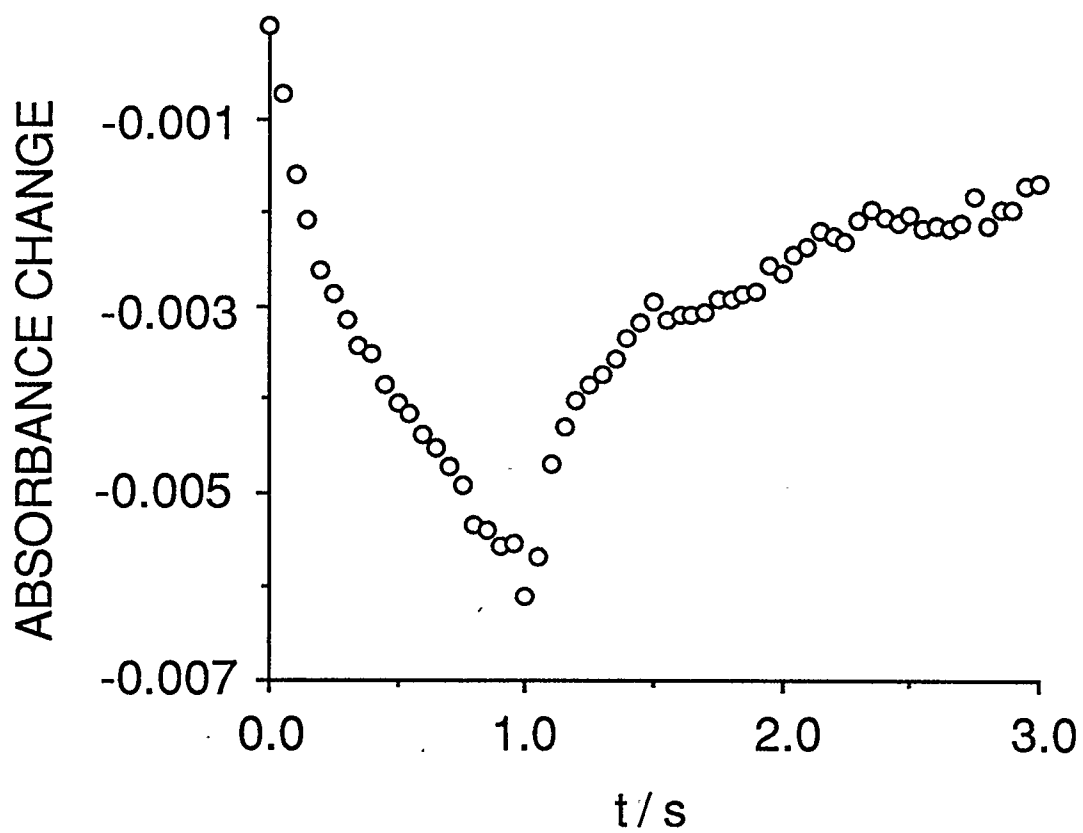


Figure 19 Absorbance-time transient for the double potential step chronoabsorptometry of [Fe(tpp)]Cl at 410 nm. Data is an average of 64 experiments and was smoothed using 10 point averaging.

The absorbance change ΔA on the forward step is related to the bulk porphyrin concentration C^* for a reversible one-electron process by equation 6.

Therefore, a plot of ΔA against $t^{1/2}$ should be linear with zero intercept and slope given by

$$[4.\Delta\epsilon.D^{1/2}.C^*] / [\cos\theta.\pi^{1/2}] \quad (8)$$

Since θ is fixed at 45° , C^* is known from spectrophotometry of the analyte solutions, and the diffusion coefficient D was measured by chronoamperometry to be $1.183 \times 10^{-5} \text{ cm}^2 \text{ s}^{-1}$, the change in molar absorptivity, $\Delta\epsilon$ may be extracted from the slope.

An $A-t^{1/2}$ plot for the forward step of the data shown in Figure 19 is presented in Figure 20. The linear region of the data extends from times of *ca.* 100 ms and longer. At shorter times the absorbance change was less than that expected from theory presumably due to the RC time constant associated with the system. It is probable that the important factor in setting this time constant is the double-layer capacitance and associated uncompensated solution resistance in the electrochemical cell (43, 44, 58). Thus, the experimental system is limited by the electrochemical response of the spectroelectrochemical cell. This value compares favourably with that observed by other workers using

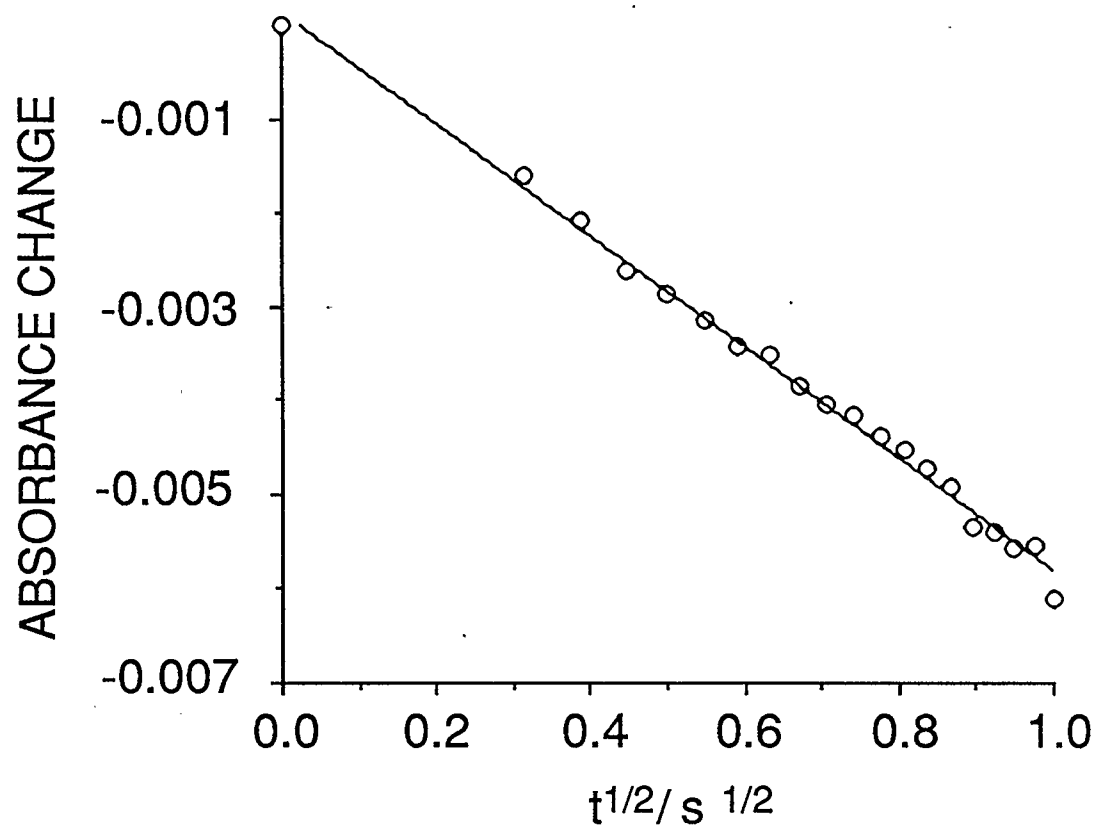


Figure 20 Plot of absorbance against square root of elapsed time for the forward step of the data presented in Figure 19.

aqueous solvent-supporting electrolyte systems (58). In principle, this time can be shortened by applying a larger potential step. In the present case, this is precluded by a second oxidation of the $[\text{Fe}(\text{tpp})]\text{Cl}$ at 1.42 V.

The u.v.-visible spectrum of $[\text{Fe}(\text{tpp})]\text{Cl}$ is shown in Figure 21 together with the spectrum of the corresponding iron(III) porphyrin π -cation radical reconstructed from the $\Delta\epsilon$ values obtained from the single-wavelength chronoabsorptometry experiments and the measured molar absorptivity, ϵ values of the unoxidized porphyrin. The uncertainty associated with each experimental point was assessed by calculating the standard deviation of the $A\text{-}t^{1/2}$ plot for each experiment. The relative percent errors in the calculated molar absorptivities were all less than 4%.

Figure 22 shows the time-resolved u.v.-visible spectral changes associated with electrolysis at 1.3 V of a thin-layer of 1 mM $[\text{Fe}(\text{tpp})]\text{Cl}$ in dichloromethane containing 0.1 M Bu_4NClO_4 . It is seen that the oxidation proceeds with isosbestic points to produce a final spectrum of the iron(III) porphyrin π -cation radical. Comparison between the final spectrum in Figure 22 with the reconstructed spectrum of the iron(III) porphyrin π -cation radical shown in Figure 21 shows excellent agreement between the spectra obtained by the two

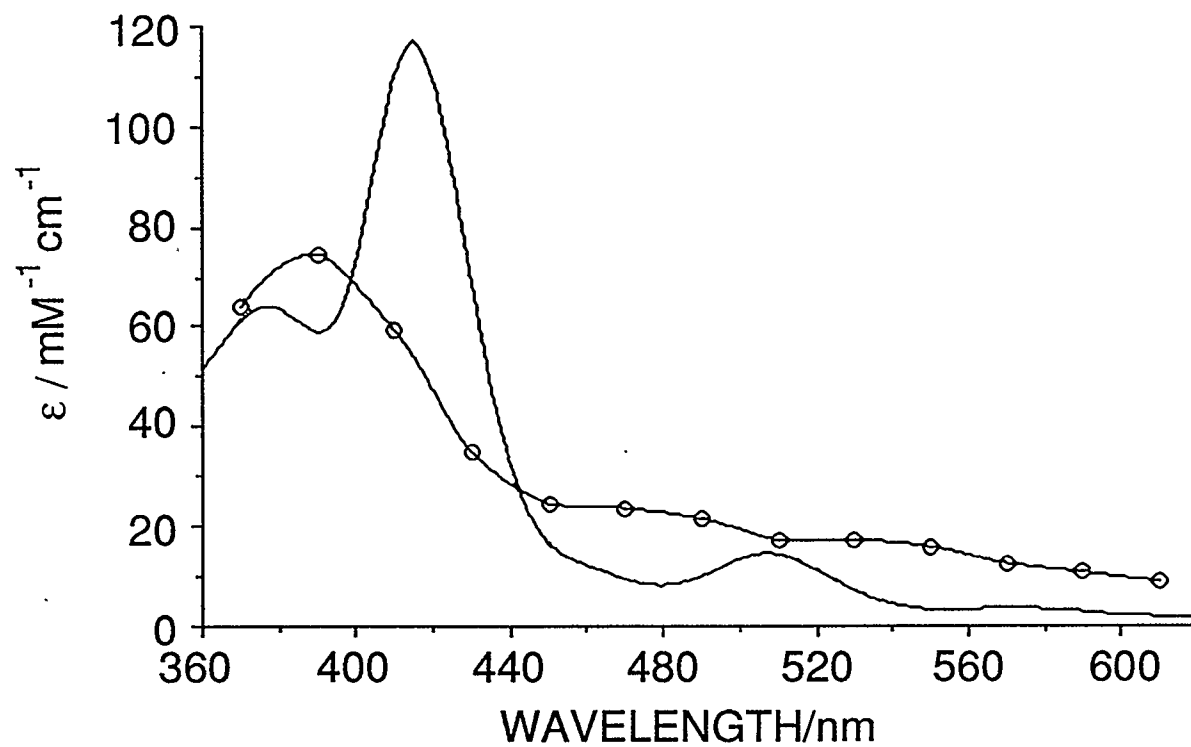


Figure 21 U.v.-visible spectrum of $[\text{Fe}(\text{tpp})]\text{Cl}$ (solid line) together with the u.v.-visible spectrum of the corresponding iron(III) porphyrin π -cation radical (circles) calculated from chronoabsorptometric data.

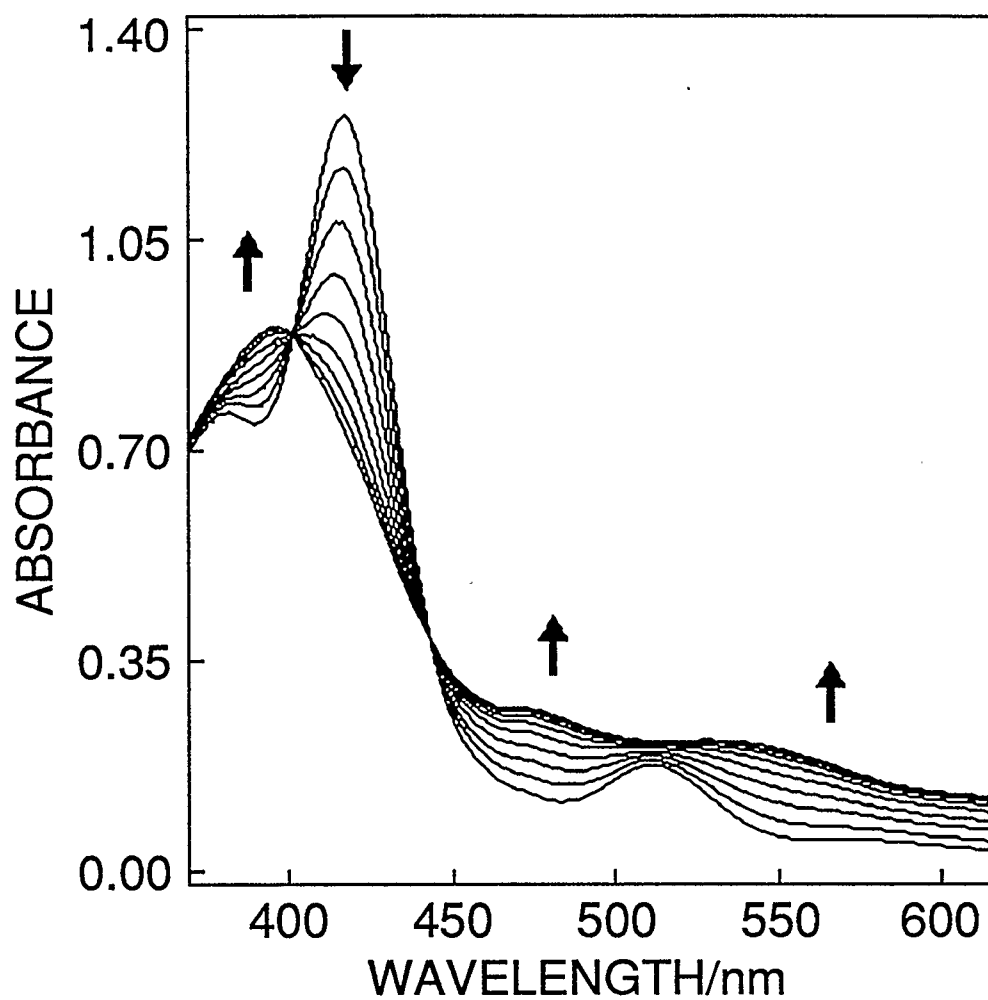


Figure 22 U.v.-visible spectral changes associated with the one-electron oxidation of $[\text{Fe}(\text{tpb})]\text{Cl}$ measured using time-resolved thin-layer reflectance spectroelectrochemistry.

different techniques.

4.6 Conclusion

It is clear that the described chronoabsorptometry experiment is capable of producing accurate values for changes in molar absorptivity using experiments on the 1 second timescale. It is possible to use iron porphyrin concentrations of 0.1 mM or greater even throughout the Soret region where the analyte gives rise to intense absorbance features.

To the author's knowledge this is the first time the chronoabsorptometry technique has been applied to systems in which the analyte solutions significantly absorb at the analytical wavelength. The use of chronoabsorptometry under conditions of semi-infinite linear diffusion in order to quantitatively assess *changes* to the molar absorptivity associated with an electrode reaction is also novel. This system is therefore expected to be useful in characterizing the u.v.-visible spectra of electrogenerated iron porphyrin intermediates which are stable on a timescale of *ca.* 1 second.

CHAPTER FIVE

***IN SITU* INFRARED SPECTROELECTROCHEMICAL STUDIES OF TETRAPHENYLPORPHYRIN COMPLEXES CONTAINING MANGANESE, IRON, AND COBALT**

5.1 Introduction

Metalloporphyrins can undergo reversible redox reactions in which the site of electron transfer may be localized at either the porphyrin ring or the central metal. Both reaction types are important in natural processes such as photosynthesis, or the action of heme enzymes such as cytochrome P-450. For this reason, the differentiation between metal-centred and porphyrin ring-centred redox reactions of metalloporphyrins is a topic which has merited considerable attention.

On one-electron oxidation a metalloporphyrin may form either a π -cation radical, or a complex in a higher metal oxidation state. In this regard, a number of diagnostic criteria have been developed to allow the correct formulation of the oxidized product based on optical spectra, EPR, electrochemistry, magnetic moment, or magnetic circular dichroism measurements (15, 16). More recently, criteria based on solid state infrared spectra of the isolated products (11), and

resonance Raman spectra obtained in solution following bulk electrolysis (19), have been suggested.

Dr. A. S. Hinman's research group had previously applied the technique of *in situ* Fourier transform infrared thin-layer reflectance spectroelectrochemistry to a study of this question (17). In this method, a thin layer (10 to 100 μm) of electrolyte solution is confined between the surface of a polished electrode (Pt in these studies) and an infrared transparent window. Infrared radiation is directed through the thin layer onto the electrode. Analysis of the energy of the specularly reflected radiation prior to and following electrolysis of the thin layer solution affords the difference in absorbance resulting from the electrolysis reaction.

Previous studies involved the oxidation of a series of metal complexes of tetraphenylporphyrin which were all known to yield π -cation radicals upon one-electron oxidation (17b). This work confirmed the presence of a new strong infrared absorption near 1280 cm^{-1} , which had previously been observed in the solid state spectra of isolated cation radicals (11) and suggested to be diagnostic of one-electron oxidation of the tetraphenylporphyrin ring. In addition, the *in situ* difference spectra revealed that a similar series of absorbance increases and decreases accompanied formation of each of the

π -cation radicals investigated. However, since it is well known that a number of porphyrin ligand vibrations are sensitive to the oxidation state, as well as the spin state of the central metal atom (63), it was not clear to what extent these additional features of the difference spectra might be specifically characteristic of oxidation of the porphyrin ring, as opposed to metal oxidation.

This chapter consists of a report on the *in situ* FTIR reflectance spectroelectrochemistry of tetraphenylporphyrinatocobalt(II), $[\text{Co}^{\text{II}}(\text{tpp})]$, chloro(tetraphenylporphyrinato)iron(III), $[\text{Fe}^{\text{III}}(\text{tpp})]\text{Cl}$, and perchlorato(tetraphenylporphyrinato)manganese(III), $[\text{Mn}^{\text{III}}(\text{tpp})]\text{ClO}_4$. $[\text{Co}^{\text{II}}(\text{tpp})]$ can be oxidized in two successive one-electron transfer steps yielding first the metal(III) complex, and then the metal(III) π -cation radical complex. $[\text{Fe}^{\text{III}}(\text{tpp})]\text{Cl}$ and $[\text{Mn}^{\text{III}}(\text{tpp})]\text{ClO}_4$ can be reduced to the corresponding metal(II) species or oxidized to metal(III) π -cation radical complexes in independent one-electron transfer steps. These compounds thus afford the opportunity for direct comparison of the changes to the vibrational spectrum associated with the metal(II)-metal(III) redox couple with those accompanying oxidation of the porphyrin ring.

5.2 Results and discussion

5.2.1 Electrochemistry and u.v.-visible spectroelectrochemistry

In order to ascertain that the electrode reactions could be carried out cleanly and reversibly on the time scale required for *in situ* FTIR spectroelectrochemical characterization, the reactions were first investigated by cyclic voltammetry, thin layer cyclic voltammetry, and thin-layer u.v.-visible spectroelectrochemistry. Initial studies were carried out in CH₂Br₂ containing 0.1 M Bu₄NPF₆, since CH₂Br₂ has been shown in previous studies to be useful for FTIR characterization of metalloporphyrin electrode reactions (17a). In this solvent, the oxidation of [Co^{II}(tpp)] to [Co^{III}(tpp)]⁺, and subsequent oxidation to the porphyrin π -cation radical, [Co^{III}(tpp)•]²⁺, could both be carried out cleanly and reversibly. Similarly, the oxidations of [Fe^{III}(tpp)]Cl and [Mn^{III}(tpp)]ClO₄ to the corresponding π -cation radicals occurred reversibly. The reductions of [Fe^{III}(tpp)]Cl and [Mn^{III}(tpp)]ClO₄ to the corresponding metal(II) species, however, were accompanied by an irreversible following reaction, as evidenced by reverse to forward peak current ratios of less than unity in conventional and thin layer cyclic voltammetry experiments, and the absence of isosbestic points in the time-resolved thin-layer u.v.-visible spectroelectrochemistry. Both Fe(II) and Mn(II) porphyrins are known to be highly unstable in the presence of dioxygen, so that reaction with trace O₂ is a

likely explanation for the observed instability of these metal(II) complexes.

It was observed that the required stability of the Fe(II) and Mn(II) species could readily be attained in 1:1 mixtures of CH₂Br₂ : CH₃CN, which may be due to a competitive inhibition of O₂ binding by CH₃CN. Acetonitrile alone could also be used to study the manganese complex, but was not useful for the iron or cobalt complexes because of their limited solubility.

For the oxidation of [Mn^{III}(tpp)]ClO₄, [Fe^{III}(tpp)]Cl, and [Co^{III}(tpp)]⁺ to the corresponding π -cation radicals, and the metal-centred oxidation of [Co^{II}(tpp)] to [Co^{III}(tpp)]⁺ it was possible to use both 1:1 CH₂Br₂ : CH₃CN and dibromomethane alone as solvent for the infrared spectroelectrochemical experiments. The infrared difference spectra obtained in these two solvent systems were nearly identical.

Table 2 presents the reversible half-wave potentials for the various redox couples observed in 1:1 CH₂Br₂ : CH₃CN containing 0.1 M Bu₄NPF₆, as measured by cyclic voltammetry. Figure 23 illustrates the u.v.-visible spectral changes associated with the redox processes identified in Table 2. In all cases, clear isosbestic points are observed, indicating that the electrode reactions

Table 2 Half-wave potentials for the the first metal- and ligand-centred redox reactions of the 0.5 mM porphyrin complexes in 1:1 CH₂Br₂ : CH₃CN containing 0.1 M Bu₄NPF₆.

Compound	E _{1/2} V v. SCE	
	M ^{III} / M ^{II}	(tpp) ¹⁻ / (tpp) ²⁻
[Mn ^{III} (tpp)]ClO ₄	-0.23	1.23
[Fe ^{III} (tpp)]Cl	-0.30	1.09
[Co ^{II} (tpp)]	0.33	1.06

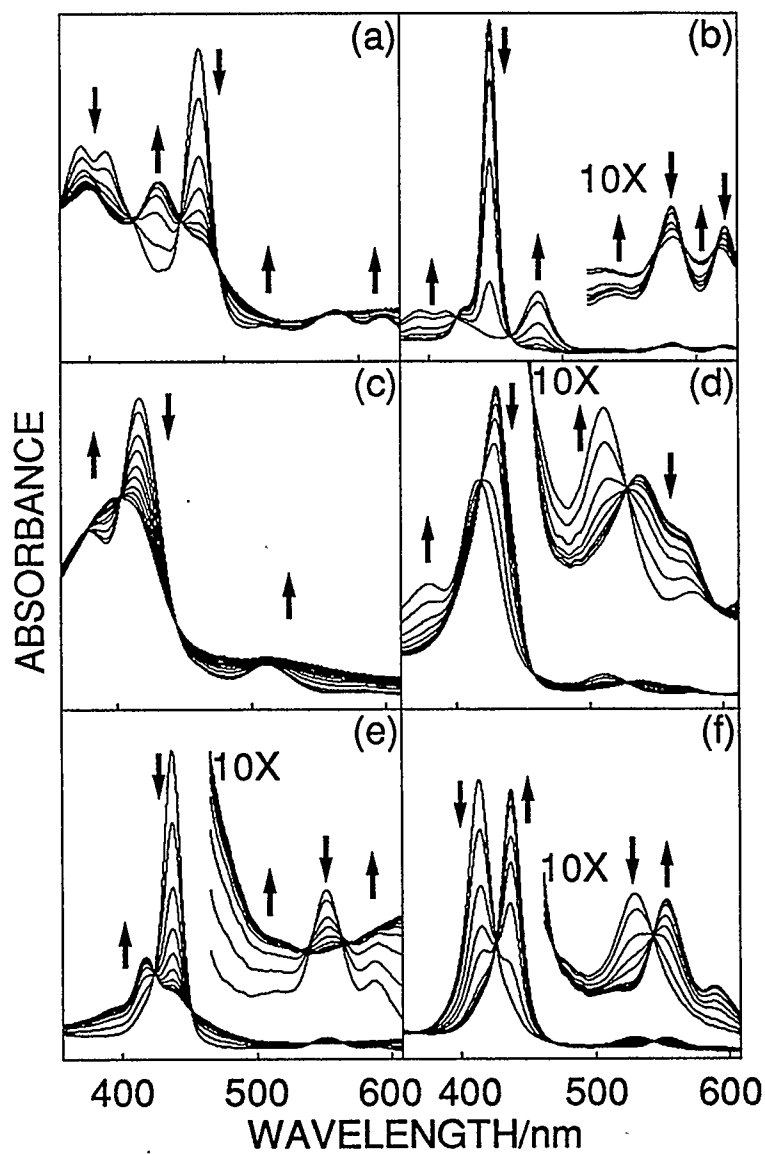


Figure 23 Time resolved thin-layer u.v.-visible spectroelectrochemistry of the one-electron oxidation of (a) $[\text{Mn}^{\text{III}}(\text{tpp})]\text{ClO}_4$ (b) $[\text{Mn}^{\text{II}}(\text{tpp})]$ (c) $[\text{Fe}^{\text{III}}(\text{tpp})]\text{Cl}$ (d) $[\text{Fe}^{\text{II}}(\text{tpp})]$ (e) $[\text{Co}^{\text{III}}(\text{tpp})]\text{PF}_6$ and (f) $[\text{Co}^{\text{II}}(\text{tpp})]$ in 1:1 $\text{CH}_2\text{Br}_2 : \text{CH}_3\text{CN}$ containing 0.1 M Bu_4NPF_6 .

proceed in a quantitative fashion. The spectral changes are consistent with literature data for the indicated processes, confirming the electron transfer sites as indicated (1b, 55).

5.2.2 In situ FTIR spectroelectrochemistry

The mid-infrared difference spectra observed upon metal- and ligand-centred oxidation of the 2 mM porphyrin complexes in 1:1 CH₂Br₂ : CH₃CN containing 0.1 M Bu₄NPF₆ are shown in Figures 24-26. The mid-infrared difference spectra observed upon metal- and ligand-centred oxidation of [Mn^{III}(tpp)]ClO₄ in CH₃CN containing 0.1 M Bu₄NPF₆ are shown in Figure 27. The positive absorbance (appearance) features indicate an increased absorption in the oxidized complex relative to the unoxidized system, whereas negative absorbance (disappearance) features indicate a corresponding decrease in absorption. The relatively high absorption due to the solvent mixture, as well as the tetra-n-butylammonium cation, acted to lower the signal-to-noise ratio in several regions of the spectra. Most notably, an intense band at 1192 cm⁻¹ due to CH₂Br₂ absorbed practically all of the infrared beam energy near 1200 cm⁻¹. In some cases, the signal-to-noise ratio was lowered near 1450 cm⁻¹ due to CH₃CN and tetra-n-butylammonium cation absorbances.

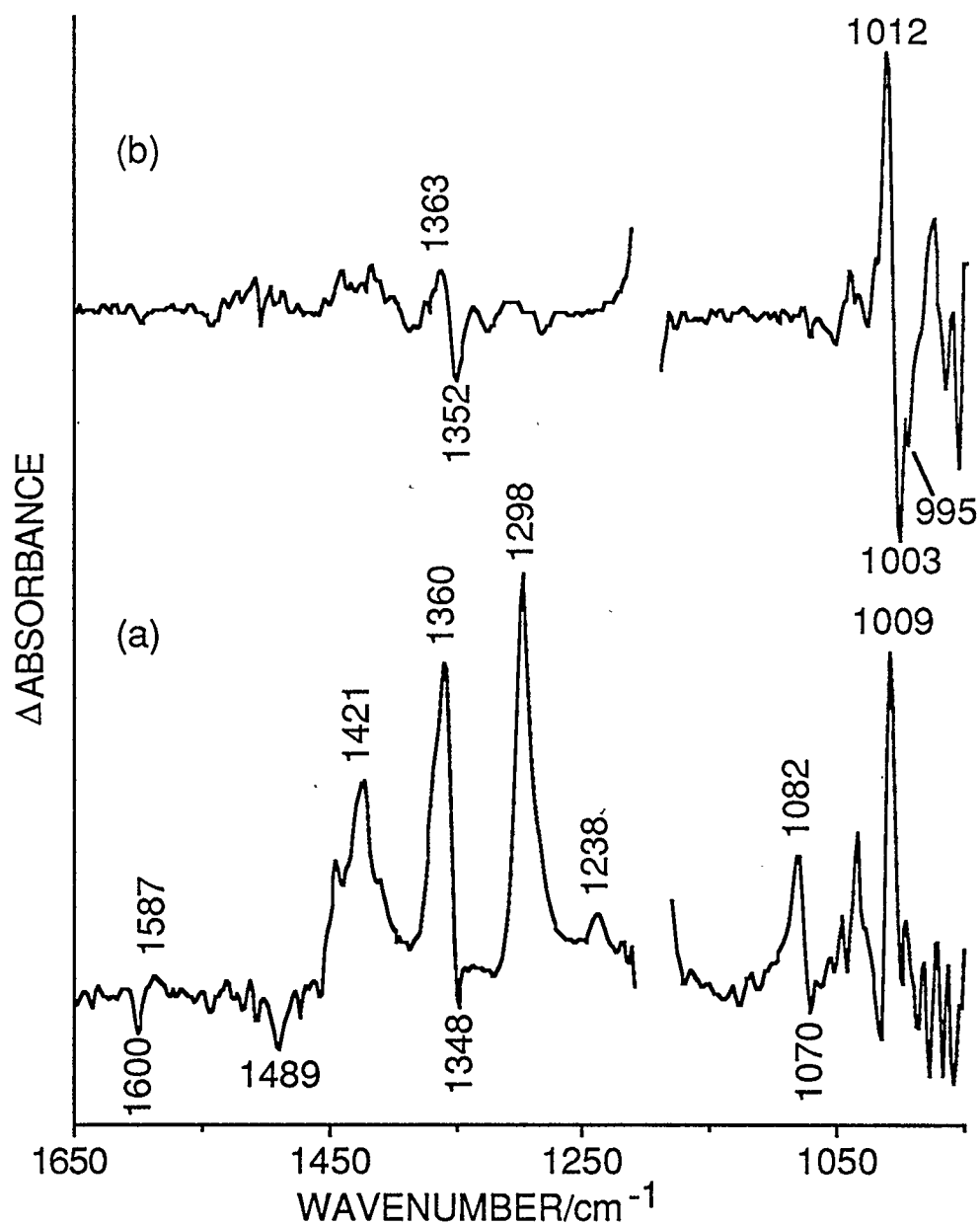


Figure 24 *In situ* FTIR difference spectra observed for the one-electron oxidation of (a) $[\text{Co}^{\text{III}}(\text{tpp})]\text{PF}_6$ and (b) $[\text{Co}^{\text{II}}(\text{tpp})]$ in 1:1 $\text{CH}_2\text{Br}_2 : \text{CH}_3\text{CN}$ containing 0.1 M Bu_4NPF_6 .

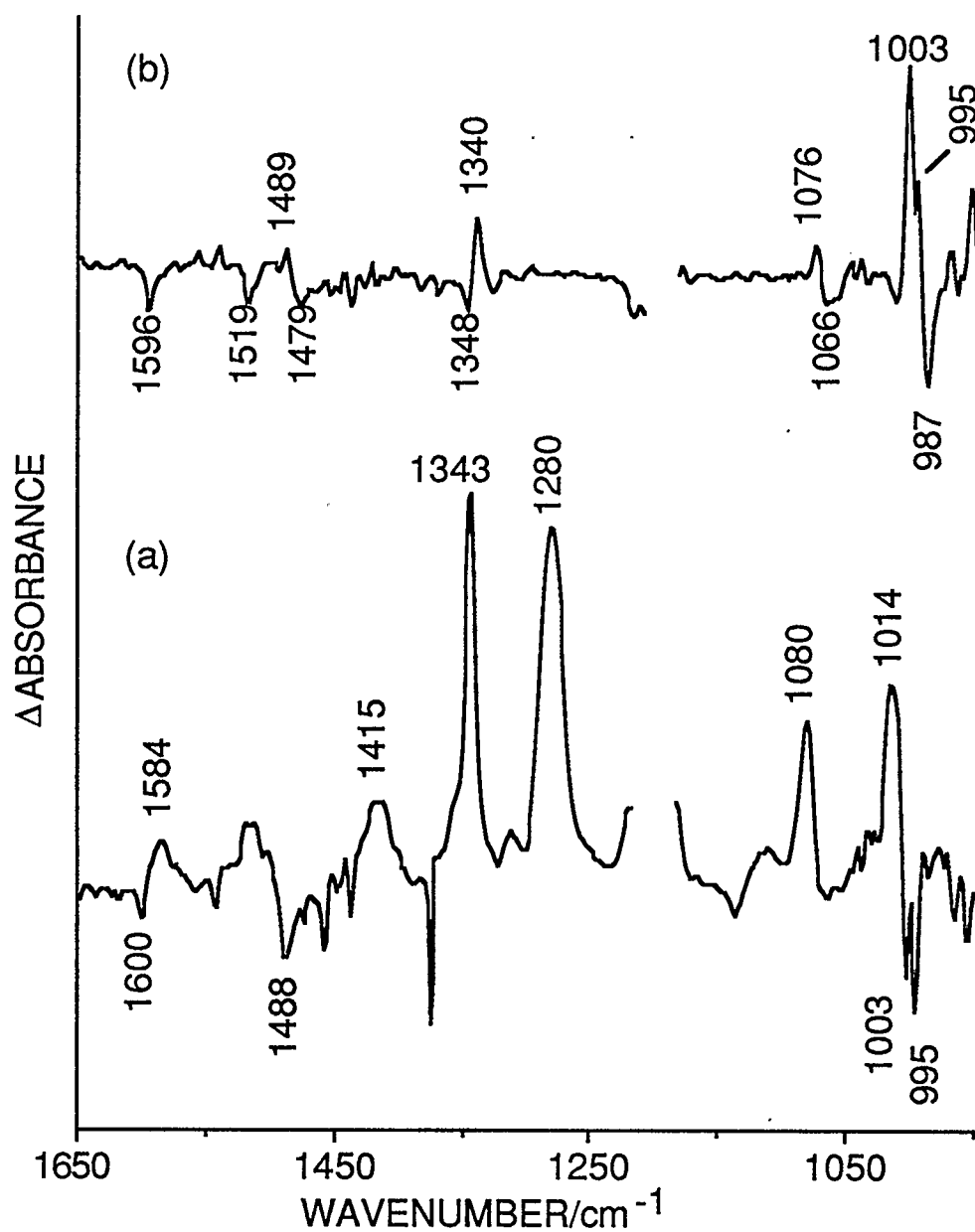


Figure 25 *In situ* FTIR difference spectra observed for the one-electron oxidation of (a) $[\text{Fe}^{\text{III}}(\text{tp})]\text{Cl}$ and (b) $[\text{Fe}^{\text{II}}(\text{tp})]$ in 1:1 CH_2Br_2 : CH_3CN containing 0.1 M Bu_4NPF_6 .

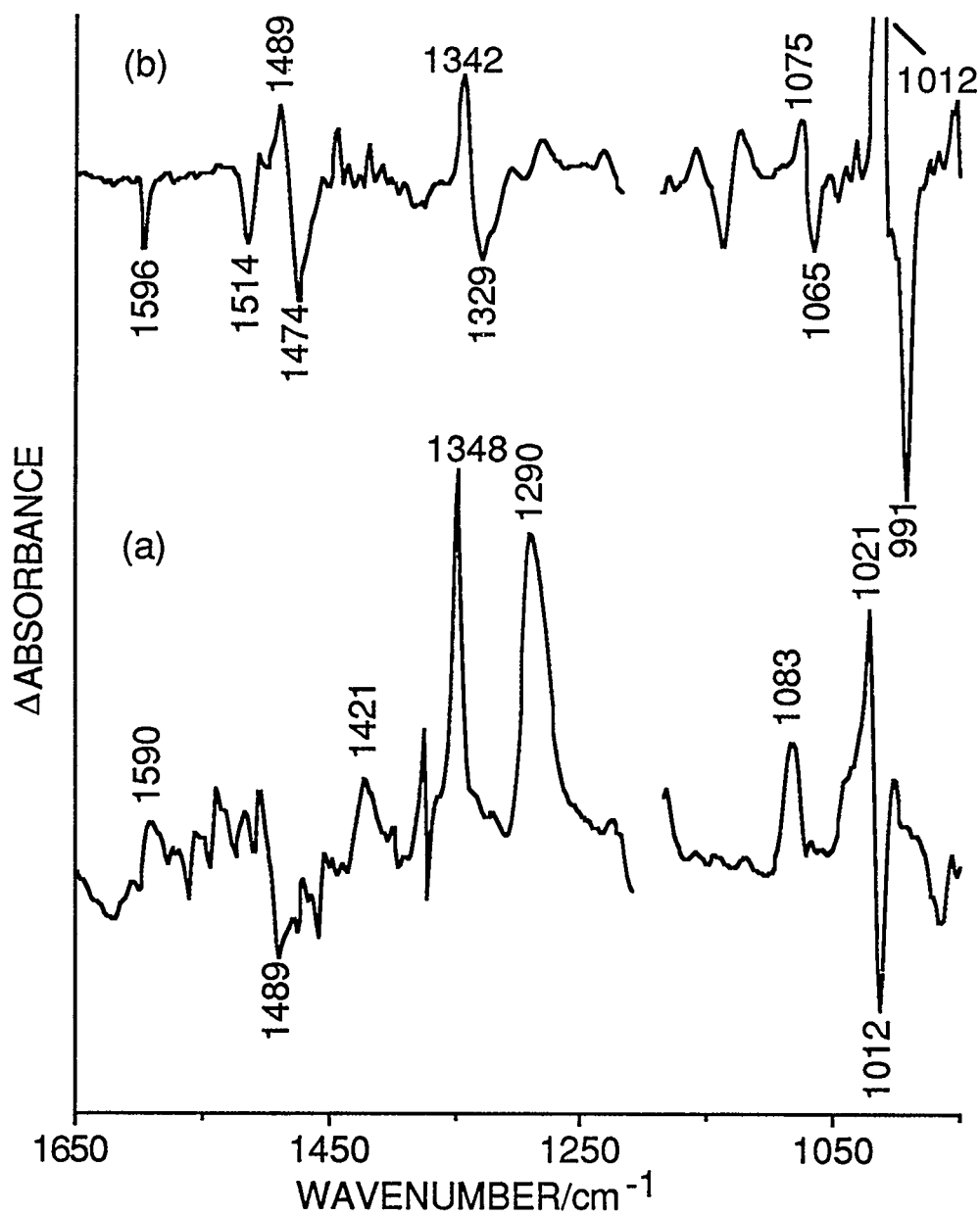


Figure 26 *In situ* FTIR difference spectra observed for the one-electron oxidation of (a) $[\text{Mn}^{\text{III}}(\text{tpp})]\text{ClO}_4$ and (b) $[\text{Mn}^{\text{II}}(\text{tpp})]$ in 1:1 CH_2Br_2 : CH_3CN containing 0.1 M Bu_4NPF_6 .

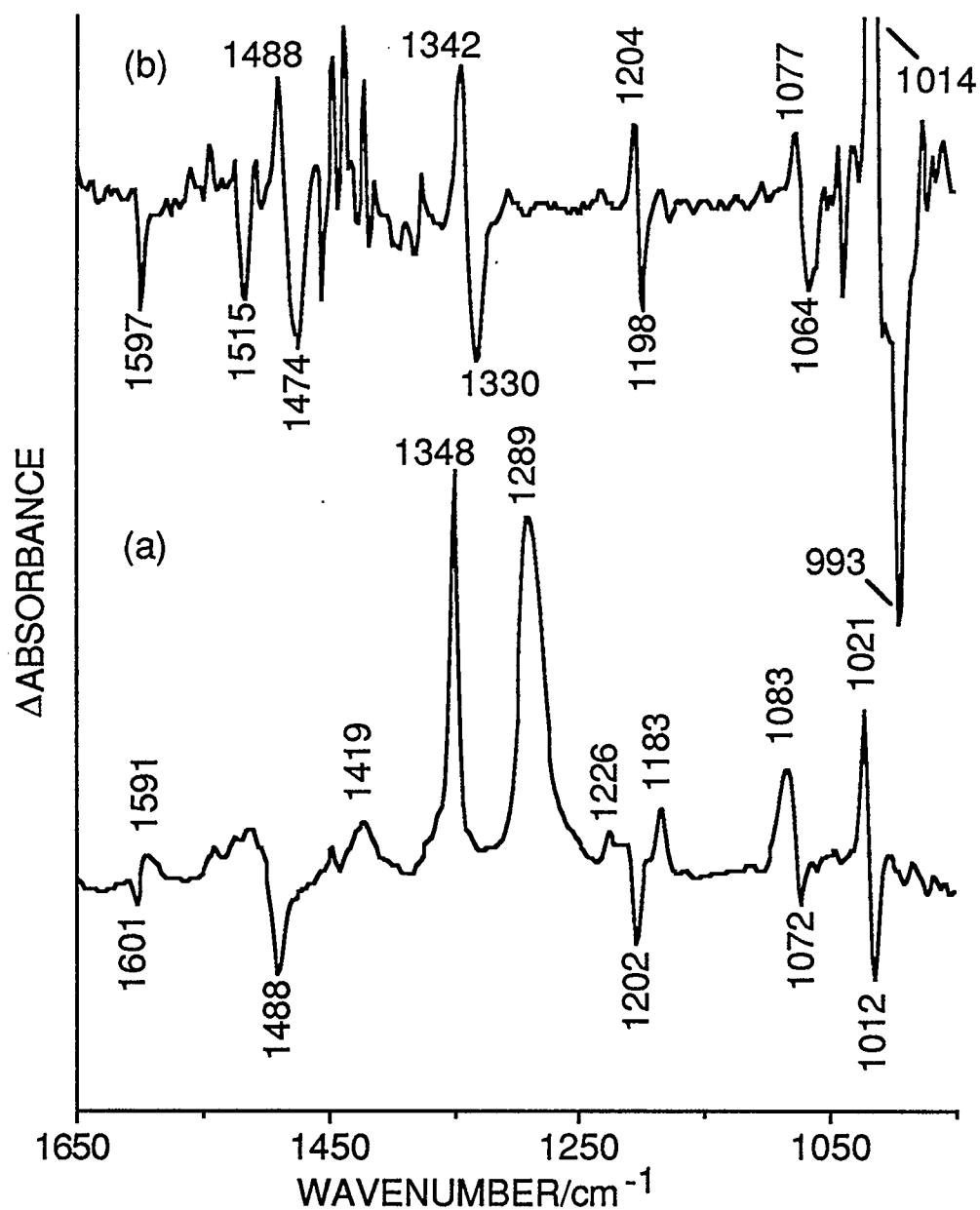


Figure 27 *In situ* FTIR difference spectra observed for the one-electron oxidation of (a) $[\text{Mn}^{\text{III}}(\text{tpp})]\text{ClO}_4$ and (b) $[\text{Mn}^{\text{II}}(\text{tpp})]$ in CH_3CN containing 0.1 M Bu_4NPF_6 .

The mid-infrared spectral changes associated with the metal-centred and ligand-centred oxidation of $[\text{Co}^{\text{II}}(\text{tpp})]$ in dibromomethane containing 0.1 M Bu_4NClO_4 have been previously reported (17b). However, coordination changes involving the perchlorate anion became manifest in the mid-infrared spectra because the anion absorbs near 1100 cm^{-1} in the infrared. Consequently, any changes to the porphyrin vibrations in the region around 1100 cm^{-1} were not observable. In the present study the use of the hexafluorophosphate anion, which has no strong bands in the mid-infrared, avoided such effects.

The mid-infrared difference spectra associated with the ligand-centred oxidation of the porphyrin complexes are shown in Figures 23 (a), 24 (a), 25 (a), and 26 (a). The general pattern of appearance and disappearance features is seen to be very similar for all three complexes. In fact, this pattern has been observed with all the tpp π -cation radicals studied to date, including that of the free base (17b).

The strong and medium intensity mid-infrared bands produced by the Mn(III), Fe(III), and Co(II) porphyrin complexes are listed in Table 3, together with a tentative assignment. In this region of the spectrum, the observed bands are due to in-plane vibrations of the porphyrin ring, as well as modes arising from

Table 3 Mid-infrared bands due to the porphyrin complexes.^a

Assignment ^b	[Mn ^{III} (tpp)]ClO ₄ ^c	[Fe ^{III} (tpp)]Cl	[Co ^{III} (tpp)] ⁺
ϕ_4'' , ν (phenyl)	1597 (1599)	1597 (1599)	1599 (1599)
ν_{39} , ν (C $_{\alpha}$ C $_m$) _{sym}	1487 (1489)	1485 (1487)	1491 (1492)
ν_{40} , ν (Pyr 1/4-ring)	1441 (1441)	1440 (1442)	1440 (1442)
ν_{41} , ν (Pyr 1/2-ring) _{sym}	1341 (1343)	1339/4 (1339)	1350 (1350)
ν_{52} , δ (C $_{\beta}$ H) _{sym}	1204	1200	1206
ϕ_6'' , ν (phenyl)	1179	1175	1177
ν_{51} , δ (C $_{\beta}$ H) _{asym}	1073 (1076)	1070 (1073)	1072 (1071)
ν_{44} , ν (Pyr 1/2-ring) _{asym}	1013 (1011)	1003 (1003)	1005 (1005)
ν_{44} , ν (Pyr 1/2-ring) _{asym}		995 (995)	997 (997)

^a Samples in form of KBr pellet. Numbers in parentheses refer to solution state spectra measured in 1: 1 CH₂Br₂ : CH₃CN in a 0.1 mm pathlength cell.

^b Taken from ref. 64. ^c ν (ClO₄) bands appear at 1122 and 1099 cm⁻¹.

the four phenyl substituents (64). If the effective molecular symmetry is D_{4h} , then the allowed infrared transitions in this region will have E_u symmetry. On one-electron oxidation of the porphyrin ligand, it is observed that a number of these modes undergo characteristic shifts in wavenumber (see Table 4). In most cases, the magnitude of these shifts could be estimated from the separation between appearance and disappearance features in a bipolar difference band. In cases where intensity changes had masked the disappearance feature, the shift was estimated from the difference in wavenumber between the appearance feature in the difference spectrum, and the parent band in the solution state spectrum of the unoxidized complex (Table 3). Thus, the phenyl mode, ϕ_4'' , shifted down by *ca.* $10\text{-}16\text{ cm}^{-1}$. In contrast, there was a shift to higher wavenumber of the porphyrin ring modes ν_{41} (*ca.* $4\text{-}12\text{ cm}^{-1}$), ν_{51} (*ca.* $7\text{-}12\text{ cm}^{-1}$), and ν_{44} (*ca.* $9\text{-}19\text{ cm}^{-1}$). The ν_{39} mode was seen to lose intensity, but apparently did not undergo any significant shift in wavenumber. The possibility that ν_{39} shifts to lower wavenumber producing the appearance feature near 1420 cm^{-1} may be ruled out since both bands can be seen in the solid state spectrum of the isolated π -cation radical derived from $[\text{Fe}^{\text{III}}(\text{tpp})]\text{Cl}$ (12). The ν_{41} mode underwent no apparent change in either

Table 4 Position of new bands and wavenumber shifts to existing bands observed during ligand-centred oxidation of the porphyrin complexes in 1:1 CH₂Br₂ : CH₃CN containing 0.1 M Bu₄NPF₆.

Assignment ^a	[Mn ^{III} (tpp)]ClO ₄	[Fe ^{III} (tpp)]Cl	[Co ^{III} (tpp)] ⁺
φ ₄ ", v(phenyl)	-10	-16	-13
ν ₄₁ , v(Pyr 1/2-ring) _{sym}	+5	+4	+12
ν ₅₁ , δ(C _β H) _{asym}	+7	+7	+12
ν ₄₄ , v(Pyr 1/2-ring) _{asym}	+9	+11	
ν ₄₄ , v(Pyr 1/2-ring) _{asym}	+19		
new bands:	1421	1415	1421
	1290	1280	1298
			1238

^a Taken from ref. 64.

wavenumber or intensity on ligand-centred oxidation.

The manganese complex could also be studied using acetonitrile as solvent (Figure 26 (a)) which avoided loss of information from the region near 1200 cm^{-1} . In this case, it was observed that ν_{52} lost intensity and ϕ_6'' gained intensity, although neither underwent any appreciable shift in wavenumber. Again, this interpretation is borne out by comparison with the solid-state infrared spectrum of an isolated tpp π -cation radical (12).

It is believed that the ligand-centred oxidation of tpp metal complexes involves removal of an electron from an a_{2u} molecular orbital to produce a π -cation radical with an A_{2u} ground state (65). The a_{2u} orbital is predicted to have antibonding character between the N and C_α atoms, as well as the C_α and C_β atoms (66). Since calculations (64, 67), as well as spectroscopic measurements (68), suggest that the porphyrin ring modes ν_{41} and ν_{44} contain significant $\nu(C_\alpha N)$ and $\nu(C_\alpha C_\beta)$ character, the shift to higher wavenumber of these modes can be understood in terms of the increased bond strength between these centres, resulting from the removal of an electron from the a_{2u}

orbital. The relatively large shift of the ν_{51} mode is less easily explained, since this mode is considered to arise from a $\delta(\text{C}_\beta\text{H})$ asymmetric stretch (64).

In addition to characterizing the perturbation to bands present in the unoxidized porphyrins, the difference spectra indicate the appearance of new bands near 1420 and 1290 cm^{-1} upon ligand-centred oxidation. Additionally, a band near 1230 cm^{-1} can be seen in the difference spectrum of the Co complex, and the Mn complex when studied in acetonitrile. One reason for the presence of extra bands in the π -cation radical spectra might be a distortion of the porphyrin ring resulting in a lowering of the effective molecular symmetry. It is known that the solid state geometry of porphyrin π -cation radicals often shows a 'saddle' distortion which lowers the molecular symmetry from D_{4h} to D_{2d} (9). Such a distortion might allow the in-plane B_{2g} modes to become infrared active.

The ν_{29} , ν_{27} , and ν_{34} vibrational modes, which have B_{2g} symmetry, have been calculated to absorb in this wavenumber region (64). Furthermore, the saddle distortion permits a decrease in the dihedral angle between the phenyl substituents and the plane of the porphyrin ring (9). This effect might explain the observed perturbation of the phenyl modes ϕ_4'' and ϕ_6'' . However, if tpp π -radical cations do adopt a saddle conformation in the solution state, the

reason for this remains unclear. Although an argument based on considerations of electronic structure has been advanced (19), steric factors (69), as well as solid-state effects (9), are also considered to be important in determining the conformation of the porphyrin ring in metalloporphyrin complexes.

The mid-infrared difference spectra associated with the metal-centred oxidation of the porphyrin complexes are shown in Figures 23 (b), 24 (b), 25 (b), and 26 (b). Since both metal- and ligand-centred redox reactions were performed using the same thin solution layer without any adjustment to the pathlength, it is possible to directly compare the difference spectra obtained for both reaction types. In general, the pattern of absorbance changes was distinct from those produced on ligand-centred oxidation. The difference spectra contained mainly bipolar features resulting from perturbations to existing vibrational modes (see Table 5). Thus, the oxidation of [Co^{II}(tpp)] to the Co(III) species resulted in shifts to higher wavenumber of the vibrational modes ν_{41} (*ca.* 11 cm⁻¹) and ν_{44} (*ca.* 9-17 cm⁻¹). Metal-centred oxidation of the Fe(II) porphyrin produced considerably greater perturbation to the mid-infrared bands. In this case, there was a shift to lower wavenumber of ν_{41} (*ca.* 8 cm⁻¹).

Table 5 Position of bands which disappear and wavenumber shifts to existing bands during metal-centred oxidation of the 2 mM porphyrin complexes in 1:1 CH₂Br₂ : CH₃CN containing 0.1 M Bu₄NPF₆.

Assignment ^a	[Mn ^{III} (tpp)]ClO ₄	[Fe ^{III} (tpp)]Cl	[Co ^{II} (tpp)]
ν_{39} , $\nu(\text{C}_\alpha\text{C}_m)_{\text{sym}}$	+15	+10	
ν_{41} , $\nu(\text{Pyr } 1/2\text{-ring})_{\text{sym}}$	+13	-8	+11
ν_{51} , $\delta(\text{C}_\beta\text{H})_{\text{asym}}$	+10	+10	
ν_{44} , $\nu(\text{Pyr } 1/2\text{-ring})_{\text{asym}}$	+21	+8	+9
ν_{44} , $\nu(\text{Pyr } 1/2\text{-ring})_{\text{asym}}$		+16	+17
lost bands:	1514	1519	

^a Taken from ref. 64.

In addition, there were shifts to higher wavenumber of ν_{39} (*ca.* 10 cm^{-1}), ν_{51} (*ca.* 10 cm^{-1}), and ν_{44} (*ca.* 8-16 cm^{-1}). Also, the phenyl mode ϕ_4 lost intensity and a band at 1519 cm^{-1} essentially disappeared upon metal-centred oxidation. The pattern observed for the oxidation of the Mn(II) species was similar to that seen for the iron system except that the wavenumber shifts were larger. Most notably, the ν_{44} mode was seen to shift *ca.* 21 cm^{-1} upwards. In addition, ν_{41} shifted to higher wavenumber (*ca.* 13 cm^{-1}), as in the case of the cobalt system.

In relation to the magnitude of the absorbance changes produced upon ligand-centred oxidation, the porphyrin ring vibrational modes were seen to be increasingly perturbed by changes to the metal oxidation state in the order: Co < Fe < Mn. The removal of an electron from a molecular orbital with mainly d-character is expected to cause a change in the mixing between the d-orbitals and the ligand orbitals, which acts to transfer electron density back onto the metal (70). Such a perturbation would be likely to have an impact upon the ligand vibrational modes. Oxidation of a Mn(II) porphyrin is considered to involve depopulation of the $d_{x^2-y^2}$ orbital, whereas oxidation of a Co(II)

porphyrin involves depopulation of the d_{z^2} orbital (1b). Since the $d_{x^2-y^2}$ orbital should have greater overlap with the nitrogen centres of the porphyrin ring relative to that of the d_{z^2} orbital, it might be expected that a greater perturbation of the porphyrin ring vibrations would result from redox processes involving the $d_{x^2-y^2}$ orbital. Furthermore, the observed degree of perturbation decreases as the effective atomic number of the central metal increases. This is reasonable, since the size of the central metal should also be important in determining the degree of overlap between metal-based and porphyrin ring-based molecular orbitals. Therefore, the observed trend is suggested to reflect an increase in the degree of mixing between the metal d-orbitals and the porphyrin ring orbitals which arises from a reorganization of electron density during the electron transfer reaction.

CHAPTER SIX

THE ONE-ELECTRON OXIDATION OF DIFLUORO(TETRAPHENYLPORPHYRINATO)IRON(III): EVIDENCE FOR π -RADICAL CATION FORMATION

6.1 Introduction

In 1983 Hickman and Goff reported that the complex anion difluoro(tetraphenylporphyrinato)iron(III) underwent a one-electron oxidation at 0.68 V vs. SCE in dichloromethane containing 0.1 M tetrabutylammonium perchlorate (25a). This first oxidation potential is *ca.* 400 mV cathodic of the first oxidation of the fluoro(tetraphenylporphyrinato)iron(III) complex and most other five-coordinate iron(III) tetraphenylporphyrin complexes (21). Hickman and Goff observed that the products of the electrode reaction were capable of oxidizing added olefin substrates to the corresponding epoxides, allylic alcohols, and enones (25). Based on the potential shift and the partial reversibility of the electrode process as observed by cyclic voltammetry, they suggested that the immediate electrochemical product was an unstable difluoro iron(IV) porphyrin. However, they were unable to spectroscopically detect this species during their experiments and so could not provide direct evidence that their formulation was

correct.

During the course of this work on the influence of axial ligation upon the oxidation site in iron(III) porphyrins the anodic electrochemistry of difluoro(tetraphenylporphyrinato)iron(III) was reinvestigated using dc and in-phase ac cyclic voltammetry, as well as time-resolved thin layer u.v.-visible reflectance spectroelectrochemistry and *in situ* Fourier transform infrared reflectance spectroelectrochemistry. The results, which support formulation of the initial electrochemical product as a difluoro iron(III) porphyrin π -radical cation, are presented here.

6.2 Results

6.2.1 dc cyclic voltammetry

The difluoro(tetraphenylporphyrinato)iron(III) anion is generated by the addition of hydrated tetrabutylammonium fluoride to a dichloromethane solution of fluoro(tetraphenylporphyrinato)iron(III). The binding constant for this process has been reported as $4 \times 10^3 \text{ M}^{-1}$ at 25 °C (25). Under conditions of complete complexation the first oxidation of the difluoro iron(III) porphyrin occurs at 0.60 V vs. SCE when 0.1 M tetrabutylammonium hexafluorophosphate is used as supporting electrolyte. This is 0.50 V negative of the half-wave potential

($E_{1/2} = 1.10$ V vs. SCE) observed for oxidation of the monofluoro complex.

The anodic peak current is linear with the square root of scan rate in the range 50-500 mV s^{-1} indicating a diffusion-controlled reaction. Over this range of scan rates the reverse to forward peak current ratio increases from 0.7 to 0.9.

Cyclic voltammetry of the hydrated fluoride salt alone in dichloromethane containing 0.1 M tetrabutylammonium hexafluorophosphate indicates the presence of an irreversible electrode reaction which gives rise to small but measurable currents at potentials as low as 0.2 V vs. SCE (Figure 28c). This presumably arises from the oxidation of water added with Bu_4NF . In order to investigate what effect this might have on the porphyrin electrode reaction, the water content of the system was lowered by drying $\text{Bu}_4\text{NF} \cdot x\text{H}_2\text{O}$ at 40 °C under vacuum for 24 h as suggested by Cox *et al.* (71). It has been shown that the "nearly anhydrous" fluoride salt produced in this fashion is susceptible to a Hoffmann-type degradation which produces tetrabutylammonium bifluoride, 1-butene, and tributylamine (72). Since tributylamine was found to be electroactive in the potential range to be studied it was removed from the dried fluoride salt by washing with dry toluene. Solvent-supporting electrolyte solutions of the difluoro iron(III) porphyrin anion produced using this "nearly

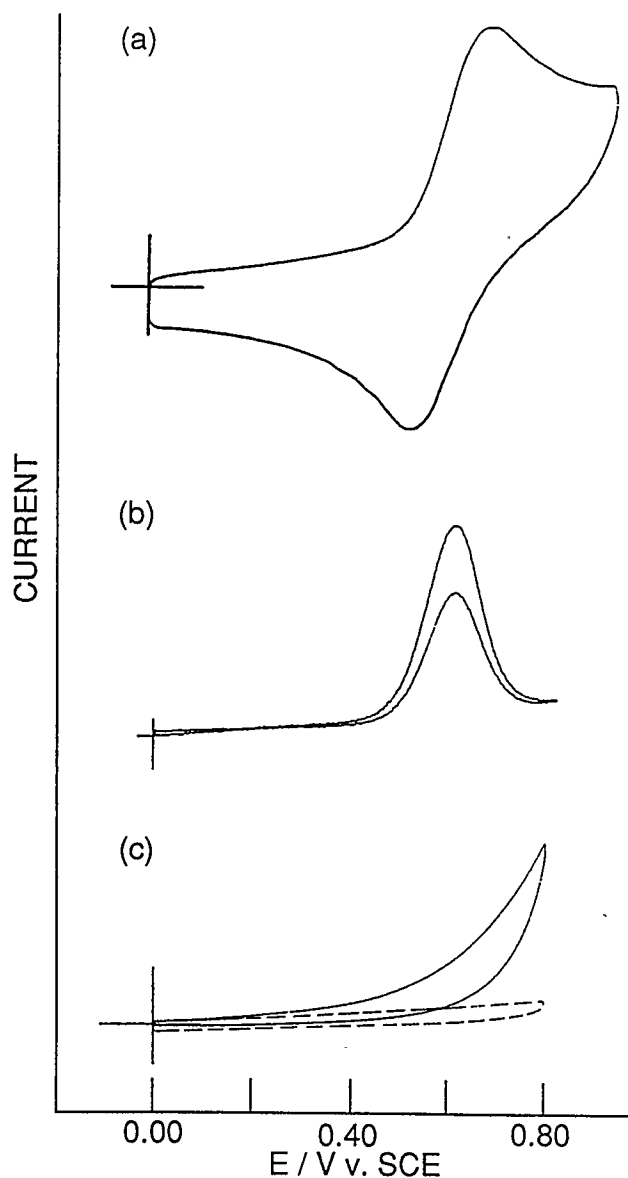


Figure 28 dc (a) and in-phase ac (b) cyclic voltammetry of $0.6 \text{ mM } [\text{Fe}^{\text{III}}(\text{tpb})]\text{F}$ in CH_2Cl_2 containing $0.1 \text{ M Bu}_4\text{NPF}_6$ and $3\text{-}6 \text{ mM dried Bu}_4\text{NF} \cdot x\text{H}_2\text{O}$. In (a), scan rate = 500 mV s^{-1} . In (b), scan rate = 5 mV s^{-1} , potential modulation = 10 mV p-p , 389 Hz . (c) dc cyclic voltammetry of $10 \text{ mM Bu}_4\text{NF} \cdot x\text{H}_2\text{O}$ in CH_2Cl_2 containing $0.1 \text{ M Bu}_4\text{NPF}_6$ (dashed line shows solvent-supporting electrolyte alone).

anhydrous" Bu_4NF display lower currents due to the irreversible electrode processes. Furthermore, the first oxidation of the difluoro iron(III) porphyrin anion becomes more chemically reversible. The reverse to forward peak current ratio increases from 0.8 at 50 mV s^{-1} and becomes unity at sweep rates greater than 200 mV s^{-1} (Figure 28a). The anodic peak current remains linear with square root of sweep rate in the range $50\text{-}500 \text{ mV s}^{-1}$.

6.2.2 *In-phase ac cyclic voltammetry*

The in-phase ac cyclic voltammetric response of the difluoro iron(III) porphyrin anion prepared using dried tetrabutylammonium fluoride was recorded at sweep rates in the range $5\text{-}25 \text{ mV s}^{-1}$. At 5 mV s^{-1} (Figure 28b) the ratio of the reverse to forward peak current amplitudes is 0.6. This ratio increases with increasing dc scan rate becoming 0.9 at 25 mV s^{-1} . At 5 mV s^{-1} the potential separation between the peaks on the forward and reverse scans is zero indicating rapid charge transfer kinetics on the dc timescale of the experiment. The forward peak width is 120 mV which is in reasonable agreement with the theoretical value of 90 mV expected for a one-electron reversible process.

6.2.3 Time-resolved thin-layer u.v.-visible reflectance spectroelectrochemistry

The spectral changes accompanying the electrolysis at 0.45 V of a CH_2Cl_2 solution containing difluoro(tetraphenylporphyrinato)iron(III) with 0.1 M Bu_4NPF_6 as supporting electrolyte are shown in Figure 29a. The difluoro iron(III) porphyrin anion in this and all subsequent experiments was prepared using dried tetrabutylammonium fluoride. At this potential no electrochemical oxidation of the difluoro iron(III) porphyrin anion can occur and the observed current is due to the irreversible water oxidation alone. However, it is seen that the spectrum of the difluoro iron(III) porphyrin anion is converted to one which is identical with that of the monofluoro iron(III) porphyrin. The conversion proceeds with observable isosbestic points consistent with a reaction involving two porphyrin chromophores. It follows that the irreversible water oxidation reduces the concentration of the difluoro iron(III) porphyrin anion by providing a means to remove free fluoride from the system. Water oxidation is expected to produce protons which would react further with fluoride to produce bifluoride. Conversion of fluoride to bifluoride was similarly suggested by Goff and co-workers (25b) to explain the production of the monofluoro iron(III) porphyrin observed during bulk electrolysis of the difluoro species.

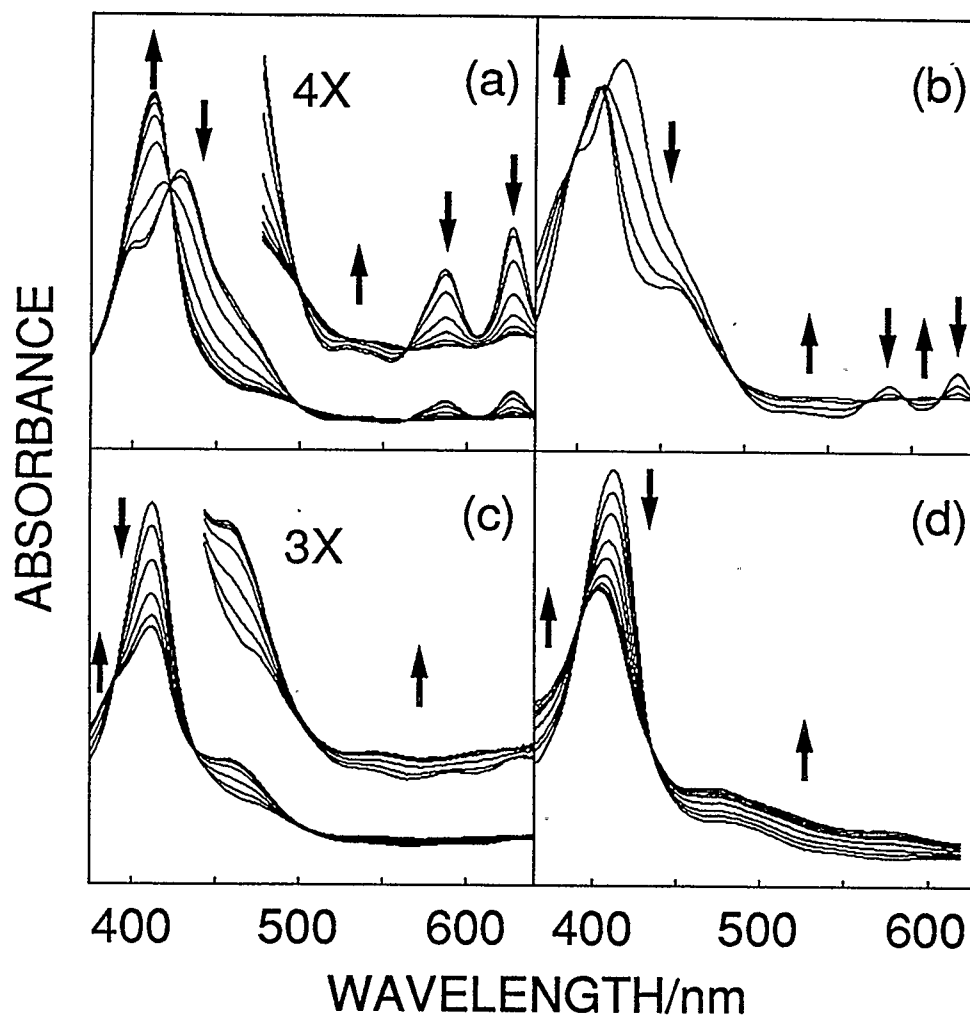


Figure 29 Time-resolved thin layer u.v.-visible reflectance spectroelectrochemistry of $[\text{Fe}^{\text{III}}(\text{tp})]\text{F}$ + excess dried $\text{Bu}_4\text{NF} \cdot x\text{H}_2\text{O}$ in CH_2Cl_2 containing 0.1 M Bu_4NPF_6 . (a) potential held at 0.45 V, 21.2 s between spectra (b) potential held at 0.80 V, 21.2 s between spectra (c) the second of two potential steps from 0.45 V to 0.80 V, 5.3 s between scans (d) $[\text{Fe}^{\text{III}}(\text{tp})]\text{F}$ in absence of Bu_4NF oxidized at 1.30 V, 2.7 s between spectra. All potentials are reported versus aqueous SCE.

The spectral changes associated with oxidation of a fresh thin-layer of electrolyte solution containing the difluoro iron(III) porphyrin anion at 0.80 V are shown in Figure 29b. The appearance of a band at 413 nm suggests that the monofluoro iron(III) porphyrin is being formed, presumably by the same sequence of reactions which resulted in its formation at 0.45 V. However, it is also seen that a partially resolved band near 450 nm and a broad featureless band in the visible region appear as the electrolysis proceeds. The absence of an isosbestic point near 415 nm implies that three or more porphyrin species are present.

After an electrolysis at 0.80 V vs. SCE for *ca.* 60 seconds to reduce the water content, the potential was stepped back to 0.45 V for *ca.* 20 seconds to reduce any oxidized porphyrin. The spectrum of the solution quickly reverted to the initial spectrum shown in Figure 29c. This spectrum indicates that the porphyrin at this point exists mainly as the monofluoro iron(III) complex, although the presence of two weak bands at 588 and 628 nm indicates that some of the difluoro species remains. The fluoride concentration has thus been significantly lowered during the preceding oxidation.

Figure 29c also shows the spectral changes to the thin layer solution on

stepping the potential back from 0.45 V to 0.80 V. During this subsequent electrolysis no further production of monofluoro iron(III) porphyrin is seen. Instead, the oxidation proceeds with well-defined isosbestic points producing a porphyrin species whose electronic spectrum contains a band near 450 nm as well as a broad featureless absorption in the visible region. Since the improved definition of isosbestic points in Figure 29c with respect to Figure 29b results from the loss of one chromophore i.e. the difluoro iron(III) porphyrin adduct, it is suggested that the spectral changes apparent in Figures 29b and 29c can be accounted for with a total of three chromophores.

It is significant that the potential at which the spectral changes of Figure 29c occur is 0.30 V negative of the half-wave potential observed for oxidation of the monofluoro porphyrin complex in the absence of any added fluoride. Thermodynamically, the one-electron oxidized monofluoro complex cannot exist at any appreciable concentration at this potential. The oxidation must be preceeded or followed by another reaction, for instance, complexation. Thus, while the fluoride concentration has been reduced below that required to completely complex all of the neutral monofluoro iron(III) porphyrin, it remains sufficient, in combination with a larger binding constant to the oxidized product, to facilitate oxidation to a significant degree. The final spectrum in Figure 29c

thus represents a mixture of $[\text{Fe}(\text{tpp})]\text{F}$ and the one-electron oxidized product $[\text{Fe}(\text{tpp})]\text{F}_2$. The three chromophores involved in the oxidation are thus suggested to be the unoxidized mono and difluoro adducts, $[\text{Fe}(\text{tpp})]\text{F}$ and $[\text{Fe}(\text{tpp})]\text{F}_2^-$, and the one-electron oxidized species $[\text{Fe}(\text{tpp})]\text{F}_2$.

Figure 29d shows the u.v.-visible spectral changes accompanying the electrolysis of $[\text{Fe}^{\text{III}}(\text{tpp})]\text{F}$ in CH_2Cl_2 containing 0.1 M Bu_4NPF_6 . The product of oxidation in this case is accepted as being a π -radical cation (21). Comparison of the final spectra in Figures 29c and 29d reveals that both the monofluoro and difluoro iron(III) porphyrin species give rise to oxidation products which produce a broad featureless absorption in the visible region. However, the spectrum of the oxidized difluoro iron(III) porphyrin has an absorption near 450 nm whereas the spectrum of the oxidized monofluoro iron(III) porphyrin does not. Thus, the two oxidized porphyrin species are distinct.

6.2.4 In situ FTIR reflectance spectroelectrochemistry

Figure 30a shows the mid-infrared difference spectrum associated with the electrochemical oxidation of fluoro(tetraphenylporphyrinato)iron(III) in dibromomethane containing 0.1 M tetrabutylammonium hexafluorophosphate.

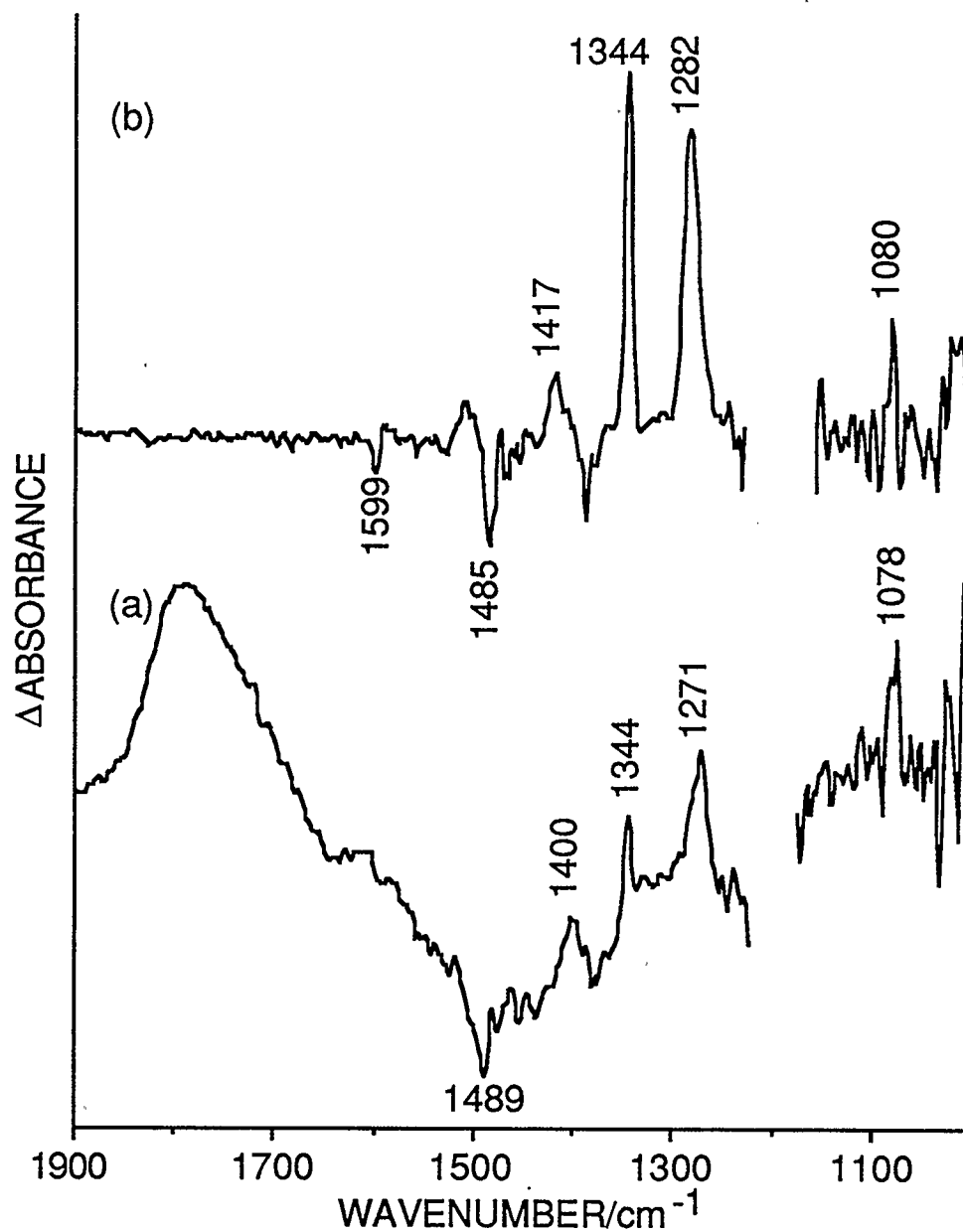


Figure 30 *In situ* FTIR difference spectra of the 1e oxidation of (a) [Fe^{III}(tpp)]F (b) [Fe^{III}(tpp)]F + excess dried Bu₄NF.xH₂O in CH₂Br₂-0.1 M Bu₄NPF₆.

The half-wave potential for the oxidation in this solvent was 1.16 V vs. SCE by cyclic voltammetry. Dibromomethane is preferred over dichloromethane for the *in situ* FTIR spectroelectrochemical studies of tpp complexes since the latter solvent absorbs strongly in the important (*vide infra*) region near 1270 cm^{-1} . Dibromomethane absorbs strongly near 1180 cm^{-1} , producing a high noise level in this region of the spectrum.

The positive absorbance (appearance) features indicate regions where the oxidized species absorbs more strongly than the unoxidized species. The negative absorbance (disappearance) features indicate regions where the oxidized species absorbs less strongly than the unoxidized species. As discussed in Chapter 5, the observed pattern of appearance and disappearance features seen in the figure has been shown to be characteristic of tetraphenylporphyrin π -radical cation formation but uncharacteristic of metal-centred redox processes. Most notably, the appearance feature at 1282 cm^{-1} is a recognized vibrational marker for tetraphenylporphyrin π -radical cations (11, 12). The appearance features at 1417 and 1508 cm^{-1} are associated with new bands of the π -cation radical not present in the unoxidized species (Chapter 5). The remaining appearance features at 1080 and 1344 cm^{-1} arise from an increase in intensity and a shift to higher wavenumber of

bands present at 1071 and 1339 cm^{-1} (KBr pellet) in the unoxidized complex. The disappearance features at 1599 and 1485 cm^{-1} result from a loss in intensity to porphyrin bands again present in the unoxidized system.

Figure 30b shows the mid-infrared difference spectrum associated with oxidation at 0.92 V of a thin electrolyte layer of difluoro(tetraphenylporphyrinato)iron(III) prepared by addition of excess dried tetrabutylammonium fluoride to the same solution used to obtain the difference spectrum of Figure 30a. The electrolysis potential is 0.24 V negative of the half-wave potential for oxidation of the monofluoro iron(III) porphyrin carried out in the absence of added fluoride, precluding observation of the one-electron oxidized monofluoro complex.

The changes to the porphyrin mid-infrared bands accompanying the electrolysis reaction are similar to those shown in Figure 30a. Two new bands appear at 1400 and 1271 cm^{-1} which are not present in the infrared spectrum of the unoxidized difluoro iron(III) porphyrin complex. Two further appearance features at 1078 and 1344 cm^{-1} arise from an increase in intensity and shift to higher wavenumber of bands present at 1070 and 1338 cm^{-1} (KBr pellet) in the isolated difluoro iron(III) porphyrin complex. A disappearance feature at 1489 cm^{-1} is associated with a loss of intensity of a band present in the unoxidized

system. While comparison between Figures 30b and 30a shows that the changes to the mid-infrared spectra accompanying the one-electron oxidation of both the monofluoro and difluoro iron(III) porphyrin complexes are very similar, it is clear from the small but significant differences in the position of bands in the two spectra, that the oxidized species produced from the two complexes are distinct.

The difference spectra associated with oxidation of the monofluoro and difluoro iron(III) porphyrin complexes were also observed using dichloromethane as solvent. With the exception of the observation of the marker band near 1280 cm^{-1} , which was obscured by strong absorbance due to the solvent, the spectral changes were equivalent to those observed in dibromomethane.

In addition to the observed changes to the porphyrin vibrations, Figure 29b also contains a broad bipolar feature comprised of a broad depression of the baseline absorbance in the region around 1450 cm^{-1} and a broad asymmetrical appearance feature near 1800 cm^{-1} . While the species giving rise to these features have not been conclusively identified, the same bipolar feature is seen when an electrolyte solution of tetrabutylammonium fluoride

alone is subjected to electrolysis at 0.92 V. The bipolar feature is not seen in the absence of the fluoride salt, and is thus ascribable to the irreversible process underlying the porphyrin oxidation.

6.3 Discussion

6.3.1 Site of oxidation in the difluoro iron(III) porphyrin anion - metal- versus ring-centred

In-phase ac and dc cyclic voltammetric studies show that the first oxidation of the difluoro(tetraphenylporphyrinato)iron(III) anion is a one-electron process which is free of coupled homogeneous reactions at moderate scan rates provided that the water content of the system is sufficiently lowered.

Time-resolved thin layer u.v.-visible reflectance spectroelectrochemistry shows that in the absence of a parallel oxidation of water, the porphyrin electrode reaction produces a single oxidized species whose electronic spectrum contains a band near 450 nm and a broad featureless absorption in the visible region. The presence of a broad featureless absorption in the visible region is recognized as being characteristic of porphyrin π -radical cation spectra (15). As such, the spectrum displayed by the oxidized difluoro iron(III) porphyrin anion is suggestive of a ring-centered electrode process. In contrast, the presence of a band near 450 nm in the spectrum of the oxidized species is untypical of

porphyrin π -radical cation spectra. However, it should be remembered that the absorption spectrum displayed by the six-coordinate difluoro iron(III) porphyrin anion itself is untypical of those of five-coordinate iron(III) porphyrins in that it displays significant absorption in the same region close to 450 nm. Thus, the band near 450 nm in the spectrum of the oxidized difluoro iron(III) porphyrin species is probably indicative of strong six-coordination around the iron center involving two axial fluoride ligands.

The *in situ* Fourier transform infrared reflectance spectroelectrochemistry provided the mid-infrared difference associated with the oxidation of the difluoro iron(III) porphyrin anion. Comparison of Figures 30a and 30b reveals that the oxidized species derived from the difluoro iron(III) porphyrin has a mid-infrared spectrum which is very similar to other tetraphenylporphyrin π -radical cations, and contains a band at 1271 cm^{-1} which is a marker for tetraphenylporphyrin π -radical cations. Moreover, the observed infrared spectral changes are not characteristic of metal-centered redox processes (Chapter 5). These results therefore also support the suggestion that the electrode process is centered at the porphyrin ring and not the central metal.

Taken together, the voltammetric and spectroelectrochemical studies of the

oxidation of the difluoro iron(III) porphyrin anion provide strong evidence that the single oxidation product is a difluoro iron(III) tetraphenylporphyrin π -radical cation. Thus, axial coordination by two fluoride ligands in iron(III) tetraphenylporphyrin complexes does not appear sufficient to alter the site of oxidation from the porphyrin ring to the central metal as previously suggested (25). This conclusion is consistent with the work of Groves *et al.* who observed that addition of methoxide to a perchlorato(tetramesitylporphyrinato)iron(III) π -radical cation produced a dimethoxy iron(IV) porphyrin, whereas addition of fluoride did not produce any observable iron(IV) species (13).

6.3.2 Origin of the shift of the first oxidation potential on coordination of fluoride to fluoro(tetraphenylporphyrinato)iron(III)

The addition of excess tetrabutylammonium fluoride to fluoro(tetraphenylporphyrinato)iron(III) in dichloromethane containing 0.1 M tetrabutylammonium hexafluorophosphate causes the apparent half-wave potential associated with π -radical cation formation and reduction to shift 500 mV cathodic from 1.10 V to 0.60 V. This observation can be rationalized in terms of the binding constant governing fluoride coordination to the π -radical cation being considerably larger than that for binding of fluoride to the monofluoro iron(III) porphyrin. The ratio of the magnitude of these two binding

constants can be estimated from the potential shift (14) and is found to be *ca.* 10^8 .

The ability of several anions - including fluoride - to produce potential shifts of *ca.* 300 mV in the half-wave potential associated with π -radical cation formation and reduction in (tetraphenylporphyrinato)zinc(II) has been reported (73), and it was suggested that there is a significant electrostatic contribution to the binding of anions to porphyrin π -radical cations. Thus, the idea that porphyrin ring oxidation potentials should be relatively insensitive to the axial coordination environment of the metal atom in high-spin iron porphyrin complexes (21) is probably only valid when the complexes being compared have the same overall charge. Therefore, it is not unreasonable to ascribe the 500 mV cathodic shift of the first oxidation of the difluoro iron(III) porphyrin relative to that of the monofluoro iron(III) porphyrin to the difference in overall charge between the two complexes resulting from the change in the metal coordination number from 5 to 6.

6.3.3 Nature of the chemical irreversibility associated with π -radical cation formation from difluoro(tetraphenylporphyrinato)iron(III)

The anodic oxidation of the difluoro iron(III) tetraphenylporphyrin anion is

seen by dc cyclic voltammetry to be a chemically reversible one-electron process at sweep rates greater than 200 mV s^{-1} . However, decreasing the sweep rate or raising the water content of the system results in a decrease in the reverse to forward peak current ratio which indicates that some loss of electroactive material is occurring.

The u.v.-visible thin-layer spectroelectrochemical studies indicate that the only porphyrin chromophore produced in addition to the difluoro π -cation radical is the unoxidized monofluoro complex. Furthermore, this process proceeds independently of the oxidation of the difluoro iron(III) porphyrin adduct. This process is presumably effected by protons produced by the electrolysis of water, resulting in the conversion of fluoride to bifluoride. Thus, at low sweep rates, the rate of proton production during the forward sweep is sufficient to deplete the free fluoride concentration such that unoxidized $[\text{Fe}^{\text{III}}(\text{tpp})]\text{F}_2^-$ diffusing in to the electrode from the bulk of solution is converted to $[\text{Fe}^{\text{III}}(\text{tpp})\text{F}]$. Since $[\text{Fe}^{\text{III}}(\text{tpp})\text{F}]$ in the absence of excess fluoride is not electroactive in the observed potential region, the concentration of oxidized species in the electrode vicinity available for reduction on the reverse sweep is lower than would be expected in the absence of proton production.

It is also possible, although less likely in view of the larger binding constant of F^- to the oxidized species, that proton production could result in loss of a fluoride from the difluoro π -cation radical to produce the monofluoro π -cation radical. Any of this species near the electrode would be immediately reduced, again resulting in reverse to forward peak current ratios of less than unity.

Figure 31 indicates the sequence of reactions proposed to account for the electrochemistry of $[Fe^{III}(tpp)F]$ in the presence of excess fluoride. In the scheme we have suggested hydrogen peroxide as the most likely product of the oxidation of water. Further oxidation to dioxygen is also possible, but we have not observed any gas evolution during the electrolysis reactions.

The proposed reaction scheme implies that the difluoro iron(III) porphyrin π -radical cation is not inherently unstable under the chosen experimental conditions. However, since iron porphyrins are known to react with peroxides and other oxidizing agents to produce unstable ferryl species which are capable of catalyzing the oxidation of organic molecules (2b) it is not possible to preclude a reaction scheme in which iron(III) porphyrin or iron(III) porphyrin π -radical cation combines with hydrogen peroxide from water oxidation to produce an oxo ferryl porphyrin species. These oxo ferryl porphyrins could then

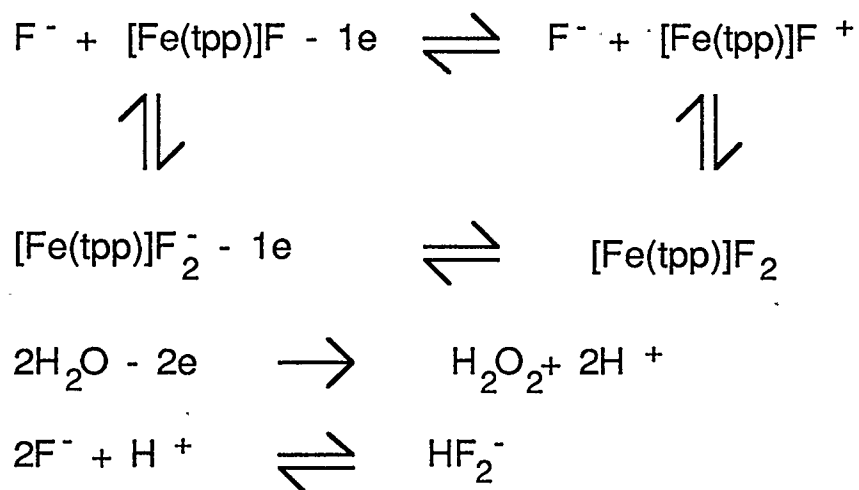


Figure 31 Proposed reaction scheme accounting for the electrode processes associated with the electrolysis of $[\text{Fe}^{\text{III}}(\text{tpp})]\text{F}$ in the presence of excess $\text{Bu}_4\text{NF} \cdot x\text{H}_2\text{O}$.

be rapidly reduced to the monofluoro iron(III) porphyrin with, for instance, concomitant oxidation of solvent *etc.*. The transient production of oxo ferryl porphyrin species by such a mechanism might explain the ability of this system to catalyze hydrocarbon oxidations, as observed by Goff and co-workers in their study of this electrode reaction (25).

CHAPTER SEVEN

THE ONE-ELECTRON OXIDATION OF HYDROXY(TETRAMESITYLPORPHYRinato)IRON(III): EVIDENCE FOR π -CATION RADICAL FORMATION

7.1 Introduction

The anodic oxidation of the sterically bulky five-coordinate iron(III) tetramesitylporphyrin with hydroxide as the axial ligand $[\text{Fe}(\text{tmp})]\text{OH}$, was first reported by Bruice and co-workers in 1985 (26b). The cyclic voltammetry in dichloromethane containing 0.1 M Bu_4NClO_4 showed two oxidations separated by *ca.* 140 mV in a potential region where the chloro derivative, $[\text{Fe}(\text{tmp})]\text{Cl}$, showed a single oxidation. It was proposed that the two oxidation waves were associated with step-wise formation of an iron(IV) porphyrin and an iron(IV) porphyrin π -cation radical and low temperature thin-layer u.v.-visible spectroelectrochemistry was subsequently used to spectrally characterize two electrogenerated intermediates (26c).

Different cyclic voltammetry was reported by Groves and Gilbert (26d) for $[\text{Fe}(\text{tmp})]\text{OH}$, in dichloromethane containing 0.1 M Bu_4NClO_4 and saturated

with Na_2CO_3 . In this case only one oxidation process at 1.0 V vs. SCE was observed. Low temperature bulk electrolysis of the hydroxy iron(III) porphyrin complex in the presence of excess Bu_4NOH produced a species with a u.v.-visible spectrum reminiscent of an oxo ferryl porphyrin and not a porphyrin π -cation radical.

The difference between Groves and Gilbert's voltammetry and that of Bruice and co-workers was ascribed by Groves to the presence of chloride in Bruice's experiments. In response to Groves and Gilbert's report, Bruice and Calderwood (26e) published evidence that no chloride was present in their system and that Groves and Gilbert's voltammetry could be reproduced if wet dichloromethane was used as solvent.

Following these communications Kadish and co-workers (26a) described a thorough investigation of both the oxidative and reductive electrochemistry and spectroelectrochemistry of $[\text{Fe}(\text{tmp})]\text{OH}$ using dc and steady-state voltammetries as well as thin-layer u.v.-visible spectroelectrochemistry. Their work suggested that the one-electron oxidized hydroxy iron porphyrin was unstable at room temperature and underwent one or more reactions producing either the chloro or the perchlorato derivative as the final product(s).

In the studies described above, spectral characterization of the electrogenerated intermediates was not possible on the voltammetric timescale at ambient temperature. In view of the reported instability of the initial electrode product (26a) it was felt that further study of the electrochemical oxidation of [Fe(tmp)]OH using short timescale *in situ* spectroelectrochemical techniques would be useful.

As part of a study into the influence of axial ligation upon the site of oxidation in iron(III) porphyrins the electrochemical oxidation of [Fe(tmp)]OH was reinvestigated using dc cyclic voltammetry under thin-layer or semi-infinite linear diffusion conditions as well as thin-layer u.v.-visible potential-resolved spectroelectrochemistry and double potential step chronoabsorptometry. The results, which suggest that the initial site of one-electron oxidation is porphyrin ring-centred and produces a hydroxy iron(III) porphyrin π -cation radical, are presented here.

7.2 Results

7.2.1 Cyclic voltammetry

The room temperature dc cyclic voltammetry of [Fe(tmp)]OH in dichloromethane containing 0.1 M Bu₄NClO₄ is shown in Figure 32a. The voltammetry is essentially identical to that previously reported by Kadish and

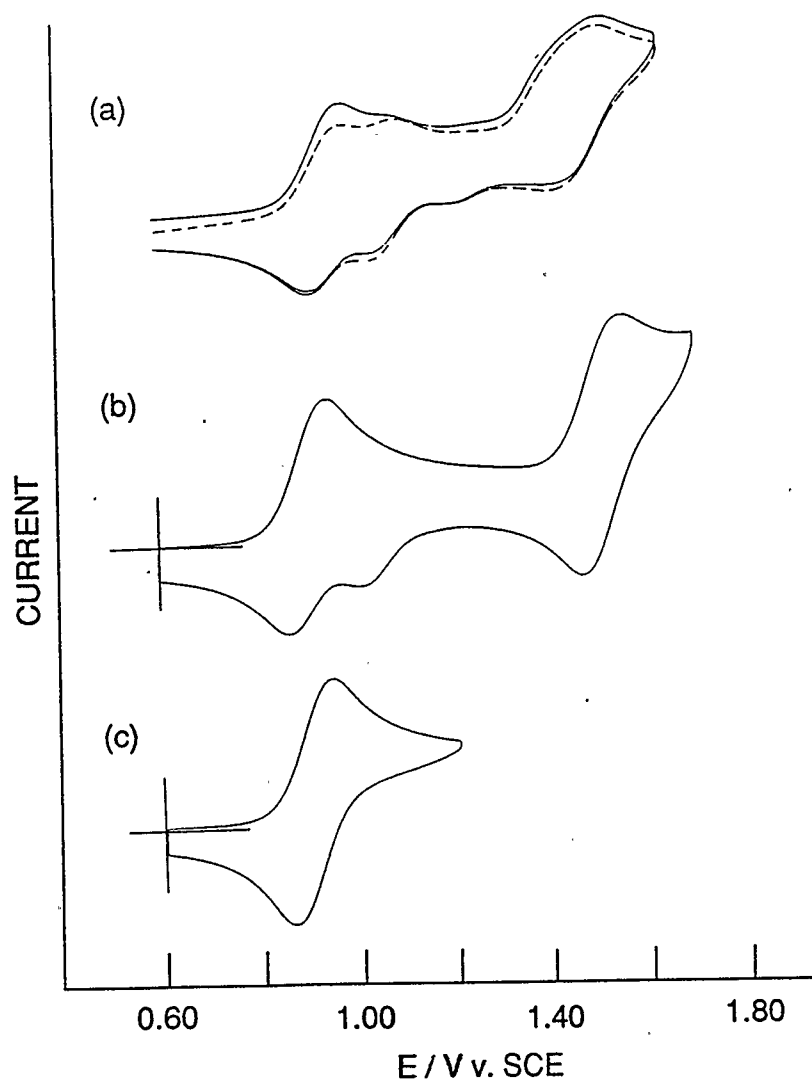


Figure 32 Cyclic voltammetry of 1 mM $[\text{Fe}(\text{tmp})]\text{OH}$ in dichloromethane containing (a) 0.1 M Bu_4NClO_4 and (b), (c) 0.1 M Bu_4NPF_6 . The sweep rate for all experiments was 100 mV s^{-1} .

co-workers (26a) and shows two oxidation processes with half-wave potentials of 0.97 and 1.08 V vs. SCE, and at least two further oxidation waves with anodic peak potentials of 1.28 and 1.55 V vs. SCE. Additional cathodic waves with peak potentials at 1.22 V and 1.44 V are observed during the reverse sweep.

During a subsequent scan (Figure 32a, dashed line) initiated immediately following completion of the first cycle, it is seen that the relative magnitude of the anodic peak currents corresponding to the oxidations at 0.97 and 1.08 V is altered. Thus, in the initial experiment the oxidation process at 0.97 V has the larger peak current (solid line). During the repeat cycle (dashed line) it is the oxidation at 1.08 V which gives rise to the larger peak current.

The voltammetry of the hydroxide complex in CH_2Cl_2 containing Bu_4NPF_6 is shown in Figure 32b. The use of hexafluorophosphate over perchlorate as the supporting electrolyte anion produces significant changes in the voltammetry. Two oxidation processes are observed at 0.90 V and 1.51 V vs. SCE. In addition a cathodic wave is observed at 1.01 V. Thus, a comparison of Figures 32a and 32b shows that the forward oxidation wave for the oxidation process at 1.08 V in CH_2Cl_2 containing 0.1 M Bu_4NClO_4 is not clearly evident when Bu_4NPF_6 is the supporting electrolyte. Steady state cycling between

0.4 V and 1.7 V causes a new anodic peak at 1.08 V to grow in, resulting in voltammetry very similar to that observed in CH_2Cl_2 -0.1 M Bu_4NClO_4 . The half-wave potential of this oxidation in CH_2Cl_2 containing 0.1 M Bu_4NPF_6 is estimated to be 1.04 V vs. SCE.

If the potential is switched at 1.30 V instead of 1.75 V then the initial oxidation process becomes completely reversible with a half-wave potential of 0.90 V vs. SCE (Figure 32c). No evidence of the oxidation process at 1.04 V is seen. The reverse to forward peak current ratios for the process at 0.90 V are unity in the range 50-150 mV s^{-1} . The peak current is also proportional to the square root of the sweep rate for sweep rates in the range 50-150 mV s^{-1} . At a sweep rate of 25 mV s^{-1} the reverse to forward peak current ratio was 0.9. All subsequent electrochemical and spectroelectrochemical experiments utilized 0.1 M Bu_4NPF_6 as supporting electrolyte.

It was observed that use of an SCE electrode caused formation of $[\text{Fe}(\text{tmp})]\text{Cl}$ at longer timescales. Addition of excess Bu_4NCl to $[\text{Fe}(\text{tmp})]\text{OH}$ in CH_2Cl_2 results in quantitative formation of the chloro complex. Thus, it is suggested that chloride leaking from the reference electrode compartment into the working electrode compartment caused the observed reaction. Use of a

Ag-AgPF₆ quasi-reference electrode in subsequent electrochemical experiments prevented any observable formation of [Fe(tmp)]Cl.

A combination of potential steps and a potential sweep was used to further probe the voltammetry of [Fe(tmp)]OH. The potential perturbations used for the experiments are shown in Figure 33. Thus, in experiment A, the potential was stepped from 0.6 V to 1.1 V for a 4 second period before being swept back to 0.6 V at 500 mV s⁻¹. After a 30 second delay to allow the analyte solution to relax, experiment B was initiated whereby the potential was stepped from 0.6 V to 1.2 V for a 4 second period before being stepped down to 1.1 V and then swept back to 0.6 V. Experiments C and D are similar to experiment B except that the potential steps were to 1.3 and 1.4 V, respectively. Thus, the overall time of the four experiments (A-D) is the same but the 4 second electrolysis occurs at increasingly positive potentials.

The potential sweeps from 1.1 V to 0.6 V resulting from experiments A to D are shown in Figure 34. It is seen that the reduction wave associated with the oxidation process at 1.04 V increases as higher potentials are accessed and in experiment D it appears that this occurs concomitant with a decrease in the reduction wave for the initial oxidation process. This demonstrates that the oxidation process at 1.04 V results from an overpotential-dependent process

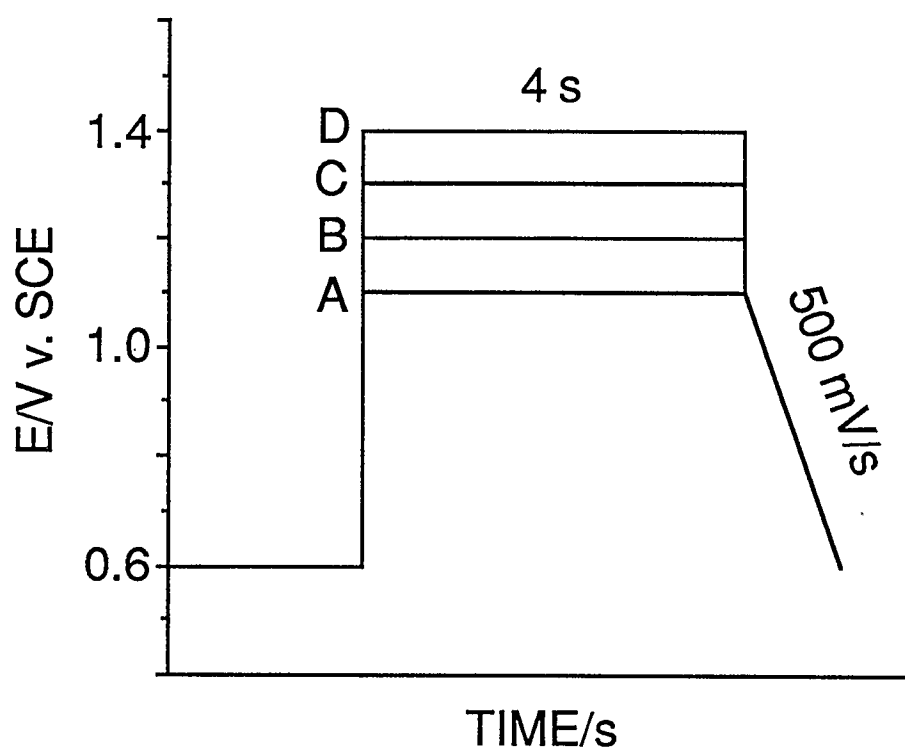


Figure 33 Potential programs used for voltammetric experiments A-D.

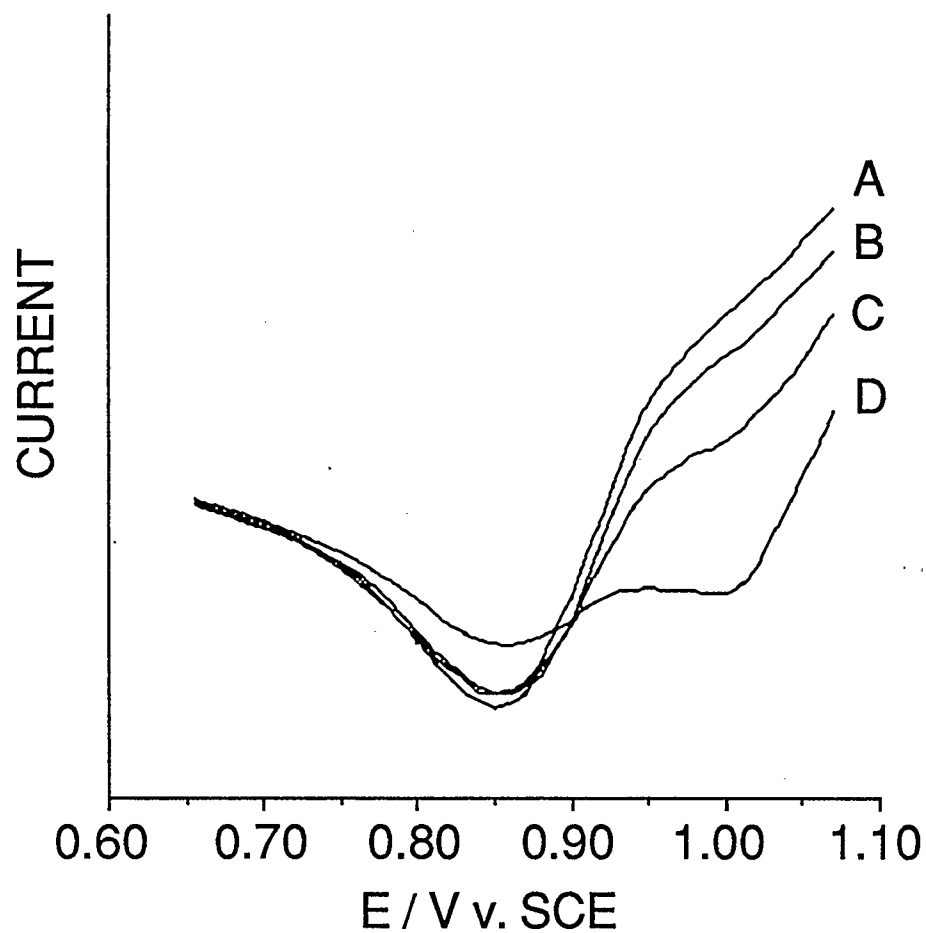


Figure 34 Combined potential step and sweep voltammetry of 0.25 mM $[\text{Fe}(\text{tmp})]\text{OH}$ in CH_2Cl_2 containing 0.1 M Bu_4NPF_6 . Voltammetry arising from the potential sweep portion of experiments A-D shown in Figure 33.

and implies that a slow irreversible heterogeneous process occurs in addition, or subsequent to, the initial oxidation process. One effect of this process appears to be the removal of material which gives rise to the reduction wave associated with the initial oxidation process at 0.90 V.

7.2.2 Double potential step chronoabsorptometry

Since the initial oxidation wave with half-wave potential at 0.90 V is reversible at moderate sweep rates provided that the switching potential is not too positive, it was possible to generate the u.v.-visible spectrum of the one-electron oxidized species using short timescale chronoabsorptometric experiments carried out under conditions of semi-infinite linear diffusion. Thus, absorbance-time transients were recorded at single wavelengths in the range 350-690 nm at intervals of 20 nm. Analyte concentrations were adjusted to produce an absorbance in the range 1.0-1.5 in the chronoabsorptometric cell at the analytical wavelength and were in the range 10^{-4} - 10^{-5} M. The potential was stepped to a point *ca.* 120 mV beyond the forward peak potential of the oxidation at 0.90 V vs. SCE for 1 second and then stepped back to the base potential, at which no electrolysis occurred, for 12 seconds prior to initiating a subsequent potential step. The spectra of the analyte solutions recorded prior to and after the experiments indicated that the iron(III) porphyrin remained in the hydroxide form. Cyclic voltammetry recorded before and after each

spectroelectrochemical experiment indicated that reversibility was maintained and that there were no local fluctuations of the analyte concentration in the vicinity of the working electrode.

The absorbance-time transient for the experiment performed at 350 nm is shown in Figure 35. For a reversible one-electron oxidation without homogeneous complications carried out under a condition of semi-infinite linear diffusion, the ratio of the absorbance at time 2τ relative to that at time τ should be 0.414 (14). The experimental value for the data shown Figure 35 is 0.414 ± 0.017 in excellent agreement with theory. Absorbance-time responses at other wavelengths also indicated that the absorbance changes were due to a reversible one-electron oxidation process without any complications during the timescale of the experiment.

A plot of the absorbance change for the forward step against the square root of the elapsed time is shown in Figure 36. The plot is linear for data collected at 100 ms and beyond and yields a zero intercept as predicted by theory (14). At times shorter than 100 ms the data is sub-linear presumably due to the time required to charge the double-layer capacitance (58). Since the bulk analyte concentration is known, and the diffusion coefficient was determined by

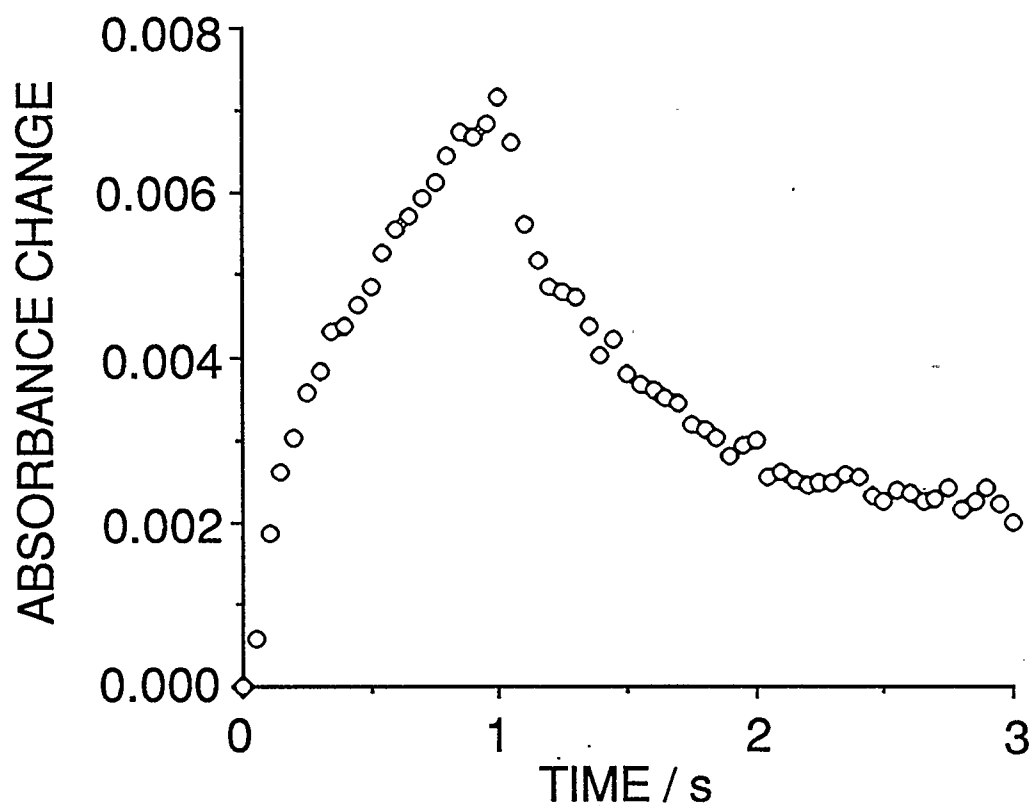


Figure 35 Absorbance-time transient recorded at 350 nm for 0.05 mM [Fe(tmp)]OH during double potential step chronoabsorptometry of the first one-electron oxidation in CH_2Cl_2 containing 0.1 M BuN_4PF_6 . The transient is the average of 64 experiments. The transient was smoothed by ten point averaging.

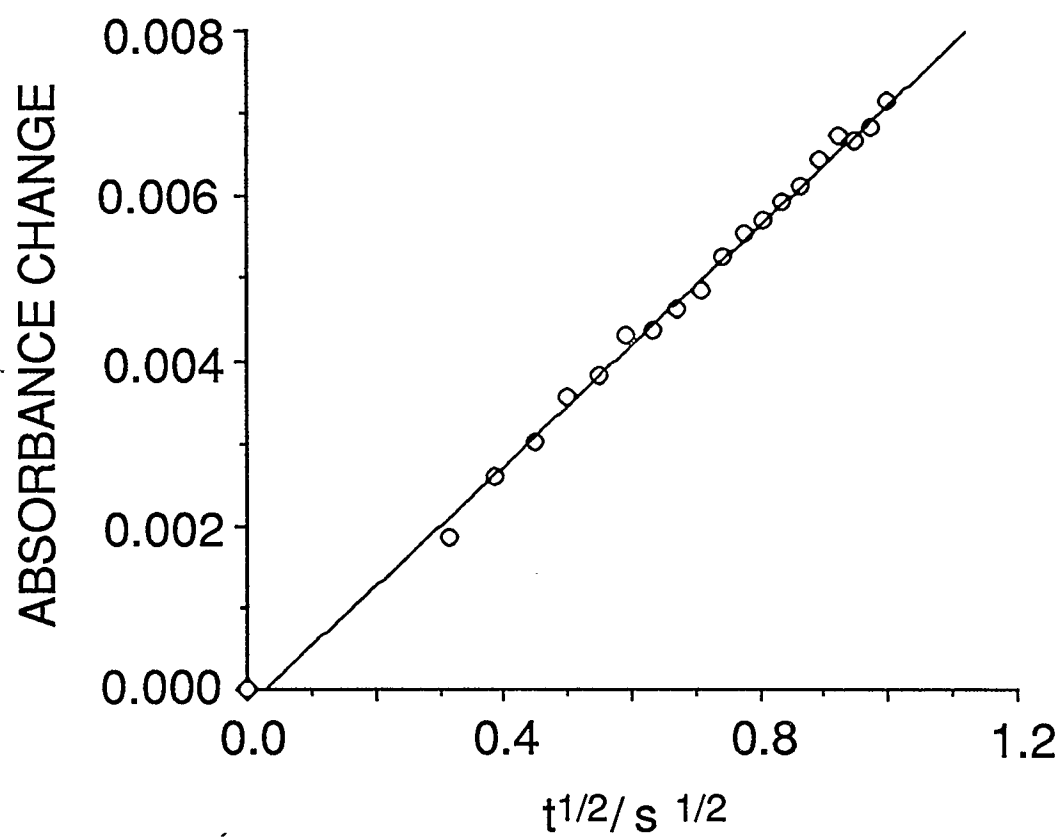


Figure 36 Plot of absorbance versus square root of time elapsed for the forward step of the data plotted in Figure 35.

chronoamperometry to be $5.33 \times 10^{-6} \text{ cm}^2 \text{ s}^{-1}$, the change in molar absorptivity, $\Delta\epsilon$ may be calculated from the slope according to Equation 2 (Chapter 4).

Figure 37 shows the u.v.-visible spectrum of the species produced from the reversible one-electron oxidation of $[\text{Fe}(\text{tmp})]\text{OH}$ (circles). The spectrum has been calculated from the molar absorptivity changes determined from chronoabsorptometric experiments carried out at different wavelengths. The spectrum of the parent hydroxy iron(III) porphyrin is shown for comparison (solid line). It is seen that the spectral changes associated with the chemically reversible one-electron oxidation of $[\text{Fe}(\text{tmp})]\text{OH}$ involve a broadening and blue-shifting of the Soret band and the appearance of a broad featureless increase in the visible region.

The spectral changes associated with the one-electron oxidation of $[\text{Fe}(\text{tmp})]\text{Cl}$ in dichloromethane containing Bu_4NClO_4 as measured by time-resolved thin-layer u.v.-visible spectroelectrochemistry are shown in Figure 38. The spectral changes are typical of those expected for formation of iron(III) porphyrin π -cation radicals.

The *in situ* FTIR difference spectrum associated with the one-electron

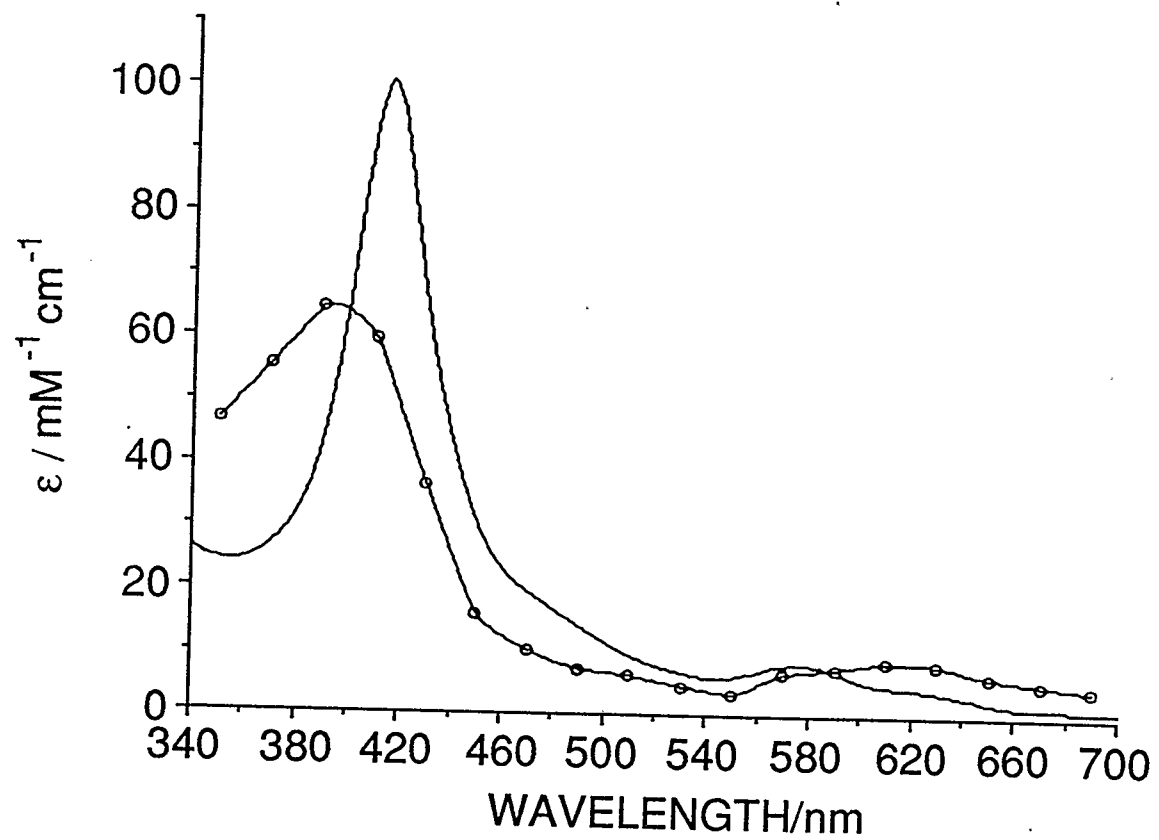


Figure 37 U.v.-visible spectra of $[\text{Fe}(\text{tmp})]\text{OH}$ (solid line) and its one-electron oxidized derivative (circles) in dichloromethane solvent.

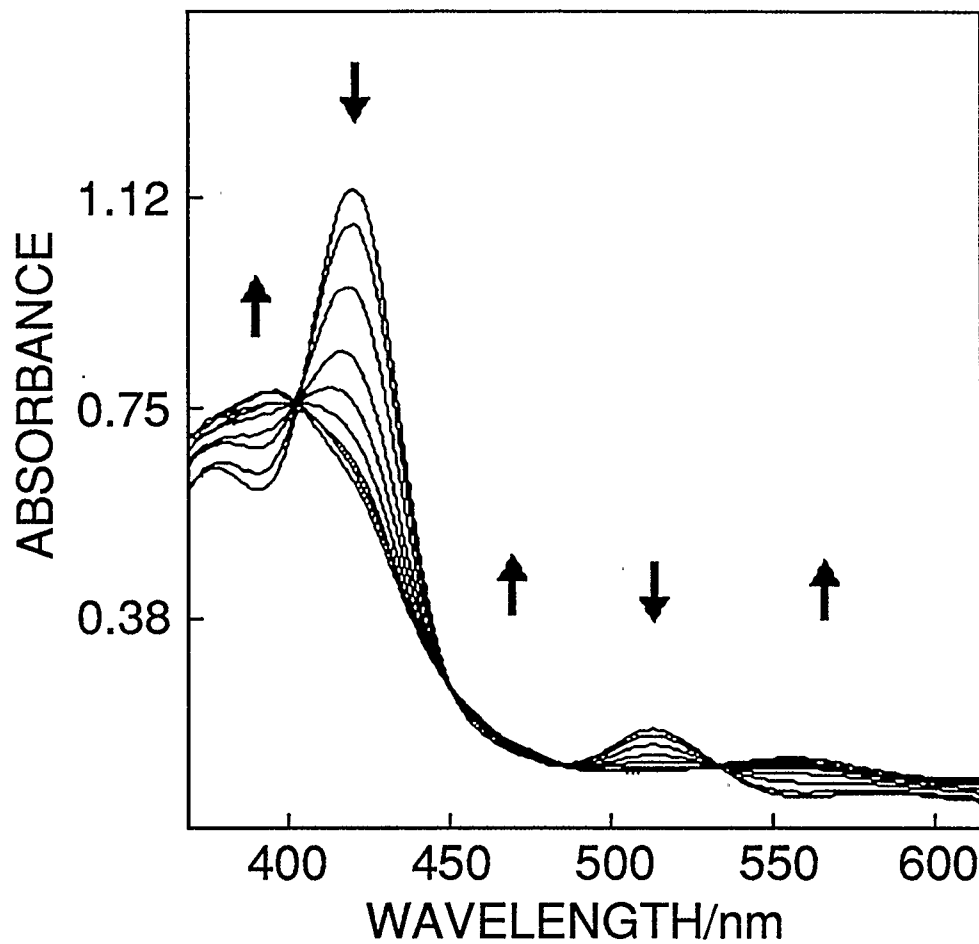


Figure 38 Time-resolved thin-layer u.v.-visible spectral changes associated with the one-electron oxidation of $[\text{Fe}(\text{tmp})]\text{Cl}$ in CH_2Cl_2 containing 0.1 M Bu_4NClO_4 .

oxidation of $[\text{Fe}(\text{tmp})]\text{Cl}$ in CH_2Br_2 containing 0.1 M Bu_4NPF_6 indicated that the oxidized product had a strong new infrared band at 1280 cm^{-1} which is a marker for ring-oxidation in tetraphenylporphyrins (11). Other appearance features were seen at 1608, 1426, 1336, 1072, and 1004 cm^{-1} . A disappearance feature was seen near 1478 cm^{-1} . The pattern is very similar to those produced by other tpp π -cation radicals (17, Chapter 5).

Comparison between Figures 37 and 38 shows that the spectral changes accompanying the 1e oxidation of $[\text{Fe}(\text{tmp})]\text{OH}$ and $[\text{Fe}(\text{tmp})]\text{Cl}$ both involve a broadening and blue-shifting of the Soret band and the appearance of a broad absorbance in the visible region. These results strongly suggest that the site of one-electron oxidation is the same for both complexes and is centred at the porphyrin ring forming iron(III) porphyrin π -cation radicals.

In situ FTIR spectroelectrochemistry of 2 mM $[\text{Fe}(\text{tmp})]\text{OH}$ in CH_2Br_2 containing 0.1 M Bu_4NPF_6 was carried out. A band at 1278 cm^{-1} appeared during electrolysis at 1.1 V indicating formation of a porphyrin π -cation radical. However, this infrared band cannot be unambiguously ascribed to the 1e oxidized $[\text{Fe}(\text{tmp})]\text{OH}$ since there is evidence (*vide infra*) that hydroxide would not remain coordinated to the iron porphyrin during the thin layer experiment.

*7.2.3 Thin-layer voltammetry and simultaneous linear potential sweep
u.v.-visible spectroelectrochemistry.*

Figure 39 shows the thin-layer voltammetry of 0.5 mM [Fe(tmp)]OH in dichloromethane containing 0.1 M Bu₄NPF₆ carried out in an external reflectance thin layer spectroelectrochemical cell. On the positive sweep it is seen that there are three major oxidation processes with anodic peak potentials at 0.26, ca. 0.35, and 0.53 V vs. the Ag-AgPF₆ quasi-reference electrode. On the reverse sweep only one major reduction with a reverse peak potential at 0.26 V vs. the Ag-AgPF₆ quasi-reference electrode is observed. In thin-layer cyclic voltammetry experiments carried out using thinner layers - and therefore lower current densities - the main reduction peak is actually 10 mV *anodic* of the main oxidation peak. The theoretical response for a chemically reversible process is expected to have coincident forward and reverse peak potentials (14). However, in a real thin layer cell iR drops arising from uncompensated solution resistance will tend to make the reduction peak potential more cathodic than the corresponding oxidation peak potential. The clear inference here is that the reduction peak does not correspond to reduction of the initial oxidation product.

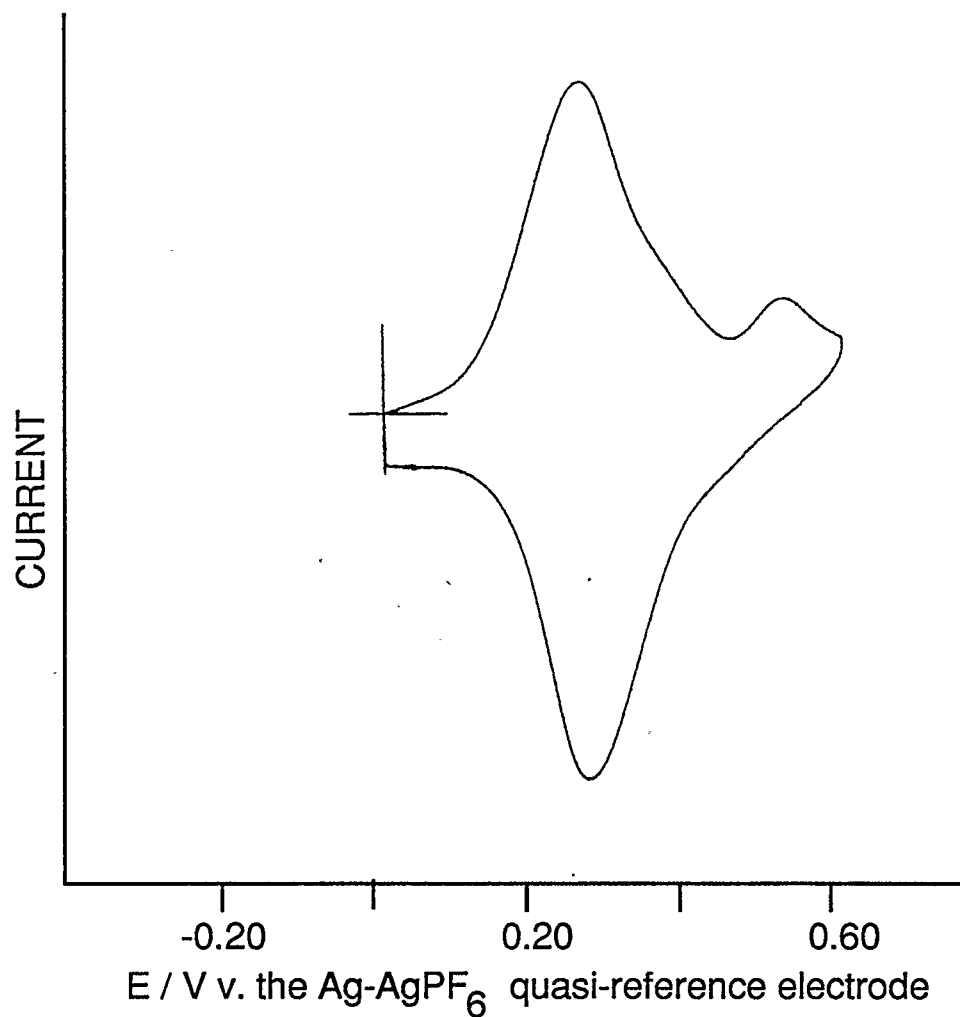


Figure 39 Thin-layer cyclic voltammetry of 0.5 mM [Fe(tmp)]OH in CH₂Cl₂ containing 0.1 M Bu₄NPF₆. Sweep rate is 5 mV s⁻¹. Potentials are vs. the Ag-AgPF₆ quasi reference electrode.

The thin layer u.v.-visible spectral changes recorded during the thin layer cyclic voltammetry experiment shown in Figure 39 at potentials between 0.00 V to 0.42 V vs. the Ag-AgPF₆ quasi-reference electrode on the forward sweep are shown in Figure 40. The spectra show the average absorbance change in sequential 14 s time periods. This translates into a potential separation between spectra of *ca.* 70 mV. Comparison of the spectral changes with the calculated spectrum of one-electron oxidized [Fe(tmp)]OH (Figure 37) show that this species is formed initially. However, loss of isosbestic points associated with the oxidation at *ca.* 0.35 V indicates that at least one additional porphyrin species is formed.

The thin layer u.v.-visible spectral changes recorded during the thin layer cyclic voltammetry experiment shown in Figure 39 at potentials between 0.42 V on the forward sweep and 0.51 V on the reverse sweep show formation of another porphyrin species with peaks at 520 and 589 nm (see Figure 41). This species is associated with the irreversible oxidation at 0.53 V. The thin layer u.v.-visible spectral changes recorded during the thin layer cyclic voltammetry experiment shown in Figure 39 at potentials between 0.5 V and 0.00 V on the reverse scan are shown in Figure 42. This process shows loss of the species with bands at 520 and 589 nm and reduction of one or more oxidized porphyrin species to form a final spectrum of an unoxidized

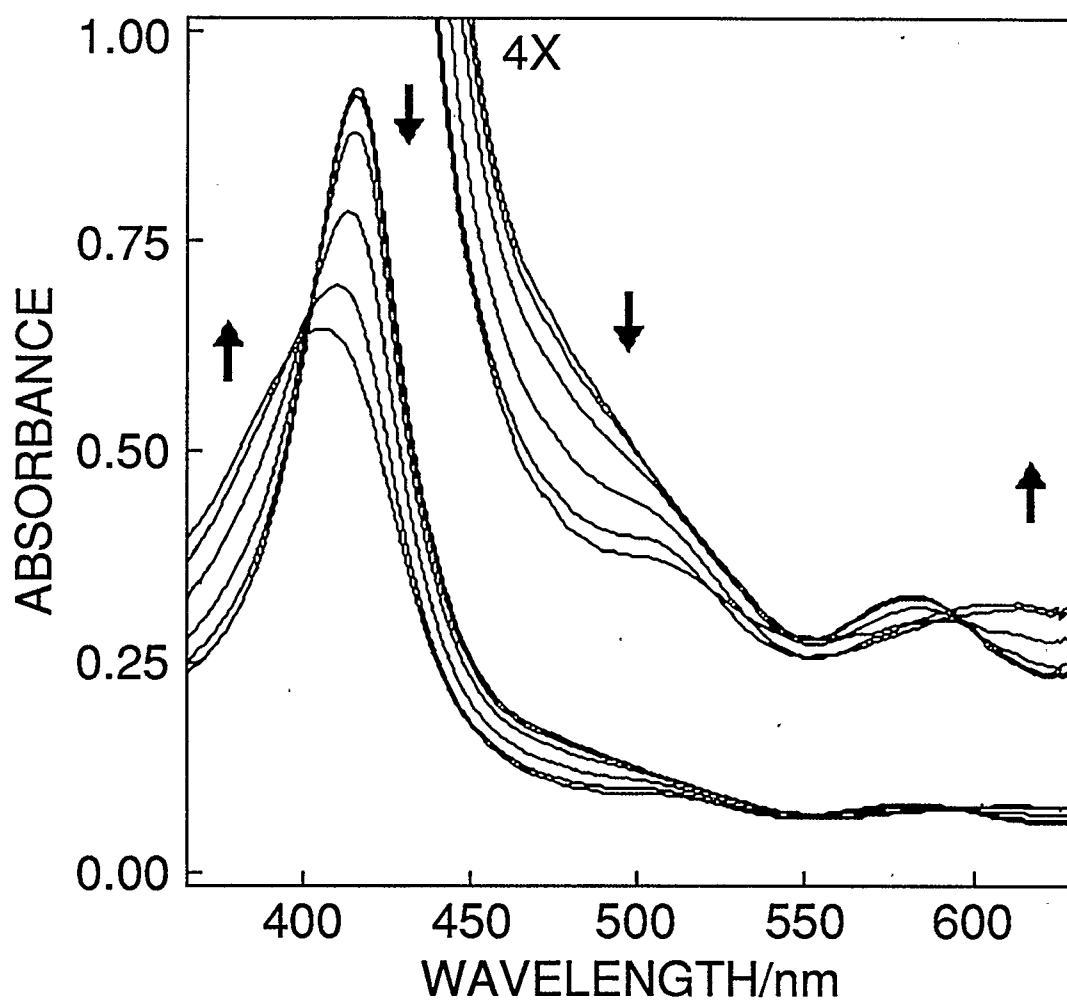


Figure 40 Thin-layer u.v.-visible spectral changes recorded during the thin-layer cyclic voltammetry experiment shown in Figure 39 at potentials between 0.00 V to 0.42 V vs. the Ag-AgPF₆ quasi-reference electrode on the forward sweep.

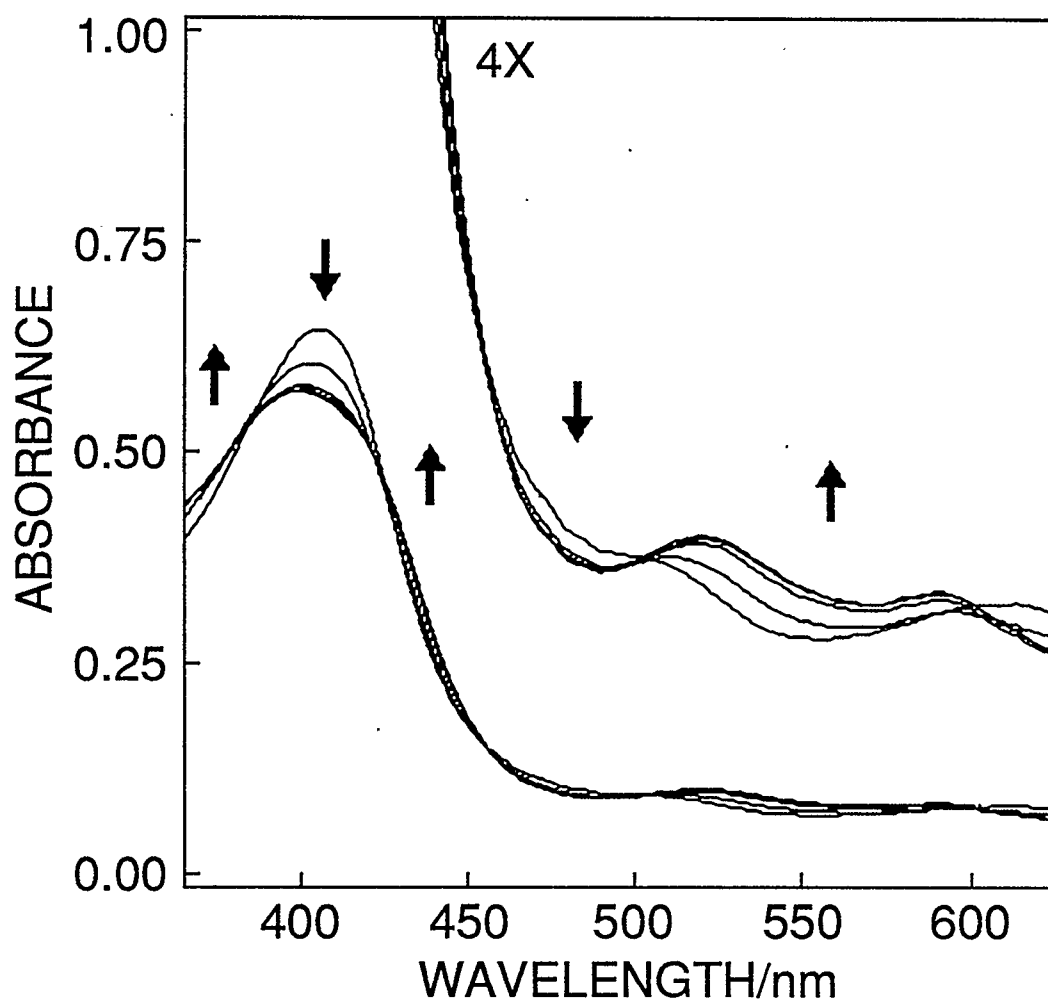


Figure 41 Thin-layer u.v.-visible spectral changes recorded during the thin-layer cyclic voltammetry experiment shown in Figure 39 at potentials between 0.42 V on the forward scan and 0.51 V on the reverse scan. Potentials are reported vs. the Ag-AgPF₆ quasi-reference electrode.

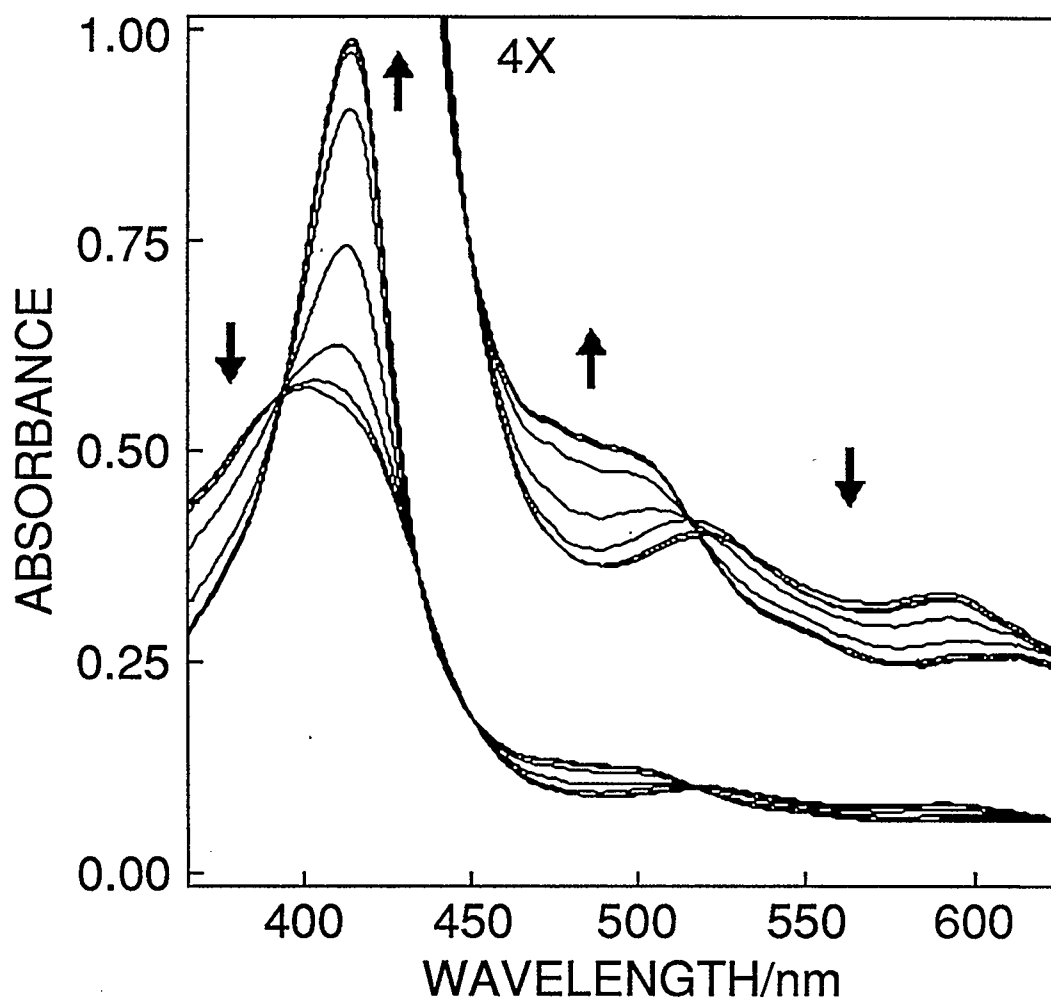


Figure 42 Thin-layer u.v.-visible spectral changes recorded during the thin-layer cyclic voltammetry experiment shown in Figure 39 at potentials between 0.51 V and 0.00 V vs. the Ag-AgPF₆ quasi-reference electrode on the reverse scan.

iron(III) porphyrin which is not due to either $[\text{Fe}(\text{tmp})]\text{OH}$ or $[\text{Fe}(\text{tmp})]\text{Cl}$. One possibility is that the spectrum is due to $[\text{Fe}(\text{tmp})]\text{PF}_6$ (*vide infra*).

7.3 Discussion

Cyclic voltammetry of $[\text{Fe}(\text{tmp})]\text{OH}$ shows that the first one-electron oxidation at 0.90 V vs. SCE is chemically reversible in dichloromethane at room temperature at moderate sweep rates provided Bu_4NPF_6 is used as the supporting electrolyte and that potentials do not become too positive. The u.v.-visible spectrum of one-electron oxidized $[\text{Fe}(\text{tmp})]\text{OH}$ is qualitatively similar to that of one-electron oxidized $[\text{Fe}(\text{tmp})]\text{Cl}$ which is typical of iron(III) porphyrin π -cation radicals (12). Further evidence that one-electron oxidation of $[\text{Fe}(\text{tmp})]\text{Cl}$ produces a porphyrin π -cation radical is provided by the *in situ* FTIR difference spectrum associated with the electrode reaction. This clearly indicates that the changes occurring to the porphyrin infrared bands are consistent with a porphyrin ring-centred process (17, Chapter 5).

On the basis of this evidence it is proposed that both $[\text{Fe}(\text{tmp})]\text{Cl}$ and $[\text{Fe}(\text{tmp})]\text{OH}$ undergo one-electron oxidation centred at the porphyrin ring to produce iron(III) porphyrin π -cation radicals. Thus, one hydroxide axial ligand does not appear capable of stabilizing an iron(IV) porphyrin under the experimental conditions.

The species which gives rise to the second oxidation at 1.04 V vs. SCE is produced by an overpotential-dependent process which results in loss of $[\text{Fe}(\text{tmp})]\text{OH}$. This new species undergoes one-electron oxidation producing a species with a u.v.-visible spectrum similar to that of known iron(III) porphyrin π -cation radicals (12). The reduced form of this iron(III) porphyrin species has a spectrum which is different to those of both $[\text{Fe}(\text{tmp})]\text{OH}$ and $[\text{Fe}(\text{tmp})]\text{Cl}$. In view of the work by Kadish and co-workers (25a) indicating that electrochemical oxidation of $[\text{Fe}(\text{tmp})]\text{OH}$ in CH_2Cl_2 containing 0.1 M Bu_4NClO_4 produced $[\text{Fe}(\text{tmp})]\text{ClO}_4$, the species produced under our conditions is tentatively identified as $[\text{Fe}(\text{tmp})]\text{PF}_6$.

The overpotential-dependent production of $[\text{Fe}(\text{tmp})]\text{PF}_6$ is suggested to involve an axial ligand-centred oxidation of hydroxide anion. Such axial-ligand oxidation has been previously observed with other iron(III) porphyrin complexes with electron-rich axial ligands such as phenolate (74) or imidazole (75). The formation of a transient short-lived iron(IV) porphyrin cannot be ruled out by our data. On the other hand, there is no need to invoke the existence of such a species to explain our results.

The different voltammetry displayed by $[\text{Fe}(\text{tmp})]\text{OH}$ in CH_2Cl_2 when

Bu_4NPF_6 is used instead of Bu_4NClO_4 as supporting electrolyte can also be rationalized by a slow heterogeneous oxidation of hydroxide. The perchlorate anion is more strongly coordinating than the hexafluorophosphate anion and consequently the formation of $[\text{Fe}(\text{tmp})]\text{ClO}_4$ will be more favourable than the corresponding formation of $[\text{Fe}(\text{tmp})]\text{PF}_6$. This explains in thermodynamic terms why the oxidation of hydroxide bound to $[\text{Fe}(\text{tmp})]\text{OH}$ resulting in the formation of $[\text{Fe}(\text{tmp})]\text{ClO}_4$ would be more favourable than a corresponding hydroxide oxidation which results in formation of $[\text{Fe}(\text{tmp})]\text{PF}_6$.

The irreversible oxidation in the thin layer voltammetry with a peak potential at 0.53 V vs. the Ag-AgPF₆ quasi-reference electrode is associated with the appearance of a new porphyrin species with bands at 520 and 589 nm. The identity of this porphyrin species cannot be unambiguously assigned on the basis of the results. The bands at 520 and 589 nm are not characteristic of either iron(III) porphyrin π -cation radicals (12) or oxo ferryl porphyrins (22d). The u.v.-visible spectrum of an iron(III) tetrakis(4-sulfonatophenyl)porphyrin N-oxide - which has oxo bridging iron and a pyrrole nitrogen - displays a red-shifted Soret band (441 nm) and two Q-bands at 544 and 602 nm. The spectrum of the iron(III) porphyrin N-oxide is, therefore, similar but not identical to that shown by the product of the oxidation at 0.53 V. In the light of this information, it is possible to

speculate that the product of the oxidation at 0.53 V might be an iron(III) porphyrin N-hydroxide. The iron(III) porphyrin N-hydroxide would be two-electron oxidized with respect to $[\text{Fe}(\text{tmp})]\text{OH}$. It should be categorically stated that the precursor(s) which could form such a species cannot be identified using the current data. The discussion outlined above is intended merely to provoke further experimentation in relation to this electrode process.

7.4 Conclusion

The first one-electron oxidation of $[\text{Fe}(\text{tmp})]\text{OH}$ is porphyrin ring-centred. An overpotential-dependent oxidation suggested to be centred at hydroxide results in formation of an iron(III) porphyrin which is tentatively identified as $[\text{Fe}(\text{tmp})]\text{PF}_6$. The complex $[\text{Fe}(\text{tmp})]\text{PF}_6$ undergoes an oxidation at 1.04 V vs. SCE. Another porphyrin species, which is speculatively identified as an iron (III) porphyrin N-hydroxide, is suggested to be the product of an irreversible oxidation process whose peak potential is at 0.53 V vs. the Ag-AgPF₆ quasi-reference electrode. The reactions thought to be involved in the electrochemical oxidation of $[\text{Fe}(\text{tmp})]\text{OH}$ are summarized in Figure 43.

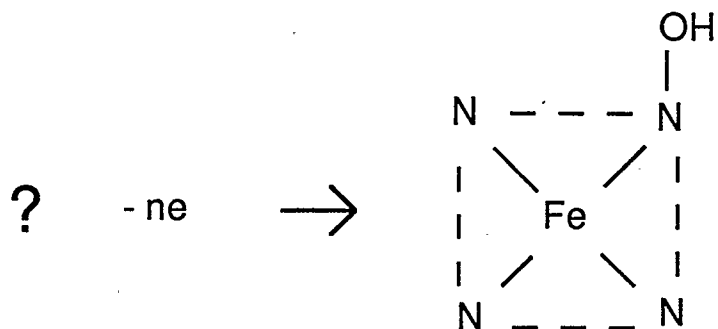
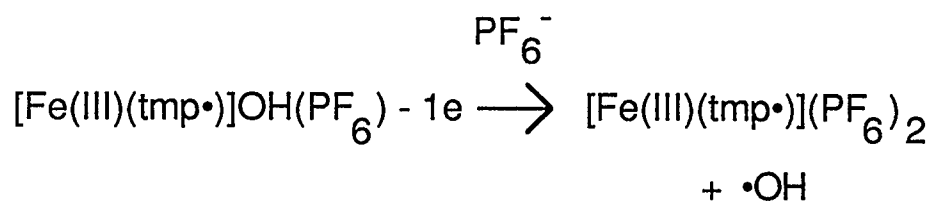
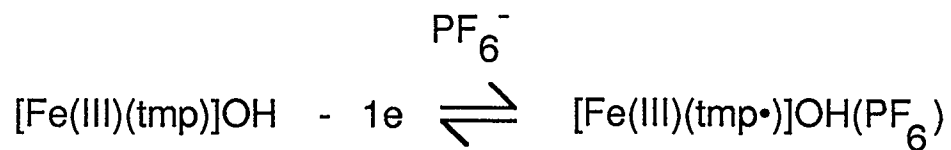


Figure 43 Reactions associated with the electrochemical oxidation of $[\text{Fe}(\text{tmp})]\text{OH}$ in CH_2Cl_2 containing Bu_4NPF_6 .

CHAPTER EIGHT

DENSITY FUNCTIONAL STUDIES OF IRON(III) PORPHINES AND THEIR ONE-ELECTRON OXIDIZED DERIVATIVES

8.1 Introduction

As part of a study on the types of axial ligation which would stabilize an iron(IV) porphyrin relative to the corresponding iron(III) porphyrin π -cation radical, we have examined one-electron oxidized iron porphyrin systems using approximate density functional theoretical methods. Our aim was to obtain useful information regarding the structure and relative stabilities of these oxidized iron porphyrins which might enable the important factors influencing their generation to be identified.

Additionally, we have sought to characterize the low-energy electronic transitions of the parent iron(III) porphyrin complexes using the density functional model. Our intent was to examine this important class of compounds using an alternative model to the *ab initio* (77) and INDO/CI (78) methods currently employed to study these systems.

8.2 Results and discussion

8.2.1 Relative energies of selected states of one-electron oxidized iron(III) porphines with one and two fluoride anions as axial ligands

The relative energies for selected states of one-electron oxidized fluoro iron(III) porphines $[\text{Fe}(\text{p})]\text{F}_2$ and $[\text{Fe}(\text{p})]\text{F}$ are shown in Table 6 and Table 7, respectively. For the difluoro species it is seen that the lowest energy state corresponds to a low-spin ($S=1$) iron(IV) species. Formation of a high-spin ($S=3$) A_{2u} π -cation radical requires an additional 0.57 eV. An intermediate spin ($S=2$) A_{2u} π -cation radical is 0.74 eV less stable than the iron(IV) porphyrin. In contrast, the lowest energy state for the monofluoro iron(III) porphine cation is the high-spin ($S=3$) A_{2u} π -cation radical which lies 0.70 eV below the iron(IV) ($S=1$) state and 1.09 eV below a high-spin ($S = 3$) A_{1u} π -cation radical.

The results suggest that one-electron oxidation of the isolated difluoro iron(III) porphine anion should be metal-centered producing an iron(IV) species, whereas a monofluoro iron(III) porphine should produce an iron(III) porphyrin π -cation radical. Therefore a crossover point in the relative stabilities of the two oxidized states is found which depends upon the nature of the axial ligation.

Axial ligation to iron(III) porphyrins by one fluoride anion results in π -cation

Table 6 Relative energy of selected states of $[\text{Fe}(\text{p})]\text{F}_2$.

$[\text{Fe}(\text{p})]\text{F}_2$	configuration							energy (eV)
	a_{1u}	a_{2u}	d_{xx-yy}	d_{zz}	d_{xz}	d_{yz}	d_{xy}	
Fe(IV), S=1	2	2	0	0	1	1	2	0.00
Fe(III) A_{2u} radical, S=3	2	1	1	1	1	1	1	0.57
Fe(III) A_{2u} radical, S=2	2	1	0	1	1	1	2	0.74

Table 7 Relative energy of selected states of $[\text{Fe}(\text{p})]\text{F}$

$[\text{Fe}(\text{p})]\text{F}^+$	configuration							energy (eV)
	a_{1u}	a_{2u}	d_{xx-yy}	d_{zz}	d_{xz}	d_{yz}	d_{xy}	
Fe(III) A_{2u} radical, $S=3$	2	1	1	1	1	1	1	0.00
Fe(IV), $S=1$	2	2	0	0	1	1	2	0.70
Fe(III) A_{1u} radical, $S=3$	1	2	1	1	1	1	1	1.09

radical formation on one-electron oxidation as predicted by theory (21, Chapter 6). Difluoro(tetraphenylporphyrinato)iron(III) was originally thought to produce an iron(IV) species on one-electron oxidation (25), however, the experimental work described in Chapter 6 suggests that the immediate electrode product is actually a π -cation radical.

One source of the difference between the experimental observations and the predictions of density functional theory may be a matrix effect. The difluoro(tetraphenylporphyrinato)iron(III) anion is produced experimentally by adding tetrabutylammonium fluoride trihydrate to a dichloromethane solution of the monofluoro iron(III) porphyrin (25). It is likely therefore that hydrogen-bonding between fluoride and water is important in these experiments. Support for this argument is provided by the crystal structure of the 2-methylimidazolium salt of the difluoro(tetraphenylporphyrinato)iron(III) anion (79). This contains quasi-linear hydrogen-bonded chains in which the 2-methylimidazolium cation is hydrogen bonded to two fluoride ions of two adjacent difluoro(tetraphenylporphyrinato)iron(III) anions. The suggested effect of this hydrogen bonding is a reduction in the donor properties of the fluoride anion relative to the isolated theoretical system. This reduction in donicity would be expected to favour formation of a high-spin iron(III) porphyrin π -cation radical over formation of a low-spin iron(IV) porphyrin for reasons which will be

discussed below. In addition, it should be noted that the iron(III) porphyrin π -cation radical and the iron(IV) porphyrin have quite different electronic structures. Therefore, it may also be possible that the present level of approximate DFT is unable to account for the difference in electron correlation between the two oxidized systems.

8.2.2 Molecular structures of one-electron oxidized difluoro iron(III) porphines

A full geometry optimization was carried out on the high-spin difluoro(porphyrinato)iron(III) anion, $[\text{Fe(III)(p)}]\text{F}_2^-$, and the corresponding one-electron oxidized low-spin iron(IV) species, $[\text{Fe(IV)(p)}]\text{F}_2$, as well as the high-spin A_{2u} π -cation radical species, $[\text{Fe(III)(p}\cdot)]\text{F}_2$. The system of nomenclature adopted for this work is shown in Figure 1 (Chapter 1). Selected geometrical parameters calculated for these systems are compared with the crystallographic geometry of difluoro(tetraphenylporphyrinato)iron(III) (79) in Tables 8 and 9. For the difluoro(porphyrinato)iron(III) anion, the calculated geometry is in good agreement with the crystallographic geometry of the derivative difluoro iron(III) tetraphenylporphyrin system. The tendency for local density functional methods to underestimate bond distances has been noted (80).

Table 8 Calculated bond distances for selected difluoro iron porphines

bond distances	[Fe(III)(p)]F ₂ ⁻	[Fe(IV)(p)]F ₂	[Fe(III)(p·)]F ₂	[Fe(III)(tpp)]F ₂ ⁻ ^a
Fe-F	1.923	1.793	1.912	1.966
Fe-N	2.013	1.953	2.022	2.064
N-C _α	1.374	1.391	1.373	1.377
C _α -C _β	1.423	1.415	1.426	1.441
C _α -C _m	1.368	1.363	1.375	1.403
C _β -C _β	1.355	1.355	1.352	1.341
C _β -H	1.082	1.080	1.093	-
C _m -H	1.090	1.084	1.093	-

^a Averaged values calculated from crystallographic data (79).

Table 9 Calculated bond angles for selected difluoro iron porphines

bond angles	[Fe(III)(p)]F ₂ ⁻	[Fe(IV)(p)]F ₂	[Fe(III)(p·)]F ₂	[Fe(III)(tpp)]F ₂ ^{- a}
Fe-N-C _α	126.1	127.0	126.2	126.0
C _α -N-C _α	107.9	105.9	107.5	107.6
N-C _α -C _β	108.4	109.2	108.6	108.5
N-C _α -C _m	126.8	127.2	126.0	125.9
C _α -C _m -C _α	124.3	121.3	125.3	125.5
C _α -C _β -C _β	107.7	107.8	107.6	107.8
C _α -C _β -H	124.4	124.1	124.5	-
C _α -C _m -H	117.8	119.3	117.3	-

^a Averaged values calculated from crystallographic data (79).

The calculated geometry of the high-spin A_{2U} π -cation radical is not significantly different from the parent anion. In particular, the Fe-N and Fe-F bond distances are not strongly affected by the removal of an electron from the porphyrin ligand. This result is in agreement with crystallographic data of isolated iron(III) porphyrin π -cation radicals (12). These systems all have Fe-N and Fe-X (X = axial ligand) bond distances which are similar to those in the parent high-spin iron(III) complexes.

Interestingly, the optimized high-spin A_{2U} π -cation radical system showed no inclination to adopt a 'saddle'-type ring conformation displayed by a number of porphyrin π -cation radicals in the solid state (12, 9). The difference in energy between the planar porphyrin ring and the saddle conformation was calculated to be only 0.65 eV. However, a geometry optimization performed on the A_{2U} π -cation radical state starting with a 'saddle'-type structure relaxed back to a planar geometry. Thus, it would appear that a 'saddle' conformation for A_{2U} porphine π -cation radicals would not be expected based on purely electronic considerations, and that steric (69) and perhaps solid-state effects (9) are more likely reasons for its observation in the crystal. This result is reasonable since the 'saddle' distortion of the porphyrin π -electron conjugated system acts to decrease the overlap between p-orbitals on the C_α and C_m centers. This

tends to raise the energy of the π -electrons in the porphine π -cation radical.

The calculated geometry for the difluoro iron(IV) porphine differed from the parent anion and the A_{2u} π -cation radical in that the Fe-N and Fe-F bond distances were shorter by *ca.* 0.1 Å (Table 8). From crystal field considerations it would be expected that shorter iron-ligand bond distances would help stabilize the low-spin Fe(IV) state. In contrast, the high-spin Fe(III) moiety present in the π -cation radical state should be favoured by a weaker crystal field and hence longer iron-ligand bond distances. The shorter metal-ligand bond distances also lend support to the idea that increased covalency in the metal-ligand interaction might help to stabilize the iron(IV) state (*vide infra*). The available experimental evidence suggests that iron-axial ligand bond distances in low-spin iron(IV) porphyrins are unusually short (2a). Furthermore, Fe-N bond distances in low-spin Fe(IV) porphyrins (2a) are similar to those observed in low-spin Fe(III) porphyrins but are significantly shorter than those seen in high-spin iron(III) porphyrins (6).

8.2.3 A possible spin-state/oxidation-site relationship in iron(III) porphyrins

Given that a clear relationship between spin-state and Fe-N bond distances exists for iron(III) porphyrins of a given coordination number (6), and that low-spin Fe(IV) porphyrins and high-spin iron(III) porphyrin π -cation radicals

display structural differences (*vide supra*), it is possible that the spin-state of iron(III) porphyrins and their site of oxidation might also be related. The assumption underlying this idea is that formal one-electron oxidations of iron(III) porphyrins proceed without significant structural rearrangement and therefore that the properties of the ligand set which favour one oxidized state over another are manifest to some degree in the iron(III) porphyrin precursor.

Tables 10 and 11 contain listings of high-spin, intermediate-spin, and low-spin iron(III) porphyrins with various axial ligands and the accepted sites of electron transfer on one-electron oxidation (at either the porphyrin ring, P, to form an iron(III) porphyrin π -cation radical, or the central metal, M, to form an iron(IV) porphyrin), and the expected oxidized product together with its spin-state. Although the data set is not exhaustive, it is interesting to note that practically all high-spin ($S=5/2$) and quantum-admixed-spin ($S=5/2, 3/2$) iron(III) porphyrins are considered to undergo one-electron oxidation to form iron(III) porphyrin π -cation radicals of the same spin-state (Table 10). In contrast, low-spin Fe(III) porphyrins may form either low-spin iron(IV) porphyrins or low-spin iron(III) porphyrin π -cation radicals on one-electron oxidation depending upon the type of axial ligation (Table 11).

The observations outlined above suggest that, in general, spin is preserved

Table 10 Site of one-electron oxidation in high- and intermediate-spin ferric porphyrins.

complex	spin-state	site	1e oxidized product	ref.
[Fe(tpp)]F	5/2	P	[Fe(tpp)]F(ClO ₄)	(21)
[Fe(tpp)]Cl	5/2	P	[Fe(tpp)]Cl(SbCl ₆)	(12)
[Fe(tpp)]Br	5/2	P	[Fe(tpp)]Br(ClO ₄)	(21)
[Fe(tpp)]I	5/2	P	[Fe(tpp)]I(ClO ₄)	(21)
[Fe(tmp)]OH	5/2	P	[Fe(tmp)]OH(PF ₆)	(Chapter 7)
[Fe(tpp)]F ₂ ⁻	5/2	P	[Fe(tpp)]F ₂	(Chapter 6)
[Fe(tpp)] ₂ O	5/2	P	[Fe(tpp)] ₂ O(ClO ₄)	(81)
[Fe(tpp)]NO ₃	5/2	P	[Fe(tpp)]NO ₃ (ClO ₄)	(21)
[Fe(tpp)]OPh	5/2	P	[Fe(tpp)]OPh(ClO ₄)	(21)
[Fe(tpp)]NCS	5/2	P	[Fe(tpp)]NCS(ClO ₄)	(21)
[Fe(tpp)](C ₆ F ₄ H)	5/2	M?	[Fe(tpp)](C ₆ F ₄ H)(ClO ₄)	(82)
[Fe(tpp)](ClO ₄)	5/2, 3/2	P	[Fe(tpp)]F(ClO ₄) ₂	(12)
[Fe(tpp)](OSO ₂ CF ₃)	5/2, 3/2	P	[Fe(tpp)](OSO ₂ CF ₃)(ClO ₄)	(83)

Table 11 Site of one-electron oxidation in low-spin ferric porphyrins.

complex	spin-state	site	1e oxidized product	ref.
[Fe(tmp)](OCH ₃) ₂ ⁻	1/2	M	[Fe(tmp)](OCH ₃) ₂	(13, 26a)
[Fe(tmp)](OH) ₂ ⁻	1/2	M	[Fe(tmp)]O + H ₂ O	(26a, 84)
[Fe(oep)]C ₆ H ₅	1/2	M	[Fe(oep)](C ₆ H ₅)(ClO ₄)	(85)
[Fe(tpp)] ₂ N	1/2	M	[Fe(tpp)] ₂ N ⁺	(86)
[Fe(tpp)] ₂ C ⁻	1/2?	M	[Fe(tpp)] ₂ C	(86a,87)
[Fe(oep)](ImH) ₂ Cl	1/2	P	[Fe(oep)](ImH) ₂ Cl(ClO ₄)	(88)

on one-electron oxidation of iron(III) porphyrins. Furthermore, it appears that only in the case of low-spin iron(III) porphyrins are the iron(IV) and iron(III) π -cation radical states both accessible on one-electron oxidation. The driving force for the formation of high-spin iron(III) porphyrin π -cation radicals from high-spin iron(III) precursors may be the retention of an exchange energy stabilization afforded by the high-spin Fe(III) configuration. Since low-spin Fe(IV) porphyrins and low-spin iron(III) porphyrin π -cation radicals have lower spin multiplicities the effects of exchange would be expected to be smaller than for the case of high-spin systems. Accordingly, differences in one-electron energies may be more important in determining the relative stability of the iron(IV) and iron(III) π -cation radical states.

Figure 44 shows interaction diagrams between metal-based d-orbitals and axial X ligands as well as σ -orbitals on N for an iron(IV) ($S=1$) state and an iron(III) ($S=1/2$) state. The bottom levels in each diagram are primarily represented by the ligand orbital with a small in-phase admixture from the metal-d component. The upper levels in each diagram are represented by the metal component with an out-of-phase contribution from the ligand orbital. The energy splitting between the two sets of levels in each diagram increases with the (a) σ - or (b) π -donor ability of the ligand. Since both states possess vacant

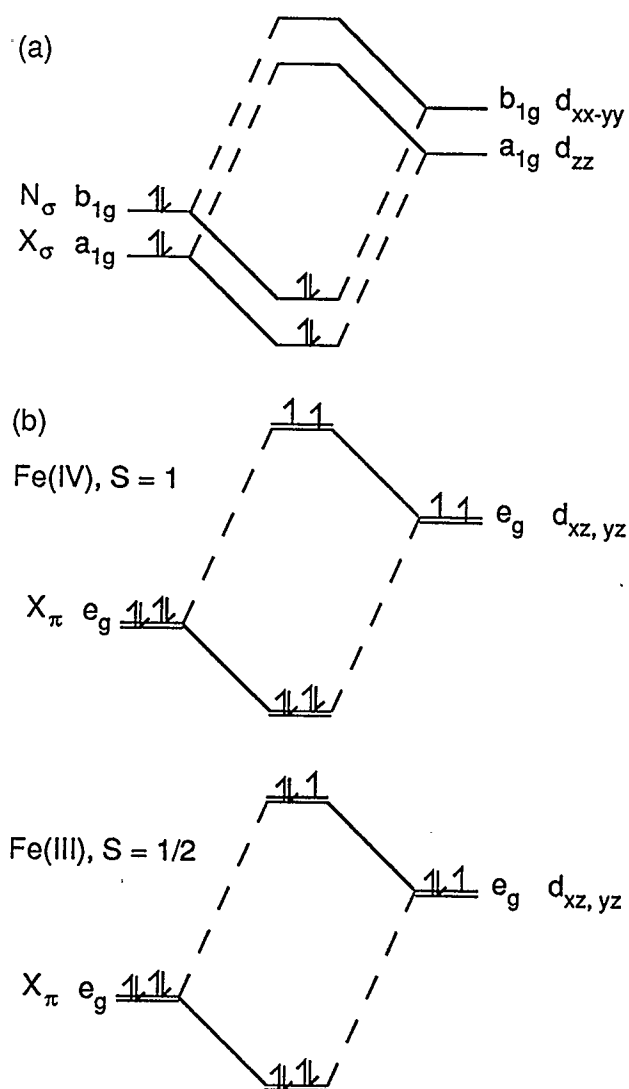


Figure 44 Interaction diagrams between metal-based d-orbitals and axial X ligands as well as σ -orbitals on N for an iron(IV) $S=1$ state and an iron(III) $S=1/2$ state (see text for discussion).

$d_{x^2-y^2}$ and d_{z^2} orbitals it appears that increased σ -donation (Figure 44a) would favour both states by about the same amount. In contrast, the effect of increasing π -donation (Figure 44b) is seen to favour low-spin iron(IV) over low-spin Fe(III) since an extra electron is destabilized by this interaction in the low-spin iron(III) case. It has previously been recognized that π -donation from the axial ligand to iron(IV) is important in stabilizing this high-valent state (2a, 89, 90).

An apparent exception to the relationship outlined above is the high-spin iron(III) porphyrins with σ -bonded perfluoroaryl axial ligands such as $[\text{Fe}(\text{tpp})](\text{C}_6\text{F}_4\text{H})$ and $[\text{Fe}(\text{tpp})](\text{C}_6\text{F}_5)$ (82). These systems are considered to undergo oxidation centered at iron to form iron(IV) derivatives in a fashion analogous to systems like $[\text{Fe}(\text{oep})]\text{C}_6\text{H}_5$ (85). From our considerations these high-spin iron(III) porphyrins might be expected to form high-spin iron(III) porphyrin π -cation radicals. The u.v.-visible spectral changes accompanying the oxidation of $[\text{Fe}(\text{tpp})](\text{C}_6\text{F}_4\text{H})$ reported by Guillard *et al.* (82) do appear - at least in our own view - reminiscent of those which accompany formation of iron(III) porphyrin π -cation radicals (12). Further spectroscopic characterization - particularly in the infrared - of the oxidized species formed in these reactions would be useful in clarifying this question.

8.2.4 $\pi \rightarrow \pi^*$ singlet transition energies of chloro(porphyrinato)iron(III)

The calculated $\pi \rightarrow \pi^*$ singlet transition energies of chloro(porphyrinato)iron(III) are shown in Table 12 together with experimental values for two widely-studied iron(III) porphyrin complexes (81, 91). The u.v.-visible spectra of iron porphyrins generally display an intense absorption close to 3.2 eV, known as the B-band or Soret band, and two weaker transitions near 2.4 eV, known as the Q-bands (see Figure 45). All these transitions display x, y-polarization. The calculated values are consistent with the assignment of the Q-band region as arising from $14a_1 \rightarrow 18e$ ($a_{2u} \rightarrow e_g^*$) and $5a_2 \rightarrow 18e$ ($a_{1u} \rightarrow e_g^*$) transitions. The B-band (Soret) region is suggested to arise from $8b_1 \rightarrow 18e$ ($b_{2u} \rightarrow e_g^*$) and $13a_1 \rightarrow 18e$ ($a_{2u}' \rightarrow e_g^*$) transitions. The $\pi \rightarrow \pi^*$ transitions shown in Table 12 are all fully allowed. The excited states are of E_u symmetry and are x, y-polarized. Furthermore, since they arise from electronic transitions within the porphyrin π -system they would be expected to be more intense than charge transfer or d-d transitions involving the paramagnetic iron center, and hence dominate the observed spectrum.

The present interpretation of the u.v.-visible spectrum of chloro(porphyrinato)iron(III) provides an alternative explanation to the popular

Table 12 Calculated singlet transition energies of chloro(porphyrinato)iron(III) (S=5/2)

transition	$\Delta E(\text{eV})$	$\Delta E_{\text{expt.}}(\text{eV})$	
		[Fe(tpp)]Cl ^a	[Fe(oep)]Cl ^b
13a ₁ → 18e	3.58	3.26 (B)	3.28 (B)
8b ₁ → 18e	3.14	2.97 (B)	
14a ₁ → 18e	2.45	2.42 (Q)	2.46 (Q)
5a ₂ → 18e	2.38		2.32 (Q)

^a Taken from ref. 81. ^b Taken from ref. 91.

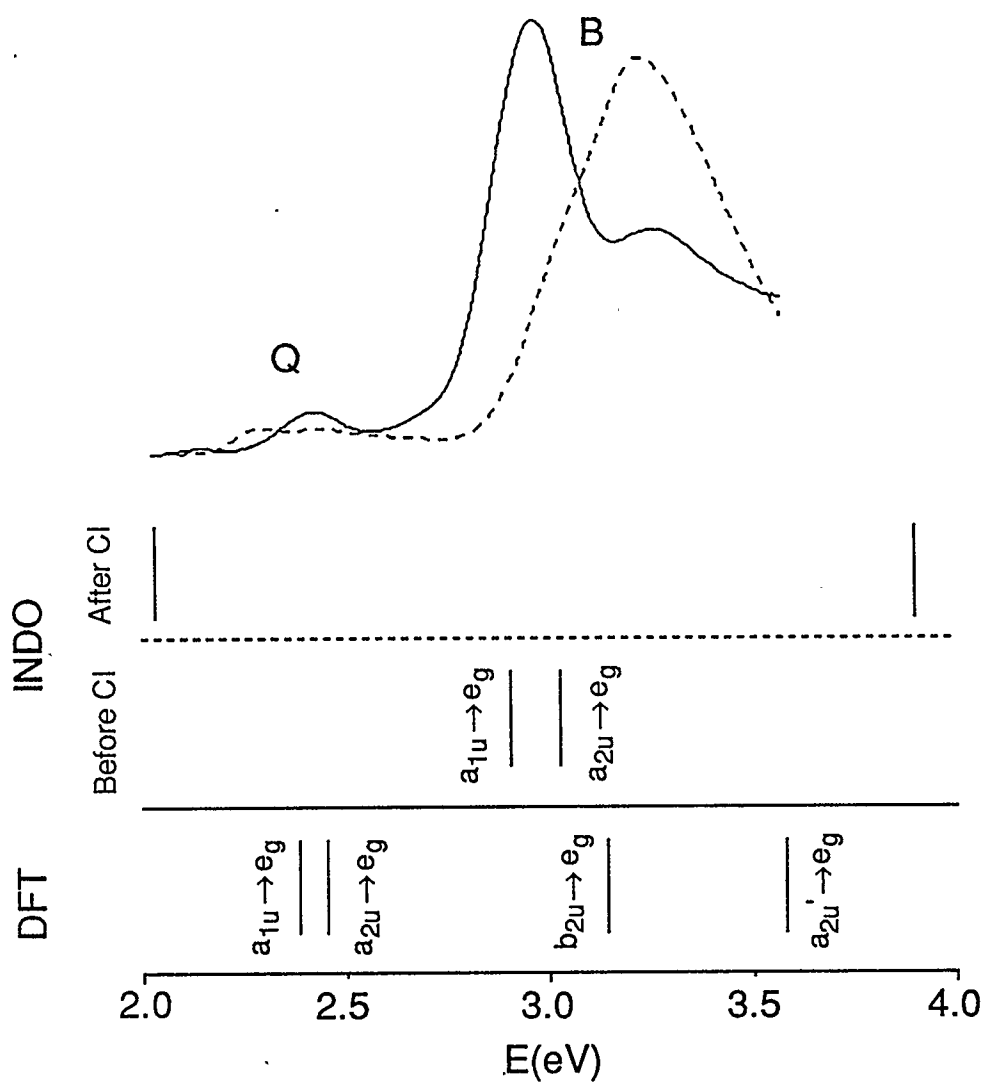


Figure 45 Comparison of calculated transition energies using INDO/CI methods (taken from ref. 78a) based on Gouterman's 4-orbital model, and HFS-LCAO methods (present work). The experimental spectra are those due to [Fe(tpp)]Cl (solid line) and [Fe(oep)]Cl (dashed line).

4-orbital model proposed by Gouterman (see Figure 45) (92). This model is based on an idea that the two highest filled porphyrin π -molecular orbitals of a_{1u} and a_{2u} symmetry are accidentally degenerate and that electronic transitions from these orbitals to the lowest unoccupied e_g^* level are consequently heavily mixed and produce an allowed B-state and a formally disallowed Q-state. A major success of this model is its ability to explain the large difference in intensity between the Q- and B-bands. However, attempts to quantify the model tend to overestimate the Q-B splitting (78a, 93).

Our alternative description using one-electron transitions is seen to produce an improved match between experimental and calculated transition energies. Unfortunately, we are unable to calculate intensities for the $\pi \rightarrow \pi^*$ transitions in Table 12. However, the B-band and Q-band in our assignment are suggested to arise from transitions involving different orbitals. Therefore, it is possible that the two sets of transitions could have quite different intensities. Previous calculations using INDO/CI (94) and IEHT (93) methods have suggested that transitions from the deeper b_{2u} and a_{2u}' π -orbitals mix together to give rise to transitions in the u.v. region (six-orbital model). The density functional calculations suggest that the energies of these transitions might have been over-estimated in previous studies.

Another point of interest is the origin of the two Q-bands. The four-orbital model predicts only one electronic transition in this energy range and the second band has been suggested to arise from vibrational-electronic coupling (95). In our alternative interpretation the two bands arise from two different electronic transitions.

CHAPTER NINE

CONCLUSIONS AND FUTURE WORK

9.1 Introduction

The present work has involved the application of spectroelectrochemical techniques to a study of metalloporphyrin electrode reactions. Of particular interest has been the elucidation of redox-site through *in situ* spectroscopic characterization of electrogenerated transient species. In this chapter a brief summary of the progress made will be outlined. Additionally, a topic for future work in this immediate area is proposed.

9.2 Summary of progress

A thin-layer u.v.-visible spectroelectrochemistry system has been constructed using a commercially available spinning-grating monochromator. The spectroelectrochemical experiment is capable of scanning a wavelength range of 369 to 617 nm in 2.1 ms. The time delay between successive scans is 83 ms. The maximum peak-to-peak noise level in a 300-point spectrum collected during 2.1 ms with a spectral bandwidth of 2 nm is 0.03 absorbance units. The anodic spectroelectrochemistry of [Cu(tpp)] was studied using the system. During one-electron oxidation of [Cu(tpp)] to form the corresponding

π -cation radical complete thin-layer electrolysis of 0.46 mM analyte in dichloroethane containing 0.16 M Bu_4NPF_6 was achieved in 12 s.

A chronoabsorptometric cell based on an external reflectance optical geometry has been constructed and incorporated into a double potential step chronoabsorptometry experiment. Experiments on the second timescale can be carried out at single wavelengths. Cottrell behaviour (theoretical response) is observed for data collected beyond 100 ms. The chronoabsorptometry of $[\text{Fe}(\text{tpp})]\text{Cl}$ in dichloromethane containing 0.1 M Bu_4NClO_4 was studied using the system and the u.v.-visible spectrum of the corresponding iron(III) porphyrin π -cation radical was constructed from single wavelength data. The relative percent errors in the calculated $\Delta\epsilon$ values were all less than 4%.

The difference spectra in the mid-infrared region associated with oxidation of the porphyrin ring in Mn(III), Fe(III), and Co(III) tetraphenylporphyrin complexes have been obtained by *in situ* FTIR spectroelectrochemistry, and are compared to those similarly observed for the corresponding metal(II)-metal(III) redox couples. Oxidation of the porphyrin ligand to the π -cation radical results in the appearance of three new bands near 1420, 1290, and 1230 cm^{-1} , as well as characteristic shifts and intensity changes of several bands present in the

parent complex. In contrast, the difference spectra associated with the metal(II)-metal(III) redox couple show less complex changes, the extent of which vary in the order $\text{Co} < \text{Fe} < \text{Mn}$. The spectral changes thus provide a means to differentiate between ligand- and metal-centred oxidation. In addition, the results provide insight into the nature of the infrared porphyrin ligand vibrations, as well as the character of the molecular orbitals associated with the oxidation processes.

The one-electron oxidation of the difluoro(tetraphenylporphyrinato)iron(III) anion has been studied using dc and in-phase ac cyclic voltammetry, time-resolved thin-layer u.v.-visible reflectance spectroelectrochemistry, and *in situ* FTIR reflectance spectroelectrochemistry. The first oxidation occurs at 0.60 V vs. SCE in dichloromethane containing 0.1 M Bu_4NPF_6 . If the water content of the system is sufficiently lowered the process is reversible at scan rates greater than 200 mV s^{-1} . At lower scan rates the reverse to forward peak current ratio gradually decreases from unity at 200 mV s^{-1} to 0.6 at 5 mV s^{-1} . Time-resolved thin-layer u.v.-visible reflectance spectroelectrochemistry shows that the electrode reaction produces a species with a broad featureless absorption in the visible region which is a characteristic feature of porphyrin π -cation radical spectra. Furthermore, *in situ* FTIR reflectance spectroelectrochemistry reveals that the oxidized porphyrin has a mid-infrared

spectrum which is very similar to that of other tetraphenylporphyrin π -cation radicals, and includes a band at 1271 cm^{-1} which is a marker for tetraphenylporphyrin π -cation radicals. The initial electrochemical product can thus be formulated as a difluoro iron(III) porphyrin π -cation radical. The observed chemical irreversibility of the electrode reaction is due, at least in part, to the irreversible oxidation of water present in the system. It is suggested that this parallel electrochemical process produces protons which convert excess free fluoride to bifluoride, resulting in formation of the monofluoro iron(III) porphyrin which in the absence of excess fluoride is electroinactive in the observed potential range.

The electrochemical oxidation of $[\text{Fe}(\text{tmp})]\text{OH}$ has been studied using dc cyclic voltammetry under thin-layer and semi-infinite linear diffusion conditions, as well as time-resolved thin-layer u.v.-visible reflectance spectroelectrochemistry and double potential step chronoabsorptometry. The one-electron oxidation of $[\text{Fe}(\text{tmp})]\text{OH}$ occurs at 0.90 V vs. SCE and is reversible in CH_2Cl_2 if Bu_4NPF_6 is used instead of Bu_4NClO_4 as supporting electrolyte, and the potential is not swept too positive. Double potential step chronoabsorptometry on a second timescale in which the one-electron oxidation was reversible allowed the point-by-point construction of the u.v.-visible spectrum of the one-electron oxidized product. The spectral

changes on one-electron oxidation involve a broadening and blue-shifting of the Soret band and the appearance of a broad absorbance in the visible region indicating that ring-centred oxidation is occurring to form the iron(III) porphyrin π -cation radical. Combined potential step and potential sweep voltammetry indicates that a species which gives rise to an oxidation process at 1.04 V is formed by an overpotential-dependent process. Simultaneous thin-layer dc cyclic voltammetry and linear potential sweep thin-layer u.v.-visible reflectance spectroelectrochemistry suggest that hydroxide is oxidized during the electrolysis of $[\text{Fe}(\text{tmp})]\text{OH}$ and a species tentatively identified as $[\text{Fe}(\text{tmp})]\text{PF}_6$ is formed which is itself electroactive in the observed potential region. Another iron porphyrin is formed during an irreversible oxidation at 0.53 V vs. the Ag-AgPF_6 quasi-reference electrode. It is speculatively identified as an iron(III) porphyrin N-hydroxide.

The relative energies of selected states for one-electron oxidized $[\text{Fe}(\text{p})]\text{F}_2$ and $[\text{Fe}(\text{p})]\text{F}^+$ have been studied using approximate density functional methods. For the difluoro derivative an iron(IV) ($S=1$) state is stabilized relative to an iron(III) A_{2u} π -cation radical ($S=3$) state. For the monofluoro species this ordering is reversed. The molecular structures of difluoro(porphyrinato)iron(III) and the corresponding iron(IV) and iron(III) A_{2u} π -cation radical species have

been investigated using a full geometry optimization. The A_{2U} π -cation radical species has a geometry very similar to that of the parent compound. In contrast, the iron(IV) derivative displays significantly shortened Fe-N and Fe-F bond distances. A possible relationship between iron(III) spin-state and the site of one-electron oxidation in iron(III) porphyrins is rationalized in terms of exchange energy stabilization and the σ - and π -donor properties of the axial ligand(s).

The $\pi \rightarrow \pi^*$ singlet transition energies of $[\text{Fe}(\text{p})]\text{Cl}$ have been calculated. Good agreement with experimental values is found and an assignment of the Q-band region as arising from $14a_1 \rightarrow 18e$ ($a_{2U} \rightarrow e_g^*$) and $5a_2 \rightarrow 18e$ ($a_{1U} \rightarrow e_g^*$) transitions is proposed. The B-band (Soret) region is suggested to arise from $8b_1 \rightarrow 18e$ ($b_{2U} \rightarrow e_g^*$) and $13a_1 \rightarrow 18e$ ($a_{2U'} \rightarrow e_g^*$) transitions.

9.4 Future work: The 1e oxidation of σ -bonded aryl iron(III) porphyrins

The groups of Kadish and Guillard have collaborated to investigate the synthesis and redox properties of σ -bonded aryl iron(III) porphyrins (96). Their work resulted in the characterization of a number of high- and low-spin iron(III) porphyrins in which aryl and perfluoroaryl groups were σ -bonded to the metal centre. On one-electron oxidation these complexes were considered to form

iron(IV) species. In the case of complexes like $[\text{Fe}(\text{oep})]\text{C}_6\text{H}_5$ and $[\text{Fe}(\text{tmp})]\text{C}_6\text{H}_5$ there is spectroscopic characterization of the high-valent derivatives which supports an Fe(IV) formulation (85, 90). The proposed relationship between spin-state and site of oxidation suggests that these low-spin Fe(III) porphyrins could be oxidized to form low-spin Fe(IV) derivatives provided that the phenyl anion is a sufficiently strong π -donor in the iron porphyrin system (90).

Although σ -bonded phenyl iron(III) porphyrins are low-spin, complexes such as $[\text{Fe}(\text{tpp})]\text{C}_6\text{F}_4\text{H}$ or $[\text{Fe}(\text{tpp})]\text{C}_6\text{F}_5$ are high-spin (82). On one-electron oxidation these complexes are also considered to form iron(IV) porphyrins. However, this assignment of oxidation site would not be expected from a consideration of the proposed spin-state/oxidation site relationship since high-spin Fe(III) porphyrins would be expected to form high-spin iron(III) porphyrin π -cation radicals. Examination of the spectral changes reported by Guillard *et al.* (82) as accompanying the one-electron oxidation of $[\text{Fe}(\text{tpp})]\text{C}_6\text{F}_4\text{H}$ show a broadening and blue-shifting of the Soret band and the appearance of a broad absorbance in the visible region. These spectral changes are thus reminiscent of those accompanying formation of an iron(III) porphyrin π -cation radical (12). In contrast, the u.v.-visible spectrum of

one-electron oxidized $[\text{Fe}(\text{oep})]\text{C}_6\text{H}_5$ is similar to that of the iron(III) porphyrin precursor which is consistent with spectra of other iron(IV) porphyrins (22d, 85). Furthermore, Kadish and Guillard report that one-electron oxidized low-spin σ -bonded aryl iron porphyrins undergo an N-phenyl shift whereas the high-spin derivatives are much more stable and do not undergo this reaction (96).

In view of the reported stability of the one-electron oxidized high-spin σ -bonded perfluoroaryl iron porphyrins it is proposed that an *in situ* FTIR reflectance spectroelectrochemical study of these species be carried out to further probe the oxidation site in the iron(III) porphyrin precursors.

REFERENCES

- (1) (a) M. W. Makinen and A. K. Churg. Iron Porphyrins Part I. *Edited by* A. B. P. Lever and H. B. Gray. Addison-Wesley, Reading MA. 1983. pp. 141-235. (b) M. Gouterman. The Porphyrins Vol. 3. *Edited by* D. Dolphin. Academic Press, New York. 1978. pp. 1-165.
- (2) (a) L. A. Andersson and J. H. Dawson. *Struct. Bonding (Berlin)* **71**, 1 (1991). (b) I. Tabushi. *Coord. Chem. Rev.* **86**, 1 (1988). (c) W. D. Hewson and L. P. Hager. The Porphyrins Vol. 7. *Edited by* D. Dolphin. Academic Press, New York. 1978. pp. 295-332. (d) D. Dolphin. The Biological Chemistry of Iron, N.A.T.O. Advanced Studies Institutes Series C Vol. 89. *Edited by* H. B. Dunford, D. Dolphin, K. N. Raymond, and L. Sieker. D. Reidel, Boston MA. 1982. pp. 283-294.
- (3) (a) T. C. Bruice. *Aldrichemica Acta* **21**, 87 (1988). (b) J. H. Dawson and K. S. Eble. *Adv. Inorg. Bioinorg. Mech.* **4**, 1 (1986). (c) B. R. James. The Porphyrins Vol. 5. *Edited by* D. Dolphin. Academic Press, New York. 1978. pp. 205-302. (d) F. P. Guengerich and T. L. MacDonald. *Acc. Chem. Res.* **17**, 9 (1984). (e) R. E. White and M. J. Coon. *Annu. Rev. Biochem.* **49**, 315 (1980). (f) B. Morgan and D. Dolphin. *Struct. Bonding (Berlin)* **64**, 115 (1987).

- (4) J. W. Buchler. Porphyrins and Metalloporphyrins. *Edited by* K. M. Smith. Elsevier, Amsterdam. 1975. pp. 157-231.
- (5) J. E. Falk. Porphyrins and Metalloporphyrins. Elsevier, Amsterdam. 1964. pp. 3-29.
- (6) W. R. Scheidt and C. A. Reed. *Chem. Rev.* **81**, 543 (1981).
- (7) W. R. Scheidt and M. Gouterman. Iron Porphyrins Part I. *Edited by* A. B. P. Lever and H. B. Gray. Addison-Wesley, Reading MA. 1983. pp. 89-139.
- (8) (a) J. L. Hoard. Porphyrins and Metalloporphyrins. *Edited by* K. M. Smith. Elsevier, Amsterdam. 1975. pp. 317-380. (b) W. R. Scheidt. The Porphyrins Vol. 3. *Edited by* D. Dolphin. Academic Press, New York. 1978. pp. 463-511.
- (9) W. R. Scheidt and Y. J. Lee. *Struct. Bonding (Berlin)* **64**, 1 (1987).
- (10) K. M. Kadish. *Prog. Inorg. Chem.* **34**, 435 (1986).
- (11) E. T. Shimomura, M. A. Phillippi, H. M. Goff, W. F. Scholz, and C. A. Reed. *J. Am. Chem. Soc.* **103**, 6778 (1981).
- (12) P. Gans, G. Buisson, E. Duee, J.-C. Marchon, B. S. Erler, W. F. Scholz, and C. A. Reed. *J. Am. Chem. Soc.* **108**, 1223 (1986).
- (13) J. T. Groves, R. Quinn, T. J. McMurry, M. Nakamura, G. Lang, and B. Boso. *J. Am. Chem. Soc.* **107**, 354 (1985).

- (14) A. J. Bard and L. R. Faulkner. *Electrochemical Methods, Fundamentals and Applications*. John Wiley and Sons, New York. 1980. pp. 577-656.
- (15) J.-H. Fuhrop. *Struct. Bonding (Berlin)* **18**, 1 (1974).
- (16) Z. Gasyna and M. J. Stillman. *Inorg. Chem.* **29**, 5101 (1990).
- (17) (a) A. S. Hinman and B. J. Pavelich. *Can. J. Chem.* **65**, 919 (1987). (b) A. S. Hinman, B. J. Pavelich, and K. McGarty. *Can. J. Chem.* **66**, 1589 (1988).
- (18) D. R. English, D. N. Hendrickson, and K. S. Suslick. *Inorg. Chem.* **22**, 367 (1983).
- (19) R. S. Czernuszewicz, K. A. Macor, X.-Y. Li, J. R. Kincaid, and T. G. Spiro. *J. Am. Chem. Soc.* **111**, 3860 (1989).
- (20) C. A. Reed. *The Biological Chemistry of Iron, N.A.T.O. Advanced Studies Institutes Series C Vol. 89. Edited by H. B. Dunford, D. Dolphin, K. N. Raymond, and L. Sieker. D. Reidel, Boston MA. 1982. pp. 25-42.*
- (21) M. A. Phillippi, E. T. Shimomura, and H. M. Goff. *Inorg. Chem.* **20**, 1322 (1981).

- (22) (a) J. T. Groves, R. C. Haushalter, M. Nakamura, T. E. Nemo, and B. J. Evans. *J. Am. Chem. Soc.* **103**, 2884 (1981). (b) D.-H. Chin, A. L. Balch, and G. N. La Mar. *J. Am. Chem. Soc.* **102**, 1446 (1980). (c) A. L. Balch, Y. W. Chan, R.-J. Cheng, G. N. La Mar, L. Latos-Grazynski, and M. W. Renner. *J. Am. Chem. Soc.* **106**, 7779 (1984). (d) A. Gold, K. Jayaraj, P. Doppelt, R. Weiss, G. Chottard, E. Bill, X. Ding, and A. X. Trautwein. *J. Am. Chem. Soc.* **110**, 5756 (1988).
- (23) (a) A. L. Balch and M. W. Renner. *J. Am. Chem. Soc.* **108**, 2603 (1986). (b) R. Guillard and K. M. Kadish. *Chem. Rev.* **88**, 1121 (1988).
- (24) R.-J. Cheng, L. Latos-Grazynski, and A. L. Balch. *Inorg. Chem.* **21**, 2412 (1982).
- (25) (a) D. L. Hickman and H. M. Goff. *Inorg. Chem.* **22**, 2789 (1983). (b) D. L. Hickman, A. Nanthakumar and H. M. Goff. *J. Am. Chem. Soc.* **110**, 6384 (1988).
- (26) (a) C. Swistak, X. H. Mu, and K. M. Kadish. *Inorg. Chem.* **26**, 4360 (1987). (b) W. A. Lee, T. S. Calderwood, and T. C. Bruice. *Proc. Natl. Acad. Sci. U.S.A.* **82**, 4301 (1985). (c) T. S. Calderwood, W. A. Lee, and T. C. Bruice. *J. Am. Chem. Soc.* **107**, 8272 (1985). (d) J. T. Groves and J. A. Gilbert. *Inorg. Chem.* **25**, 125 (1986). (e) T. S. Calderwood and T. C. Bruice. *Inorg. Chem.* **25**, 3722 (1986).

- (27) A. D. Adler, F. R. Longo, F. Kampas, and J. Kim. *J. Inorg. Nucl. Chem.* **32**, 2443 (1970).
- (28) (a) M. Kihn-Botulinski and B. Meunier. *Inorg. Chem.* **26**, 210 (1988). (b) J. S. Lindsey, I. C. Shreiman, H. C. Hsu, P. C. Kearney, and A. M. Marguerettaz. *J. Org. Chem.* **52**, 827 (1987). (c) R. W. Wagner, D. S. Lawrence, and J. S. Lindsey. *Tetrahedron Lett.* **28**, 3069 (1987).
- (29) A. S. Hinman, K. McGarty, C. Tang, and B. J. Pavelich. *Can. J. Chem.* **67**, 545 (1989).
- (30) I. A. Cohen, D. A. Summerville, and S. Ru Su. *J. Am. Chem. Soc.* **98**, 5813 (1976).
- (31) K. Anzai, K. Hatano, Y. J. Lee, and W. R. Scheidt. *Inorg. Chem.* **20**, 2337 (1981).
- (32) P. Gans, J.-C. Marchon, and J.-M. Moulis. *Polyhedron* **1**, 737 (1988).
- (33) (a) R. N. Adams. *Electrochemistry at Solid Electrodes*. Marcel Dekker, New York. 1969. (b) D. T. Sawyer and J. L. Roberts. *Experimental electrochemistry for Chemists*. Wiley-Interscience, New York. 1974.
- (34) E. J. Baerends, D. E. Ellis, and P. Ros. *Chem. Phys.* **2**, 41 (1973).
- (35) (a) E. J. Baerends. Ph.D. Thesis 1975, Vrije Universiteit. (b) W. Ravenek. *Algorithms and Applications on Vector and Parallel Computers*. Edited by H. J. J. Riele, Th. J. Dekker, and H. A. van de Horst. Elsevier, Amsterdam. 1987.

- (36) A. D. Becke. *J. Chem. Phys.* **88**, 2547 (1988).
- (37) L. Versluis and T. Ziegler. *J. Chem. Phys.* **88**, 322 (1988).
- (38) J. Krijn and E. J. Baerends. Fit Functions in the HFS-method; Internal Report (in Dutch), Free University; Amsterdam, The Netherlands, 1984.
- (39) O. Gunnarsson and I. Lundquist. *Phys. Rev.* **B10**, 1319 (1974).
- (40) S. J. Vosko, L. Wilk, and M. Nusair. *Can. J. Phys.* **58**, 1200 (1980).
- (41) A. D. Becke. *Phys. Rev.* **A38**, 2398 (1988).
- (42) J. P. Perdew. *Phys. Rev.* **B33**, 8822 (1986). J. P. Perdew. *Phys. Rev.* **B34**, 7406 (1986) (erratum).
- (43) W. R. Heineman, F. M. Hawkridge, and H. N. Blount. Electroanalytical Chemistry Vol. 13. *Edited by* A. J. Bard. Marcel Dekker, New York. 1983. pp. 1-104.
- (44) (a) A. S. Hinman, S. Pons, and J. Cassidy. *Electrochim. Acta* **30**, 89 (1985). (b) A. S. Hinman, S. Pons, and J. Cassidy. *Electrochim. Acta* **30**, 95 (1985).
- (45) (a) X. Q. Lin and K. M. Kadish. *Anal. Chem.* **57**, 1498 (1985). (b) X. Q. Lin and K. M. Kadish. *Anal. Chem.* **58**, 1493 (1986).
- (46) J. P. Bullock and K. R. Mann. *Inorg. Chem.* **28**, 4006 (1989).
- (47) H. B. Mark Jr., T. M. Kenyhercz, and P. T. Kissinger. Electrochemical Studies of Biological Systems. *Edited by* D. T. Sawyer. Ann. Chem. Soc. Symp. Ser. 1977. pp. 1-25.

- (48) R. W. Hurst, W. R. Heineman, and E. Deutsch. *Inorg. Chem.* **20**, 3298 (1981).
- (49) E. A. Blubaugh, A. M. Yacynych, and W. R. Heineman. *Anal. Chem.* **51**, 561 (1979).
- (50) J. W. Strojek, G. A. Gruver, and T. Kuwana. *Anal. Chem.* **41**, 481 (1969).
- (51) E. E. Wells Jr. *Anal. Chem.* **45**, 2022 (1973).
- (52) A. M. Yacynych and H. B. Mark Jr. *J. Electrochem. Soc.* **123**, 1346 (1976).
- (53) E. Steckhan. *Electrochim. Acta* **22**, 395 (1977).
- (54) E. Steckhan and D. A. Yates. *Ber. Bunsenges Phys. Chem.* **81**, 369 (1977).
- (55) A. Wolberg and J. Manassen. *J. Am. Chem. Soc.* **92**, 2982 (1970).
- (56) I. B. Goldberg and A. J. Bard. *J. Electroanal. Chem.* **38**, 313 (1972).
- (57) I. B. Goldberg, A. J. Bard and S. W. Feldberg. *J. Phys. Chem.* **75**, 3281 (1972).
- (58) T. Kuwana and N. Winograd. *Electroanalytical Chemistry Vol. 7. Edited by A. J. Bard.* Marcel Dekker, New York. 1974. pp. 1-74.
- (59) F. R. Shu and G. S. Wilson. *Anal. Chem.* **48**, 1676 (1976).
- (60) D. L. Langhus and G. S. Wilson. *Anal. Chem.* **51**, 1139 (1979).

- (61) E. F. Bowden, F. M. Hawkridge, J. F. Chlebowski, E. E. Bancroft, C. Thorpe, and H. N. Blount. *J. Am. Chem. Soc.* **104**, 7641 (1982).
- (62) M. Petek, T. E. Neal, and R. W. Murray. *Anal. Chem.* **43**, 1069 (1971).
- (63) H. Oshio, T. Ama, T. Watanabe, J. Kincaid, and K. Nakamoto. *Spectrochim. Acta, Part A* **40**, 863 (1984) and references therein.
- (64) X.-Y. Li, R. S. Czernuszewicz, J. R. Kincaid, Y. O. Su, and T. G. Spiro. *J. Phys. Chem.* **94**, 31 (1990).
- (65) J. Fajer, D. C. Borg, A. Forman, D. Dolphin, and R. H. Felton. *J. Am. Chem. Soc.* **92**, 3451 (1970).
- (66) H. Kashiwagi and S. Obara. *Int. J. Quantum Chem.* **20**, 843 (1981).
- (67) L. L. Gladkov and K. N. Solovyov. *Spectrochim. Acta, Part A* **41**, 1443 (1985).
- (68) P. V. Croatto and T. A. Keiderling. *Chem. Phys. Lett.* **144**, 455 (1988).
- (69) K. M. Barkigia, M. D. Berber, J. Fajer, C. J. Medforth, M. W. Renner, and K. M. Smith. *J. Am. Chem. Soc.* **112**, 8851 (1990).
- (70) T. Ziegler, A. Rauk, and E. J. Baerends. *Chem. Phys.* **16**, 209 (1976).
- (71) D. P. Cox, J. Terpinski, and W. Lawrynowicz. *J. Org. Chem.* **49**, 3216 (1984).
- (72) R. K. Sharma and J. L. Fry. *J. Org. Chem.* **48**, 2112 (1984).

- (73) (a) A. S. Hinman, B. J. Pavelich, A. E. Kondo, and S. Pons. *J. Electroanal. Chem.* **234**, 145 (1987). (b) A. S. Hinman and B. J. Pavelich. *J. Electroanal. Chem.* **269**, 53 (1989).
- (74) H. Sugimoto, N. Ueda, and M. Mori. *Bull. Chem. Soc. Jpn.* **55**, 3468 (1982).
- (75) H. M. Goff and M. A. Phillippi. *J. Am. Chem. Soc.* **105**, 7567 (1983).
- (76) J. T. Groves and Y. Watanabe. *J. Am. Chem. Soc.* **110**, 8443 (1988).
- (77) D. C. Rawlings, M. Gouterman, E. R. Davidson, and D. Feller. *Int. J. Quantum Chem.* **28**, 823 (1985).
- (78) (a) W. D. Edwards, B. Weiner, and M. C. Zerner. *J. Phys. Chem.* **92**, 6188 (1988). (b) P. Du, F. U. Axe, G. H. Loew, S. Canuto, and M. C. Zerner. *J. Am. Chem. Soc.* **113**, 8614 (1991).
- (79) W. R. Scheidt, Y. J. Lee, S. Tamai, and K. Hatano. *J. Am. Chem. Soc.* **105**, 778 (1983).
- (80) T. Ziegler. *Chem. Rev.* **91**, 651 (1991).
- (81) M. A. Phillippi and H. M. Goff. *J. Am. Chem. Soc.* **104**, 6026 (1982).
- (82) R. Guillard, B. Boisselier-Cocolios, A. Tabard, P. Cocolios, B. Simonet, and K. M. Kadish. *Inorg. Chem.* **24**, 2509 (1985).
- (83) A. D. Boersma and H. M. Goff. *Inorg. Chem.* **23**, 1671 (1984).
- (84) R. S. Czernuszewicz and K. A. Macor. *J. Raman Spectrosc.* **19**, 552 (1988).

- (85) D. Lancon, P. Cocolios, R. Guillard, and K. M. Kadish. *J. Am. Chem. Soc.* **106**, 4472 (1984).
- (86) (a) D. R. English, D. N. Hendrickson, and K. S. Suslick. *Inorg. Chem.* **22**, 367 (1983). (b) K. M. Kadish, R. K. Rhodes, L. A. Botoomley, and H. M. Goff. *Inorg. Chem.* **20**, 3195 (1981).
- (87) (a) J. P. Battioni, D. Lexa, D. Mansuy, and J.-M. Saveant. *J. Am. Chem. Soc.* **105**, 207 (1983). (b) D. Lancon and K. M. Kadish. *Inorg. Chem.* **23**, 3942 (1984).
- (88) H. M. Goff and M. A. Phillippi. *J. Am. Chem. Soc.* **105**, 7567 (1983).
- (89) G. H. Loew. Iron Porphyrins Part I. *Edited by* A. B. P. Lever and H. B. Gray. Addison-Wesley, Reading MA. 1983. pp. 1-87.
- (90) A. L. Balch and M. W. Renner. *J. Am. Chem. Soc.* **108**, 2603 (1986).
- (91) E. B. Fleischer, J. M. Palmer, T. S. Srivastava, and A. Chatterjee. *J. Am. Chem. Soc.* **93**, 3162 (1971).
- (92) M. Gouterman. *J. Mol. Spectrosc.* **6**, 138 (1961).
- (93) C. Weiss, H. Kobayashi, and M. Gouterman. *J. Mol. Spectrosc.* **16**, 45 (1965).
- (94) W. D. Edwards and M. C. Zerner. *Can. J. Chem.* **63**, 1763 (1985).
- (95) (a) W. A. Eaton and R. M. Hochstrasser. *J. Chem. Phys.* **46**, 2533 (1967). (b) W. A. Eaton and R. M. Hochstrasser. *J. Chem. Phys.* **49**, 985 (1968).

- (96) (a) R. Guillard and K. M. Kadish. *Chem. Rev.* **88**, 1121 (1988). (b) R. Guillard, C. Lecomte, and K. M. Kadish. *Struct. Bonding (Berlin)* **64**, 71 (1987).